

“Alexandru Ioan Cuza” University

Department of Physics

**Applications of low-pressure discharge plasma in surface  
science and nanotechnology**

*Lucel Sirghi*

**Habilitation Thesis**

Iasi, Romania

March, 2012

Lucrarea de fata sintetizeaza rezultatele activitatii mele de cercetare stiintifica desfasurate in perioada 2000-2012 in laboratorul de fizica plasmei de la Universitatea „Alexandru Ioan Cuza” din Iasi, dar si in laboratoare de la Universitatile Nagoya si Shizuoka din Japonia, Institutul de Tehnologie Georgia din Atlanta, USA, si Institutul de Sanatate si Protectia Consumatorului din Centrul Comun de Cercetare al Comisiei Europene, Ispra, Italia.

In acest context doresc sa multumesc tuturor colaboratorilor si profesorilor cu care am lucrat pentru sprijinul si contributia lor la obtinerea acestor rezultate. De asemenea, multumesc familiei mele care m-a sprijinit si mi-a fost alaturi in tot acest timp.

The present work is a synthesis of main scientific results obtained by the author in the period 2000-2012 in the laboratory of plasma physics at “Alexandru Ioan Cuza” University of Iasi, and also in laboratories from Nagoya University and Shizouka University in Japan, Georgia Institute of Technology in Atlanta, USA, and the Institute for Health and Consumer Protection of Joint Research Center of European Commission in Ispra (Italy).

In this context, I would like to thank all my collaborators and professors for their support and contributions to the results presented in this thesis. Also, I would like to thank my family for being supportive along all these years.

# CONTENT

I. Resume .....	1
II. Applications of low-pressure discharge plasma in surface science and nanotechnology .....	3
II.1 Plasma assisted depositions of thin films with applications in surface science and nanotechnology .....	4
II.1.1 Plasma assisted depositions of photocatalytic titanium dioxide thin films.....	9
II.1.2 Plasma enhanced chemical vapor deposition of super hydrophobic fluorocarbon thin films with application in nanoindentation lithography.....	34
II.1.3 High power impulse magnetron sputtering deposition of optically transparent and electrically conductive ZnO:Al thin films .....	42
II.2 Application of low-pressure discharge plasma in atomic force microscopy and nanotechnology.....	51
II.2.1 Plasma cleaning and hydrophilization of silicon surface of AFM probes.....	53
II.2.2 Coating of AFM probes by plasma assisted depositions of thin films.....	58
II.2.3 Effect of plasma surface treatment of AFM probe and sample surfaces on microscopic adhesive forces.....	64
II.2.4 Sensing the chemical contrast by hydrophilic AFM probes.....	73
II.2.5. Control of adhesion in AFM indentation experiments.....	89
III. Prospective and future research.....	103
IV Selected papers.....	117
References.....	123

## I Rezumat

Fabricarea de materiale functionale si inteligente este esentiala in domenii de varf ale stiintei si tehnologiei ca microelectronica, energie, medicina, nanotehnologie, etc. In acest sens, utilizarea plasmei\_gazelor la joasa presiune in modelarea proprietatilor de suprafata a solidelor este din ce in ce mai populara deoarece tehnologiile cu plasma evita riscurile asociate cu manipularea substanelor chimice precum si poluarea chimica. Aceasta tendinta se datoreaza si dezvoltarii recente a nanotehnologiei cu necesitatea ei de a controla la scara nanometrica structura si compozitia chimica a suprafetelor.

Aceasta teza de abilitare prezinta rezultatele obtinute de autor in utilizarea plasmei gazelor de joasa presiune la tratamente de suprafata si depuneri de filme subtiri cu diverse aplicatii in stiinta suprafetei si nanotehnologie. Plasma gazelor la joasa presiune a fost utilizata la depunerea chimica in vaporii (CVD) si depunerea prin pulverizare de filme subtiri cu aplicatii in cataliza heterogena, fabricarea de suprafete hidrofobe, electrozi optic transparenti si suprafete repulsive pentru proteine si celule vii. Filme photocatalitice de dioxid de titan ( $TiO_2$ ) au fost obtinute prin depuneri CVD asistate de plasma (PECVD) si prin depuneri prin pulverizare in plasma descarcarii magnetron de radiofrecventa. Au fost studiate efectele parametrilor plasmei si a parametrilor de depunere asupra structurii si proprietatilor filmelor depuse. In cazul depunerilor filmelor subtiri de  $TiO_2$  pe substraturi polimerice, s-a observat o instabilitate de incretire a suprafetei substraturilor, efect ce a fost atribuit bombardarii suprafetelor cu particule energetice (ioni pozitivi de argon). De asemenea s-a observat ca proprietatile photocatalitice ale filmelor de  $TiO_2$  ultra subtiri depind de grosimea filmelor, fapt ce a fost atribuit unei rugozitati mai mici a acestor filme, absorptiei partiale a luminii si separarii spatiale a purtatorilor de sarcini electrice. Descarcarea magnetron reactiva in impuls de mare putere a fost utilizata la depuneri de filme optic transparente si electric conductoare de oxid de zinc dopat cu aluminiu, filme ce au aplicatii in fabricarea celulelor solare. Aceste depuneri au folosit o noua metoda de dopare, metoda ce consta in pulverizarea unui electrod din aluminiu plasat in apropierea catodului. Depuneri PECVD au fost folosite pentru fabricarea filmelor subtiri de fluorocarbon pentru obtinerea de suprafete cu energie de suprafata mica si indice de plasticitate mare, proprietati necesare in nanolitografia de indentare. De asemenea, depuneri PECVD s-au utilizat si pentru sinteza straturilor subtiri de polietilen glicol (PEO) in scopul obtinerii de suprafete repulsive pentru proteine si celule vii. Astfel de filme sunt utilizate pentru obtinerea de paternuri cu contrast biologic adeziv/non-adereziv la scara nanometrica prin tehnici ca tratamente de suprafata cu plasma, litografie prin iradiere cu fascicul de electroni, imprimare prin micro-contact si micro-depuneri de proteine.

Teza de abilitare prezinta si rezultate referitoare la efectele modificarii cu ajutorul plasmei a suprafetelor asupra fortelor de adeziune si frecare la scara nanometrica. Aceste rezultate au fost obtinute fie prin aplicarea tratamentelor de curatire cu plasma, fie prin acoperirea cu filme subtiri a sondelor utilizate in microscopia cu forta atomica (AFM). Astfel, sonde AFM au fost acoperite cu un strat subtire de TiO<sub>2</sub> pentru a controla hidrofilicitatea suprafetei acestora intr-un studiu al efectului condensarii capillare a vaporilor de apa din atmosfera asupra fortelor de adeziune si frecare la contactul intr-o singura asperitate nanoscopica. Sonde AFM acoperite de un strat subtire de PEO au fost utilizate intr-un studiu al conditiilor optime de transfer al proteinelor prin tehnica de imprimare prin microcontact. Sondele AFM acoperite cu un strat subtire de PEO au fost de asemenea folosite pentru a reduce sau anula forta de adeziune in experimente de indentare AFM a celulelor vii.

Curatirea cu plasma a sondelor AFM din siliciu a fost utilizata pentru controlul proprietatilor chimice ale suprafetelor acestora. Curatirea cu plasma inlatura cu eficienta moleculele contaminante hidrofobe de pe suprafata sondelor AFM, obtinand in acest fel sonde cu suprafete curate si foarte hidrofile. Acest tratament are ca rezultat o crestere puternica a fortelor de adeziune la contactul in aer ale varfurile nanoscopice ale sondelor AFM cu suprafatele hidrofile ale specimenelor. In acelasi timp, tratamentul are ca rezultat o anulare a fortelor de adeziune in apa. Probele AFM curatite cu plasma sunt utile pentru determinarea contrastului chimic pe suprafata unui specimen prin masuratori de microscopie cu forta de frecare sau adeziune in aer. Regiunile mai hidrofile de pe suprafata unui specimen sunt caracterizate de formarea de meniscuri capilare de apa mai mari si, corespunzator, de forte de adeziune si frecare mai mari in comparatie cu regiunile mai putin hidrofile sau hidrofobe. Acest principiu a fost folosit pentru a distinge regiuni de activitate photocatalitica diferita pe suprafata filmelor subtiri de TiO<sub>2</sub>. Sonde AFM curatare cu plasma au fost utilizate pentru evidențierea contrastului chimic ale nanopaternelor obtinute prin litografia cu fascicul de electroni pe suprafetele filmelor de PEO.

## I Resume

The development of functional and smart materials is an essential task in many fields of science and technology such as microelectronics, energy, medicine, nanotechnology, etc. The low-pressure plasma has become an increasingly popular tool for tailoring the properties of solid surfaces because the plasma techniques avoid chemical hazards and waste. This trend is favored also by the recent development of nanotechnology with its need for control of surface structure and chemistry at nanoscale.

This habilitation thesis presents the results obtained by the author in using low-pressure plasmas for surface treatments and depositions of thin films with various applications in surface science and nanotechnology. Low pressure plasmas have been used for chemical vapor deposition (CVD) and sputtering deposition of thin films with applications in heterogeneous catalysis and fabrication of water repellent surfaces, transparent electrodes, and bio repellent coatings. Photocatalytic titanium dioxide ( $TiO_2$ ) thin films have been fabricated by plasma enhanced CVD (PECVD) and radio frequency magnetron sputtering deposition. Effects of deposition and plasma parameters on the structure and properties of deposited films have been studied. In case of polymer substrates, a surface buckling instability has been observed and attributed to high energy plasma particle bombardment. The photocatalytic property of ultrathin  $TiO_2$  thin films depended on thickness, fact which has been attributed to a smaller surface roughness, partial absorption of light, and a space separation of charge carriers at the film surfaces. Reactive high power impulse magnetron sputtering deposition has been used to deposit transparent conductive films of aluminum doped zinc oxide with applications in solar cells and flat panel displays. In this deposition, a novel doping method consisting in sputtering of an aluminum electrode positioned in the proximity of the cathode has been used. The PECVD at low discharge power (5-10 W) has been used for fabrication of fluorocarbon thin films with low surface energy and high plasticity index for nanoindentation lithography. The PECVD has been used also for synthesis of polyethylene glycol oxide (PEO) thin films to obtain biorepellent surfaces for proteins and living cells. Such films are used for fabrication of micro- and nano- patterns with adhesive/nonadhesive contrast for proteins and living cells by techniques as plasma surface treatment, electron beam lithography, micro-contact printing and micro-spotting.

The thesis presents also results concerning the effect of plasma modification of surface properties on nanoscale adhesion and friction forces. These results have been obtained by plasma-cleaned or plasma-coated atomic force microscopy (AFM) probes. Thus, the RFMSD was used to coat AFM probes with TiO<sub>2</sub> to control the hydrophilicity of the AFM tips used in an experimental investigation of the effect of capillary condensation of atmospheric water vapor on adhesion and friction forces at single-asperity nanocontacts. The AFM tips were covered by thin PEO layers in order to study the optimal conditions of protein transfer in microcontact printing. The PEO covered AFM tips have been used also to reduce or cancel the adhesion force between AFM tips and living cells in AFM indentation experiments.

Cleaning of silicon AFM probes in low-pressure air plasma was also used to control the chemistry of AFM probe surfaces. The plasma cleaning treatment removes efficiently the adsorbed hydrophobic contaminant molecules and renders clean and highly hydrophilic probe surfaces. This treatment results in a strong increase of AFM tip-sample adhesion force in air and a cancelation of the adhesion force in water. Plasma cleaned and hydrophilized AFM tips are suitable for sensing chemically different regions on a sample surface by either friction force microscopy or adhesive force mapping in ambient air. The chemical contrast in friction and adhesion force images is related to the capillary condensation of water vapor at the AFM tip-sample contact. More hydrophilic regions on a sample surface are characterized by larger water menisci and adhesive force values as compared to less hydrophilic (or hydrophobic) regions. This principle has been used to distinguish regions of different photocatalytic activity on the UV irradiated TiO<sub>2</sub> thin films. Plasma cleaned AFM tips were used also in study of chemical contrast of nanopatterns obtained by electron beam lithography on PEO surface.

## **II. Applications of low-pressure discharge plasma in surface science and nanotechnology**

The ability to control surface properties is hugely important in heterogeneous catalysis, semiconductor device fabrication, biology (biosensors, implants, etc), polymer science, nanotechnology, etc. Low-pressure discharge plasma is known as one of the most versatile technique used to tailor properties of solid surfaces by cleaning, etching, thin film depositions, doping, ion implantation, and surface functionalization. All these plasma techniques have the advantage of allowing a good control of the processes at spatial resolution as high as few tenths of nanometers. Moreover, plasma technology is environmentally friendly since it uses dried processes that are not using solvents generating chemical waste. This section describes results obtained by the author of the present habilitation thesis in using plasma to control surface chemistry for applications in photocatalysis, transparent electrodes for solar cells, nanobiotechnology, and atomic force microscopy. Results concerning plasma assisted thin film depositions and characterization are presented in subsection II.1, while the results concerning plasma surface treatments with applications in atomic force microscopy and nanobiotechnology are presented in subsection II.2.

The, subsection II.1 presents the results concerning depositions and characterization of photocatalytic titanium dioxide, super hydrophobic fluorocarbon, and optically transparent and electrically conductive aluminum doped zinc oxide thin films. Deposition mechanisms and effect of deposition parameters on film structure and properties are described. The film properties and structure are discussed in connection with the impingement of high-energy particles on film surface during deposition. Results of a study of dependence of mechanical properties of fluorocarbon thin films deposited by plasma enhanced chemical depositions in connection with discharge power are also described. Finally, this subsection presents a new doped method in reactive high power impulse magnetron sputtering deposition of metal oxide thin films. The method has been applied to control aluminum doping of zinc oxide thin films. The details on plasma assisted deposition and characterization of biorepellent polyethylene glycol oxide thin films are described in subsection II.2. Subsection II.2 presents results concerning plasma cleaning of atomic force microscopy (AFM) probes and the effects of plasma treatments (cleaning and coating) on adhesion and friction surface forces. It is shown

that plasma-cleaned AFM probes are efficient in sensing of chemical contrast of nanopatterns and surface heterogeneity at nanoscale. Results concerned the use of plasma to coat AFM tips with biorepellent coatings (polyethylene glycol oxide) for study of adhesive force in microcontact printing and nanoscale indentations are also described.

## ***II.1 Plasma assisted depositions of thin films with applications in surface science and nanotechnology***

This section describes results obtained by the author in using low-pressure plasmas for depositions of photocatalytic titanium dioxide ( $\text{TiO}_2$ ), super hydrophobic fluorocarbon ( $\text{CF}_x$ ), optically transparent and electrically conductive  $\text{ZnO}:\text{Al}$ , and protein and cell repellent polyethylene glycol oxide (PEO) thin films. Titanium dioxide thin films were fabricated by either plasma enhanced chemical vapor depositions (PECVDs) or radio frequency magnetron sputtering depositions (RFMSDs), while the  $\text{CF}_x$  and PEO thin films were fabricated by PECVDs. The aluminum doped  $\text{ZnO}$  thin films ( $\text{ZnO}:\text{Al}$ ) were prepared by high power impulse magnetron sputtering (HiPIMS) deposition using an original doping method consisting in a secondary electrical discharge on a negatively biased auxiliary aluminum electrode. The PEO films were obtained by PECVD using a low power (5W) pulsed capacitively coupled r.f. discharge. Details on PEO deposition are given in section II.2.2

Titanium dioxide is an important environmental material with applications in photocatalytic air and water purification, hydrogen energy, and fabrication of self-cleaning and antibacterial surfaces [1]. The capacity of  $\text{TiO}_2$  surface to degrade organic macromolecules and decompose water is own to the strong oxidation potential of the holes excited by the UV light in the valence band [2]. Since Fujishima and Honda [1] reported the photocatalytic hydrolysis of water on the UV light radiated titanium dioxide ( $\text{TiO}_2$ ), the photocatalytic property of this material has been studied intensively [3]. According to the current explanation [2], The UV light irradiated  $\text{TiO}_2$  surface becomes super hydrophilic because of the photocatalytic decomposition of either water or hydrophobic adsorbate molecules at  $\text{Ti}^{4+}$  photoreduced to  $\text{Ti}^{3+}$  sites, which typically are situated at the oxygen bridges on the surface. The UV induced hydrophilicity is reversible, the surface turning hydrophobic during storage in dark or visible light [4] or by wet rubbing [5]. Recent studies revealed the role that charge carrier production and transport in the  $\text{TiO}_2$  film have on the UV light induced surface reactions [6, 7]. Mechanic quantum simulation of water adsorption on a  $\text{T}_7\text{O}_{14}$  embedded cluster [8] revealed that while the photoexcited electrons are localised by

subsurface  $\text{Ti}^{4+}$  atoms, the photoexcited holes are delocalised on surface and involved in water surface reactions that lead to generation of  $\text{OH}^-$  or  $\text{OH}^*$  chemisorbed radicals. Formation of  $\text{OH}^*$  radicals on the UV light irradiated  $\text{TiO}_2$  surface was proved by ESR measurements [9] and it is believed that these hydroxyl radicals contribute to the photocatalytic activity and UV light induced super hydrophilicity of the  $\text{TiO}_2$  surface [10].

Polymeric  $\text{CF}_x$  films are known to render a surface with very low energy and relatively good hardness and wearing resistance. These properties make these films interesting for coatings that reduce adhesion of water, oily contaminants, bacteria, etc. Such coatings are desirable for magnetic recording media [11], electric insulators for electric power lines [12], and biomedicine applications [13, 14]. Fluorocarbon films with good hydrophobic and hardness properties are usually synthesised by PECVD that employs discharge plasmas to dissociate precursor gases [15, 16]. In order to obtain a good compromise between the good hydrophobic property of pure fluorocarbon films and the good hardness and wear resistance of pure hydrocarbon films (which are not hydrophobic) fluorinated carbon films are synthesized by PECVD in mixed hydrocarbon and fluorocarbon gases [15]. For these films, it was found that their hydrophobicity improves by the increase of the fluor content, while the hardness and wearing resistance decrease [16]. An alternative method to synthesise fluorocarbon film consists of sputtering deposition in a r.f. magnetron discharge using polytetrafluoroethylene (PTFE) target [17]. Systematic studies of dependence of hydrophobic property and mechanical properties of these fluorocarbon films on different deposition parameters (discharge power, mixture gas content, substrate biasing potential, gas pressure) are reported in [18].

Zinc oxide ( $\text{ZnO}$ ) is a n-type semiconductor with a wide direct energy band gap of 3.44 eV at room temperature, large exciton binding energy (60 meV), large piezoelectric constant, strong luminescence, high sensitivity of surface conductivity to adsorbed species, and high thermal conductivity. The material is easy to grow as large bulk single crystals or as polycrystalline thin films [19, 20]. All these properties make  $\text{ZnO}$  a strong candidate for fabrication of optoelectronic devices for blue light and UV radiation, transparent electrodes for solar cells, and sensor and actuator devices. Controlling of the conductivity of  $\text{ZnO}$  thin films is a key point in most of their applications. The  $\text{ZnO}$  films prepared without introduction of extrinsic doping atoms show a native n-type low conductivity (resistivity about  $10^7 \Omega\cdot\text{cm}$ ) that depends much on the film structure and purity. The origin of the n-type conductivity of intrinsic  $\text{ZnO}$  has been attributed initially to defects as oxygen vacancies or

zinc interstitials; fact invalidated by density functional calculations [21] and optically detected electron paramagnetic resonance measurements [22]. Therefore, the cause of ZnO n-type conductivity could be related to the intentional or unintentional incorporation of atoms that act as shallow donors (either metals with one additional conduction electron on zinc lattice sites or halogens with one additional electron on oxygen lattice sites) [19]. In particular, the ZnO films doped with aluminum (ZnO:Al) are considered for manufacturing of transparent electrodes for flat panel displays, solar cells and organic light-emitting diodes [23]. In these films, the extra valence electrons of the Al atoms that substitute Zn are easily excited to the conduction band, the ionization energy being 120 meV [24], fact that renders the good conductivity of these films. Transparent ZnO:Al thin films with electrical resistivity as low as  $2 \times 10^{-4} \Omega \cdot \text{cm}$  has been prepared by d.c. or r.f. magnetron sputtering of composite metallic Zn:Al (2 wt%) or ceramic ZnO/Al<sub>2</sub>O<sub>3</sub> (2wt%) targets [25]. However, these magnetron sputtering techniques does not allow for an independent control of Al concentration in the ZnO:Al films, the working gas pressure and composition (partial pressure of O<sub>2</sub>) being used as key deposition parameters to optimize the film electrical conductivity.

Polyethylene Glycol Oxide (PEO) thin films provide non-fouling surfaces in physiologic solutions for proteins and cells, fact that make these films useful in fabrication of biosensors. It is believed that the biologic non-fouling character of PEO surface is own to the self-repulsion of their polymer chains in aqueous solutions [26]. Particularly, pulsed plasma polymerization of pure diethylene glycol dimethyl ether monomer allowed fabrication of PEO thin layers highly stable in water, ethanol or phosphate buffer saline (PBS) solutions and with a high retention of polyethylene oxide character [27]. Moreover, the PEO thin films provides a good bioadhesive/biorepellent surface contrast at micro- and nano-scale by lithography techniques involving plasma treatment [28], electron beam irradiation [29], microcontact printing [30] and microspotting [31]. It has been shown that plasma treatment and electron irradiation reduced the PEO-like character of the surface by decreasing the ether bond density along with increasing of hydrocarbon bond density [28, 29]. In a recent work {Ruiz *et al* [30]}, Sirghi used PEO coated AFM probes to study the optimal conditions for the protein transfer from a elastomer stamp to the PEO surface, a study relevant to optimization of microcontact printing of protein patterns on PEO surface. Also, Sirghi performed an AFM study of morphology of protein layer deposited by microspotting [31] on PEO surface and AFM studies of protein bioadhesive/biorepellent patterns created by

electron beam lithography { see [29] and selected paper P9 [32]}. Details of PEO film deposition and characterizations are given in sections II.3.2 and II.3.4.

Recently, different deposition techniques have been developed to produce TiO<sub>2</sub> thin films with the goal of obtaining photocatalytic surfaces [33, 34]. Among these techniques the sputtering deposition is known to produce films with high adhesion and hardness, but with relatively low photocatalytic activity [26]. Sirghi et al showed that the low photocatalytic activity of these films corresponds to their heterogeneous crystalline and amorphous mesostructure {see selected papers P1 [35] and P2 [36]}. The selected paper P1 reports results of a microscopic study of surface hydrophilicity of UV-irradiated TiO<sub>2</sub> thin films obtained by RFMSD and PECVD. The study is based on dependence of the adhesion force measured in air at medium humidity between a hydrophilic AFM tip and TiO<sub>2</sub> thin film surfaces. It has been found that PECVD films have higher photocatalytic activity and more homogeneous and smooth surfaces as compared to RFMSD films. However, in the selected paper P2 it has been reported that a good choice of the sputtering deposition parameters may yield high quality films. Thus, radio frequency magnetron sputtering of a pure TiO<sub>2</sub> target in Ar(91%)-O<sub>2</sub>(9%) mixture gas at pressure of 10 mTorr resulted in depositions of amorphous TiO<sub>2</sub> films with microscopically homogeneous surfaces and good UV-light-induced hydrophilicity. It has been shown that the mesoscopic structure and UV-induced hydrophilicity of the TiO<sub>2</sub> films obtained by RFMSDs are determined by the plasma particle bombardment of the film surface during deposition. Single Langmuir probe [36] and optical emission spectroscopy diagnosis [37] of RFMSD plasma proved that the pressure value of Ar-O<sub>2</sub> gas has a big impact on plasma parameters and plasma particle bombardment of the deposited films. The low energy of plasma particles (ions and electrons) at relatively high value of the gas pressure (10 mTorr) favored deposition of amorphous TiO<sub>2</sub> thin films with a short range order of anatase type, good UV-light-induced hydrophilicity, microscopically smooth and homogeneous surfaces. At lower gas pressure values, the energy of plasma particles increases favoring depositions of TiO<sub>2</sub> films with mixed crystalline and amorphous structure and relatively rough and inhomogeneous surfaces. The mixed crystalline structure of the films deposited at low gas pressure (less than 10 mTorr) has been observed as film surface nanoscopic regions of high hydrophilicity mixed with regions of low hydrophilicity on UV irradiated TiO<sub>2</sub> film surfaces. These regions are discriminated by friction force microscopy measurements, the friction force values being larger on hydrophilic regions than the values measured on less hydrophilic regions of the UV irradiated TiO<sub>2</sub> thin films [38].

Sirghi and Hatanaka have shown that the photocatalytic activity of amorphous TiO<sub>2</sub> thin films obtained by RFMSD depended on film thickness {see the selected paper P3, [7]}. For films thicker than a threshold value of about 12 nm the effect of UV light irradiation on the film surface hydrophilicity was fast, strong and did not depend on substrate or thickness, while for thinner films it was weak and dependent on substrate or thickness. The weak effect of UV light irradiation observed for the ultra-thin films (with thickness less than 12 nm) was explained based on results of measurements of surface topography, UV-light absorption and photocurrent decay in vacuum. Comparing to thicker films, the ultra-thin films have a smoother surface, which diminish their real surface area and density of defects, absorb partially the incident UV light radiation, and exhibit a longer decay time of the photocurrent in vacuum, which proves a spatial charge separation. All these effects contribute to a low UV light irradiation effect on the ultra-thin film hydrophilicity.

Sirghi et al {see the selected paper P4 [39]} analyzed the energy flux density transported by plasma particles and photons on the deposition substrate and growing film surface. This energy flux may affect drastically not only the properties of the deposited TiO<sub>2</sub> thin films, but also the surface morphology at nanoscale in case of polymer substrates. This was the case of RFMSDs of TiO<sub>2</sub> on polymethyl methacrylate and polycarbonate substrates, which showed buckling of their surfaces. The effect was evaluated by analysis of atomic force microscopy topography images of the deposited TiO<sub>2</sub> films. The amount of energy received by the substrate surface during the film deposition was determined by a thermal probe. Then, the results of thermal probe measurements were used to compute surface temperature of the polymer substrate. The computation indicated substrate surface temperature values under the polymer melting temperature. Therefore, the buckling of polymer substrate surface in the deposition plasma was not regarded as a temperature driven surface instability, but as an effect of plasma ion bombardment.

Sirghi et al {see the selected paper P5 [40]} studied the mechanical properties of fluorocarbon (CF<sub>x</sub>) thin films obtained from C<sub>4</sub>F<sub>8</sub> gas by PECVD at low *r.f.* power (5-30 W) and *d.c.* self-biasing potential (10-80V). This particular deposition method renders films with good hydrophobic property and high plastic compliance. The mechanical properties at nanoscopic scale were determined by AFM indentation technique. Force depth curves and imprint characteristics were used for determination of film hardness, elasticity modulus and plasticity index. The measurements show that the decrease of the discharge power results in deposition of films with decreased hardness and stiffness and increased plasticity index.

Nanolithography based on AFM indentation was demonstrated on thin films (thickness of 40 nm) with good plastic compliance.

In a recent work, Sirghi et al [41] investigated a new doping method in high power impulse magnetron sputtering (HiPIMS) deposition of thin metal oxide films. The method has been applied successfully to control the aluminium doping of ZnO:Al thin films obtained by reactive HiPIMS of a pure Zn target [42] and consisted in sputtering of an electrically negative biased aluminum electrode placed in the proximity of the negative glow of the magnetron discharge. Resonant laser absorption measurements of Al atom concentration in vapor phase during the depositions and the XPS (X-ray Photoelectron Emission Spectroscopy) measurements of Al concentration in the deposited ZnO:Al films confirmed the doping control. ZnO:Al thin films with concentrations of Al ranged between 0.1 at.% and 28.5% at% have been obtained by choosing suitable values of Al electrode biasing potential. The optical properties of the deposited films were characterized by ultraviolet-visible (UV-Vis) transmission spectroscopy, while the film crystalline structure were investigated by X-ray diffraction (XRD) and deposition of optically transparent ZnO:Al thin films with good electrical conductivity and crystallinity was reported.

### **II.1.1 Plasma assisted depositions of photocatalytic titanium dioxide thin films**

Titanium dioxide thin films have been deposited by either plasma enhanced chemical vapor deposition (PECVD) using titanium tetraisopropoxide, Ti-(O-*i*-(C<sub>3</sub>H<sub>7</sub>)<sub>4</sub>, (TTIP) as a source gas and H<sub>2</sub>/O<sub>2</sub> plasma as process enhancer or by sputtering of a pure TiO<sub>2</sub> sintered target in a radio frequency magnetron discharge in Ar/O<sub>2</sub> gas. Both methods produce for optimal values of deposition parameters highly photocatalytic amorphous TiO<sub>2</sub> thin films.

The author (L. Sirghi) has contributions in investigation of mechanism of TiO<sub>2</sub> thin film synthesis by PECVD showing that H radical is the active plasma component that dissociate the TTIP molecules [43]. It has been found that addition of O<sub>2</sub> to H<sub>2</sub> gas results in a drastic increase of H radical density and film deposition rate. The highest deposition rate of 11 nm/min, which was much higher than that for the case of single gas (H<sub>2</sub> or O<sub>2</sub>) plasmas, was obtained in the case of mixture gas ratio of 80% H and 20% O. It was proved that, at higher content of O<sub>2</sub>, the deposition rate decreased due to presence of OH radical molecules. The substrate temperature had not affected the deposition rate, but significantly changed the film structure. It was concluded that the use of H<sub>2</sub>/O<sub>2</sub> plasma is effective for obtaining a high

deposition rate of  $\text{TiO}_x$  thin films with a high content of OH groups, films referred hereafter as hydro-oxygenated  $\text{TiO}_x:\text{OH}$  films.

Results of an investigation of the electrical and hydrophilic properties in connection with OH group content of the  $\text{TiO}_x:\text{OH}$  films obtained by PECVD in  $\text{H}_2/\text{O}_2$  plasma were reported in different paper [44]. It has been shown that the  $\text{TiO}_2$  thin films obtained by PECVD had good hydrophilicity after ultraviolet UV light irradiation, low dark, and high photoexcited currents in vacuum and high sensitivity of their dark and photoexcited currents to surface adsorbates. Low dark and high photoexcited currents measured in vacuum for the  $\text{TiO}_x:\text{OH}$  films were explained by the effect of inactivation of the defect states such as dangling bonds by the termination of OH group. The sensitivity of the photoexcited currents to surface adsorbates noticed for the  $\text{TiO}_x:\text{OH}$  films suggests that the surface potential is modified in response to electron affinity of the surface adsorbates during UV light irradiation. This effect contributes to generation of oxidants due to interaction between photoexcited carriers and surface adsorbates and, hence, improves the hydrophilicity of the  $\text{TiO}_x:\text{OH}$  films.

The plasma reactor used in PECVDs of  $\text{TiO}_x:\text{OH}$  thin films is presented schematically in Fig. 1. The cylindrical chamber of the reactor with the inner diameter of 17 cm and length of 47 cm was connected to a quartz tube with the inner diameter of 4.5 cm and the length of 100 cm. The length of the quartz tube inside the reactor chamber was 14 cm, while the distance between deposition substrate and the end of the quartz tube in the reactor chamber was 10 cm. The source plasma was generated by a microwave discharge in  $\text{H}_2/\text{O}_2$  gas in the quartz tube at distance  $d = 50$  cm from the substrate. The  $\text{H}_2$  and  $\text{O}_2$  gases were fed into the system through mass flow controllers (MFCs). Among the plasma-generated chemically active species (radicals), only long lifetime radical H and OH species can reach the film deposition region because of remote plasma configuration. Light emission spectroscopy measurements of intensity of emission lines 656.2 nm of H and 309 nm of OH radicals were used to follow the dependence of these radical atom concentrations on the  $\text{H}_2/\text{O}_2$  gas composition. The source gas, vapor of titanium tetraisopropoxide (TTIP), was introduced into the chamber through a bubbling cylinder by He carrier gas. To prevent condensation of TTIP vapor, the bubbling cylinder and transfer tubes were kept at 75 °C and 95 °C, respectively. The substrate was heated by a heater with a thermocouple sensor for the control of temperature. Typical deposition parameters are shown in Table 1. Film thickness was monitored by in situ He-Ne laser interferometer and confirmed by ellipsometry, which also estimated refractive index of the deposited films. The deposition rate was proportional to the TTIP flow rate, which suggests that  $\text{H}_2/\text{O}_2$  plasma produced enough radical H and OH

species to dissociate TTIP molecules in the gas phase. The effect of the plasma gas composition on the deposition rate was studied by fixing the total gas flow rate at 60 sccm and changing the flow rates of H<sub>2</sub> and O<sub>2</sub>. The deposition rate in the cases of H<sub>2</sub> or O<sub>2</sub> single gas plasmas were very low, 0.19 and 0.16 nm/min, respectively. However, the deposition rate increased drastically in the H<sub>2</sub>/O<sub>2</sub> mixture gas plasma, reaching the highest value of 11 nm/min for 20% O<sub>2</sub> and 80% H<sub>2</sub> gas composition. The substrate temperature had little influence on the deposition rate, but affected strongly the film structure. The FT-IR spectra of the films obtained at various substrate temperatures showed that the OH group content in the films decreased significantly and the Ti–O–Ti bond peak sharpened by increasing of the substrate temperature. Moreover, increasing the substrate temperature caused the deposition of films with high refractive index (2.4 at 580 K) and small optical band gap (1.93 eV at 580 K). The TiO<sub>x</sub>:OH films deposited by PECVD were amorphous and showed good photocatalytic activity {see the selected paper P1 and references [43] and [44]}.

The author (L. Sirghi) has shown that TiO<sub>x</sub> thin films with similar properties can be obtained also by RFMSD (see the selected paper P2). Magnetron sputtering deposition is known as a reliable method of fabrication of ceramic films with a good chemical stability and an excellent adherence to the substrate. The RFMSD TiO<sub>x</sub> thin films have been obtained by sputtering of a cathode target (a sintered TiO<sub>2</sub> disk with the diameter of 10 cm) in a 200 W power radio frequency discharge in Ar (6 sccm) and O<sub>2</sub> (0.6 sccm) gas mixture at pressure values of 1, 4 and 10 mTorr. Figure 2 presents a sketch of the experimental apparatus. The cylindrical chamber of the magnetron with 39 cm in diameter 19 cm in height was connected to a vacuum system (minimum pressure of 10<sup>-6</sup> Torr) and a gas supply system with mass flow controllers (MFCs) for Ar and O<sub>2</sub> gases. The substrate holder including a heating system was installed at 10 cm in front of the cathode. A cylindrical Langmuir probe consisting of a 5-mm-long tungsten wire with the diameter of 0.15 mm was placed at a distance of 1 cm from the substrate holder and used to determine the plasma density, the electron temperature and the plasma potential in the deposition region. The films were deposited during 3 hours on Si(100) wafers heated to 270°C. Values of parameters of deposition plasma (density, potential, electron temperature, and computed ion flux density) and film properties (thickness and refractive index) at three values of gas pressure are presented in Table 2. The increase of working gas pressure resulted in increase of plasma density, decrease of electron temperature and plasma potential, and an increase of flux density of low energy Ar<sup>+</sup> ions. A careful

investigation of dependence of RFMSD plasma parameters on gas pressure and flow rate is reported by Sirghi et al in [45].

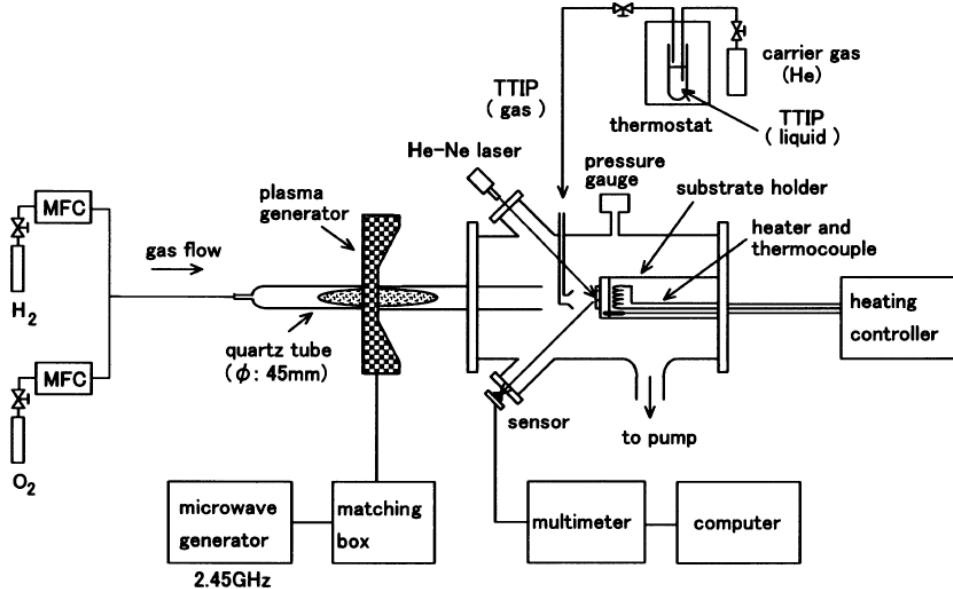


**Fig. 1 Sketch of the PECVD setup used for synthesis of titanium oxide hydro-oxygenated, TiO<sub>x</sub>:OH, thin films [43].**

**Table 1. Typical values of PECVD parameters**

deposition parameters	typical values
Microwave (2.45 GHz) power	500 W
O <sub>2</sub> flow rate	12 sccm <sup>2</sup>
H <sub>2</sub> flow rate	48 sccm <sup>2</sup>
gas pressure	0.1 torr
TTIP vapor flow rate	0.4 sccm
He flow rate	5 sccm
Substrate	p-Si(100), quartz
Substrate temperature	room temperature – 400 °C

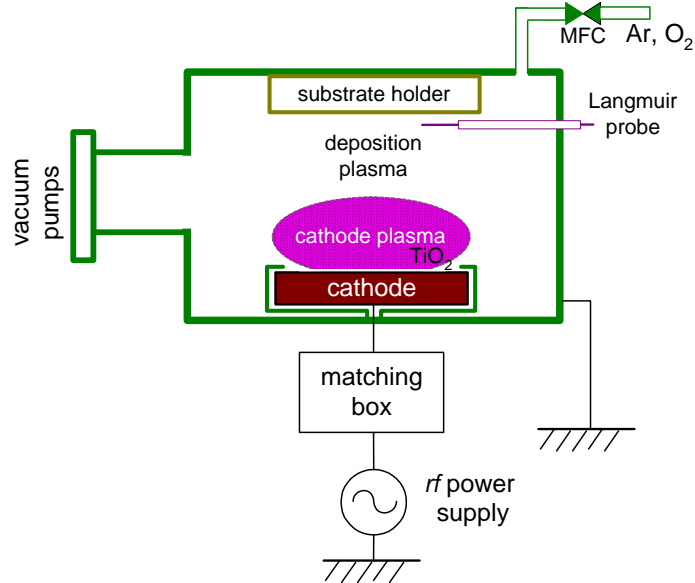


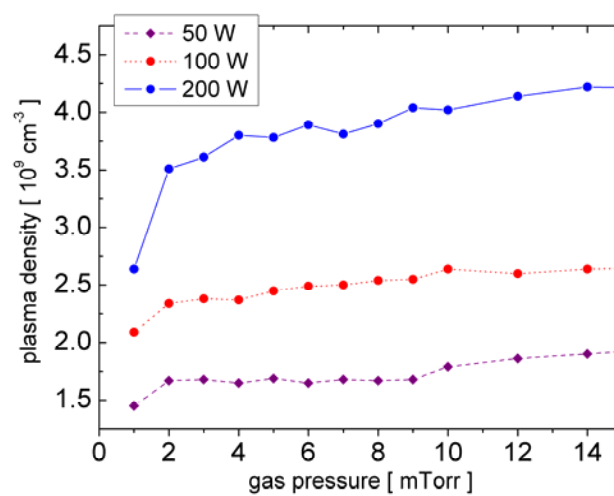
**Fig. 2 Sketch of the experimental setup used in RFMSD of  $\text{TiO}_2$  thin films.**

**Table 2 Values of plasma parameters and film thickness (corresponding to a deposition time of 2h) and refractive index at three values of deposition pressure.**

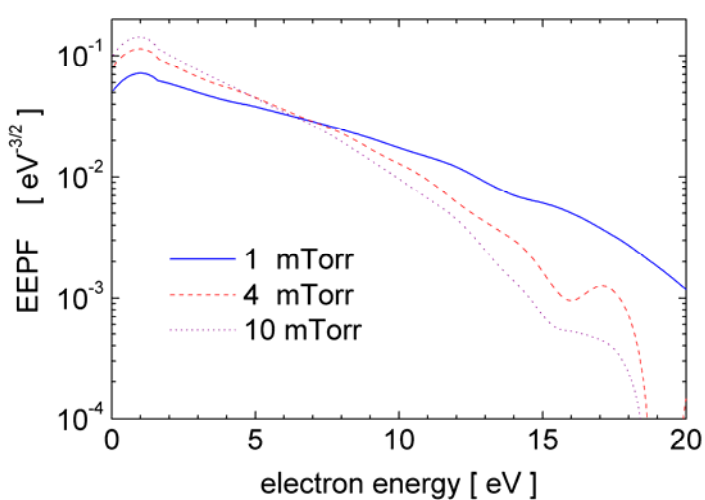
Sample	gas pressure [mTorr]	film thickness [nm]	refractive index	plasma density [ $10^9 \text{ cm}^{-3}$ ]	electron temperature [eV]	plasma potential [V]	flux density of low-energy ions [ $10^{14} \text{ cm}^{-2} \text{s}^{-1}$ ]
a	1	400	1.72	2.6	4.1	5.4	1.4
b	4	180	2.13	3.5	3.7	4.5	1.65
c	10	160	1.83	4	3.2	4.3	1.75

Figure 3 shows the dependence of plasma density on the gas pressure, while Fig. 4 shows the electron energy distribution function (EEDF) measured by Langmuir probe at three values of gas pressure. The slope of EEDF increases with the increase of the working gas pressure, at high gas pressure (10 mTorr) the EEDF being depleted in high-energy electrons. These changes in EEDF are reflected also by dependence of electron temperature values in Table 2. Variation of the pressure of the working gas has a big impact not only on plasma parameters, but also on the crystalline structure of the deposited films. The XRD patterns (Fig. 5) show no diffraction peak for the film deposited at 10 mTorr (sample c) and weak peaks at  $27.5^\circ$ , which are attributed to rutile (110), for the films deposited at 4 mTorr and 1 mTorr (sample b and a, respectively). Results of Fourier transform infrared (FTIR) spectroscopy confirmed the results of the XRD investigation. Thus, the FTIR spectra (not shown) for the films deposited

at low pressure values (1 and 4 mTorr, respectively) showed two absorption peaks (507 and 397 cm<sup>-1</sup>) that are attributed to vibrations of Ti-O-Ti bonds in the octahedral structures of crystalline TiO<sub>2</sub>, while the FTIR spectra of the film deposited at 10 mTorr show a single broad absorption peak (at 447 cm<sup>-1</sup>) attributed to Ti-O-Ti vibrations in an amorphous structure.



**Fig. 3 Dependence of the plasma density on the argon pressure at three values of the discharge power (argon flow rate was 4 sccm)**



**Fig. 4 Electron energy probability function (EEPF) at three values of Ar pressure (the argon flow rate was 4 sccm).**

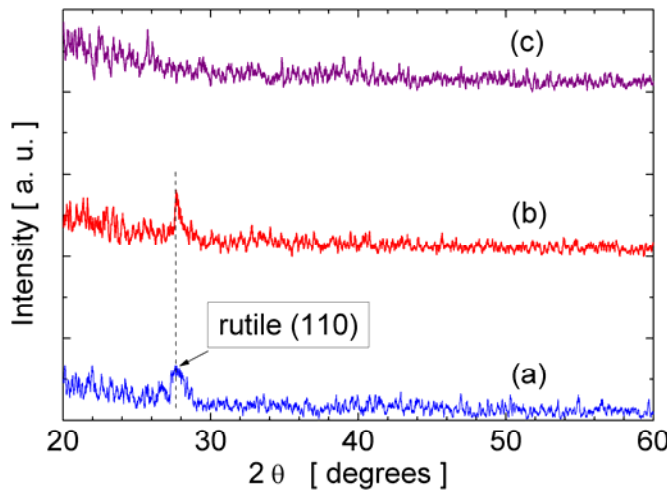


**Fig. 5** The XRD spectra for the films obtained by RFMSD at Ar-O<sub>2</sub> gas pressure of 1 (sample a), 4 (sample b) and 10 mTorr (sample c).

Differences in the crystallinity of the deposited films can be explained by the gas pressure related changes of energetic particle bombardment of the film surface. It is known that the positive ion bombardment of the surface of a growing film increases the mobility of the adatoms, which leads to a more compact film microstructure [46]. However, the crystalline films were obtained for low values of the gas pressure (1 and 4 mTorr), when the flux density of the positive ions coming from the plasma was smaller. This apparent discrepancy is cleared by the observation that the energy of these positive ions coming from the plasma and accelerated in the ion sheath formed at the plasma-film interface is low. Then, the film surface impingement by these low-energy ions can induce a mobility of the adatoms only at a short-range scale, which is not sufficient for formation of crystalline microstructures. Growing of crystalline films on a longer scale is related more to the high-energy particle impingement of the film surface [47]. The change in the gas pressure in RFMSD plasma results also in a change in the film surface bombardment by the energetic particles coming directly from the magnetron target [48]. Such particles can be sputtered O<sup>-</sup> ions accelerated in the cathode sheath nearby the target, energetic backscattered Ar<sup>+</sup> ions [49], and electrons escaped from the magnetic trap of the magnetron cathode. Finding of a dependence of the film structure on the radial position of the substrate in RFMSD of TiO<sub>2</sub> at low discharge pressure has been attributed to the impingement of the film surface by the high-energy particles that come from the cathode region of the discharge [50]. Because of the scattering collisions, the increase of the gas pressure should weaken the flux of high-energy particles going from the cathode region of the magnetron discharge towards the growing film.

Therefore, increase of the gas pressure results in an enhancement of the high-energy particle scattering through the elastic collisions with the background gas atoms, which leads to a decrease of high-energy particle bombardment of the film surface. At low gas pressure (1 mTorr) the film structure is affected more by the high-energy particles than by the low-energy ions coming from the nearby plasma, which explains the crystalline structure of this film. By increasing of the gas pressure, the growing of an amorphous film is favored because of a weak impingement of the film surface by the high-energy particles.

The mesoscopic structure of the RFMSD films determines their photocatalytic activity and thus the hydrophilicity of their surfaces after UV irradiation. The UV-light-induced hydrophilicity of  $\text{TiO}_2$  is related to the dissociative adsorption of water molecules from the ambient air at  $\text{Ti}^{4+}$  photoreduced to  $\text{Ti}^{3+}$  sites, which typically are situated at the oxygen bridges on the surface [2]. Immediately after deposition the films showed hydrophilic surfaces. After storage in dark the films became less hydrophilic showing water contact angle values around  $70^\circ$ . One hour irradiation of the films by UV light at  $3 \text{ mW/cm}^2$  intensity in atmospheric air at relative humidity (RH) of 45% and temperature of  $22^\circ\text{C}$  induced the changes of the water contact angle that are shown in Fig. 6. The film deposited at 10 mTorr (sample *c*) and the reference PECVD film (sample *d*) showed a very low water contact angle (around  $4^\circ$ ), which is indicating a very good UV-light-induced hydrophilicity (photocatalytic activity) of these films.

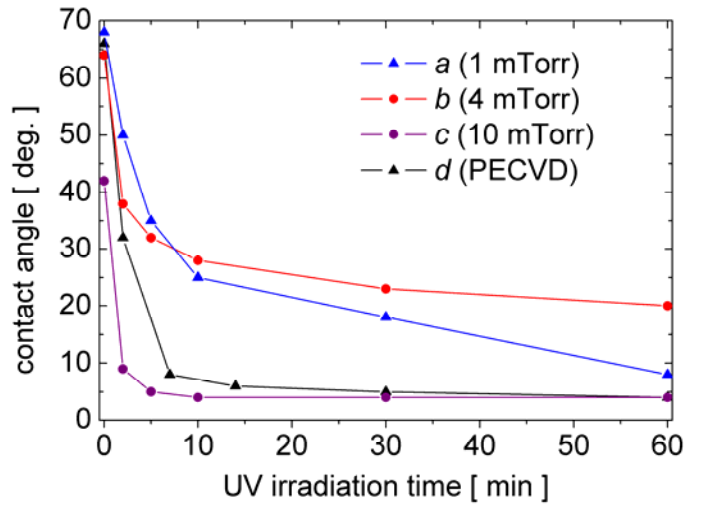


**Fig. 6** UV-light-induced modification of the water contact angle of the  $\text{TiO}_2$  thin films. Plots represent the water contact angle dependence on the UV light irradiation time for the films obtained by RFMSD in  $\text{Ar}/\text{O}_2$  gas at pressure of 1 mTorr (**a**), 4 mTorr (**b**) and 10 mTorr (**c**), and for the PECVD film used as reference (**d**).

The films deposited at lower gas pressure values (samples *a* and *b*) showed larger water contact angles after UV light irradiation, which indicates a lower photocatalytic activity for these films.

The UV induced hydrophilicity of deposited TiO<sub>2</sub> thin film surfaces has been studied microscopically by FFM measurements. In selected paper P1 [35] Sirghi et al showed that the AFM measurements of the tip-sample adhesive force in air could be used to differentiate regions of different wettability on the TiO<sub>2</sub> film surface. The adhesive force generated by the capillary and superficial tension forces of the water meniscus, which is formed by capillary water vapor condensation at the tip-sample contact, depends strongly on the size and shape of the meniscus. Figure 7 illustrates the dependence of capillary adhesive force on surface hydrophilicity of an AFM sample. Large water menisci and tip-sample adhesive force values correspond to AFM tip contacts with hydrophilic regions of the sample, while smaller menisci and adhesive force values correspond to less hydrophilic (or hydrophobic) regions of the sample. Because of the capillary condensation of water vapor, the friction force between a hydrophilic AFM tip and a sample surface also depends on the sample surface hydrophilicity (see [38] and the selected paper P8). An explanation of the effect of the wetting of the AFM tip-sample contact on the friction force was given by Fogden and White, which generalized the Hertz theory to include the normal load created by

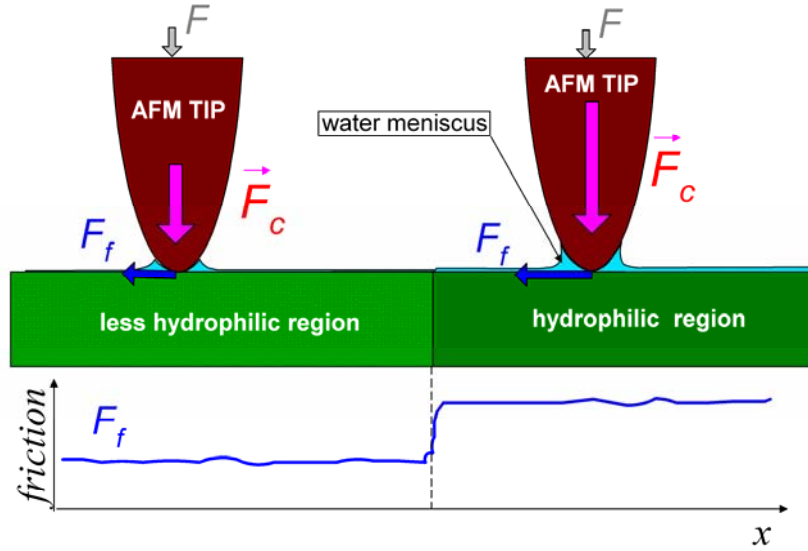


**Fig. 7** Illustration of friction force microscopy technique used to differentiate nanoscopic regions of different hydrophilicity on a sample surface. The AFM tip is pressed onto sample surface by a small and constant force  $F$ . The water meniscus formed by capillary condensation of water vapor in air on the nanoscopic gap between AFM tip and sample surfaces generates an adhesive capillary force,  $F_c$ , which depends on sample surface hydrophilicity. Thus, the friction force,  $F_f$ , is larger on hydrophilic regions due to large value of  $F_c$  and smaller in less hydrophilic regions due to smaller values of  $F_c$ .

the capillary and superficial tension forces of the capillary water meniscus at the contact [51] (see Fig. 7). If the normal loading force applied externally on the tip-sample contact is kept weak (much smaller than the normal loading force generated by the capillary meniscus), the friction force depends strongly on the wetting of the tip-sample contact and its value can be used as a measure of the sample hydrophilicity. Figure 8 shows the results of FFM measurements in air at RH = 45% performed on an area of  $2000 \times 2000 \text{ nm}^2$  of the surface of the sample *a* before and after UV light irradiation. The histograms and the images of the friction force in the inset show a relatively homogeneous surface before UV irradiation (the left part of the inset) and an inhomogeneous surface after UV irradiation (the right part of the inset). The friction force histogram for the sample surface before UV light irradiation shows a single peak resembling the Gauss distribution (apart for a distortion on the high-value side), which is indicating a relatively homogeneous surface. The friction force histogram for the sample surface after UV light irradiation shows a distribution shifted towards larger friction force values with two peaks, which proves the occurrence of regions of two different photocatalytic activities on the surface of this sample. By the UV light irradiation, the friction force values increased allover the sample surface, but they increased differently on the two different region types of the sample surface. Measurements of the tip-sample adhesive force on the two regions types of the UV-light irradiated sample surface showed that large adhesive force values correspond to large friction force values, while low adhesive force values correspond to low friction values. This proves that the FFM measurements can be used as well as the AFM tip-sample adhesive force measurements to distinguish microscopically regions of different hydrophilicity (photocatalytic activity) on the surface of the TiO<sub>2</sub>.

The result of the AFM and FFM measurements for the films obtained by RFMSD at the gas pressure values of 1 mTorr (*a*), 4 mTorr (*b*) and 10 mTorr (*c*), respectively, and for the reference film (*d*) after their UV light irradiation are presented in Fig. 9. The images of the surface topography (left part) show the occurrence of large grains ( $200 \times 200 \text{ nm}^2$  in area) on the film deposited at low gas pressure (*a*) and much smaller grains on the films deposited at larger gas pressure values (*b* and *c*). On the corresponding friction force images (right part), one observes inhomogeneous distributions with low friction force on some of the grains of the samples *a* and *b*. The RFMSD film deposited at low gas pressure shows the most inhomogeneous surface with small friction force values on the large grains and large friction force values between the large grains.

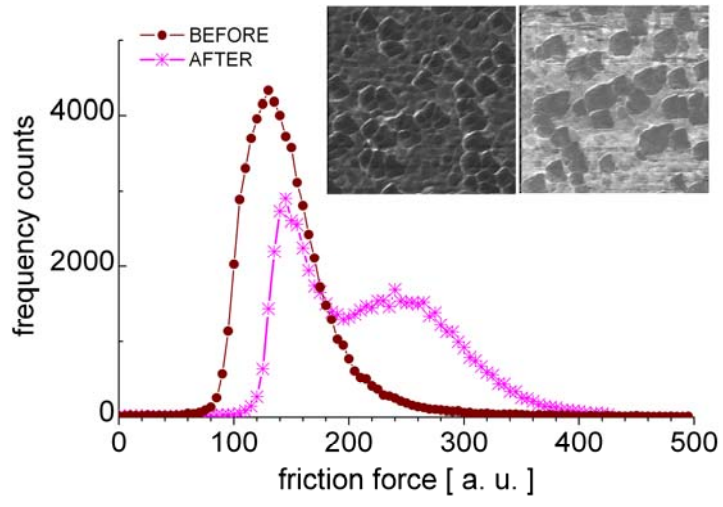


**Fig. 8** The histograms of the friction force values on an area of  $2000 \times 2000$  nm $^2$  of the surface of sample *a* before and after it was irradiated by UV light. The inset shows the friction force images before (left part) and after (right part) UV irradiation. The film deposited at 10 mTorr gas pressure shows a relatively homogeneous distribution of the friction force on its surface, but its surface smoothness and homogeneity are inferior to those of the surface of the reference sample (*d*).

These results are in agreement with the results of XRD and FTIR investigation of the film structure. The FFM measurements show the occurrence of mixed crystalline and amorphous microstructure in the film deposited at low pressure (sample *a*). The strong high-energy particle impingement during this film deposition led to the formation of crystalline microstructures at a relatively long-range scale (200 nm). It is difficult to establish which of the two microstructure types has a higher photocatalytic activity. However, by comparing of the results of FFM measurements of the samples *a* and *c*, one concludes that the amorphous phase has the best photocatalytic activity. This result is explained by the fact that the amorphous phase (with short-range order of anatase type) has a higher density of oxygen bridging sites on its surface than the crystalline (rutile) phase.

The selected paper P3 [7] reports the results of study of the dependence on thickness of photocatalytic activity (UV-light-induced hydrophilicity) of amorphous titanium dioxide thin films obtained by RFMSD. This study presents practical and theoretical motivations. A major drawback of the sputtering deposition is its relatively low deposition rate (typically, few nm/min) at a high cost. Therefore, a study of the film photocatalytic property in connection to the film thickness is important in order to establish the minimum film thickness at which good surface properties are achieved. Besides this practical interest, the study has also a theoretical importance.

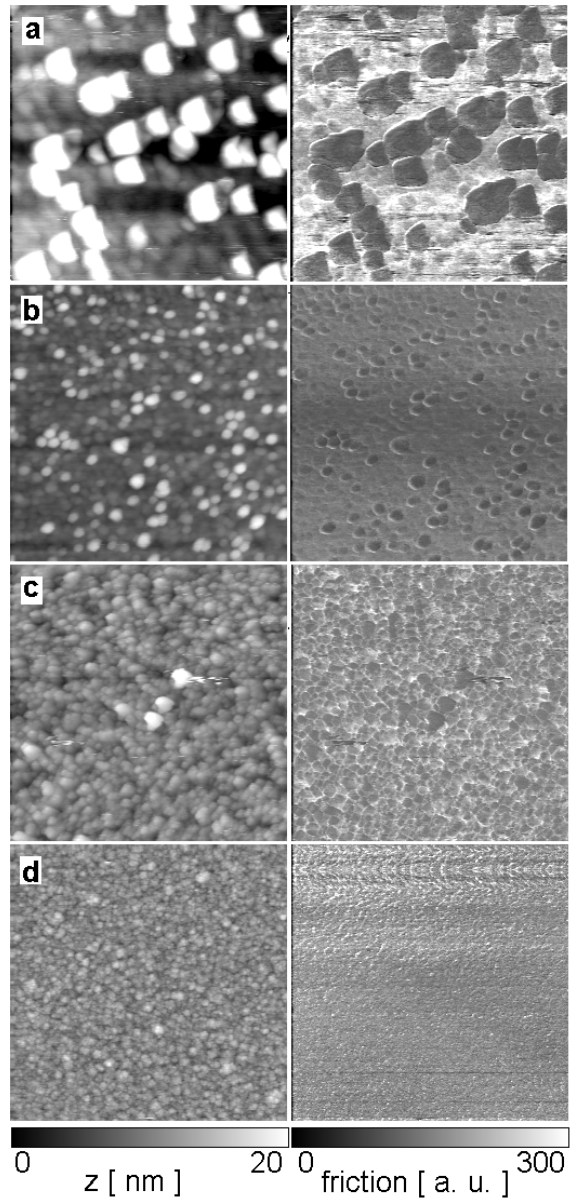


**Fig. 9** Images of the surface topography (left) and of distributions of the friction force (right) for  $\text{TiO}_2$  films obtained by RFMSD in  $\text{Ar}$ (6 sccm) and  $\text{O}_2$ (0.6 sccm) gas mixture at pressure of 1 mTorr (a), 4 mTorr (b) and 10 mTorr (c), and for the PECVD film used as reference (d), after the films were irradiated by UV light. The scanned area is  $2000 \times 2000 \text{ nm}^2$  for all images.

The efficacy of UV light irradiation in changing the  $\text{TiO}_2$  wettability may be related not to the formation of anion vacancies at the surface, which according to recent STM measurements is low [52], but more to the formation of charge carriers in the bulk and their transportation to the surface where they interact with the adsorbate molecules. Observation of a relation between the UV-light-induced hydrophilicity and generation, recombination and transport of the electric charges in  $\text{TiO}_2$  films has been reported in [53]. In very thin films

(thickness smaller than 100 nm) the charge transport may be affected drastically by the spatial charge separation caused by the energy band distortion at the film interfaces [54].

It has been found that the effect of UV light irradiation on hydrophilicity of TiO<sub>2</sub> films thicker than a threshold value of about 12 nm was fast, strong and did not depend on substrate or thickness. For thinner films, the UV induced hydrophilicity was weak and dependent on substrate or film thickness. Irradiation of the films by UV light at 3 mW/cm<sup>2</sup> intensity in atmospheric air at relative humidity (RH) of 40% and temperature of 22°C induced the changes of the water contact angle that are shown in Fig. 10. The weak effect of UV light irradiation observed for the ultra-thin films (with thickness less than 12 nm) has three main causes. Firstly, the ultra-thin films (thickness lower than 12 nm) have a smoother surface, possibly with a lower density of defects, which may make their surface less photocatalytic. Secondly, the ultra-thin films can absorb only partially the incident UV light radiation. Lastly, the ultra-thin films may be less photocatalytic because of the charge separation caused by the energy band distortion at the film interfaces. First cause is indicated by the results of topography analysis of AFM images of surfaces of the deposited films. The thickness and root mean square (RMS) roughness of the films deposited on Si(100) substrate are given in the Table 3. The film roughness increased by the increase of the film thickness as an effect of the grain growing during the deposition.

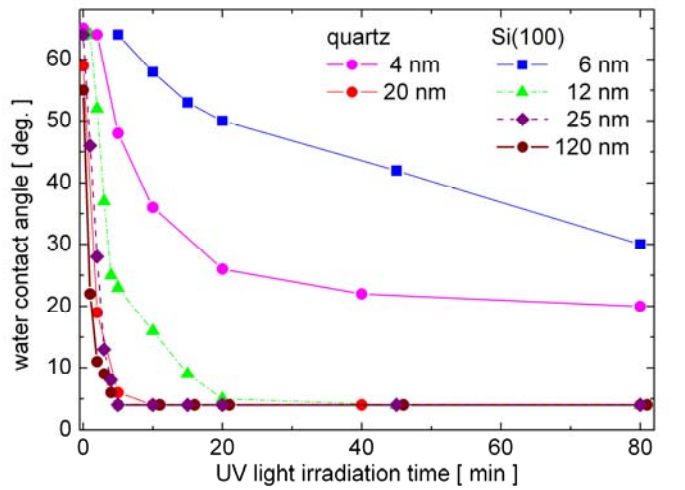


**Fig. 10 Dependence of water contact angle on the time of UV light irradiation (3 mW/cm<sup>2</sup>) of the TiO<sub>2</sub> thin films in air at RH of 40% and temperature of 22°C.**

**Table 3 Thickness and root mean square roughness of the TiO<sub>2</sub> thin films deposited on Si(100) substrate.**

Deposition time [ min ]	5	10	20	40	120
Thickness [ nm ]	6	12	25	45	120
RMS roughness [ nm ]	0.16	0.25	0.35	0.59	0.8

Figure 11 presents the topographic images of the surfaces of the films deposited on Si(100) for 5 minutes (left part) and 40 min (right part), respectively. The insets show high-resolution images resulted by scans of  $50 \times 50 \text{ nm}^2$  area of the sample surfaces. The images show the onset of the grain formation on the surface of the film deposited in 5 minutes (film thickness of 6 nm) and fully developed grains on the surface of the film deposited in 40 minutes (film thickness of 45 nm). The typical diameter and height of the fully developed grains were estimated to 16 nm and 1 nm, respectively, values that compute a typical grain curvature radius of 30 nm. Formation of grains on the film surface may have a strong effect on the film surface properties, since the surface with fully developed grains have larger real area and a higher density of defects than the smooth surface. To investigate the second possible cause, optical transmission spectroscopy measurements in UV domain were performed and the results are shown in Fig 12.

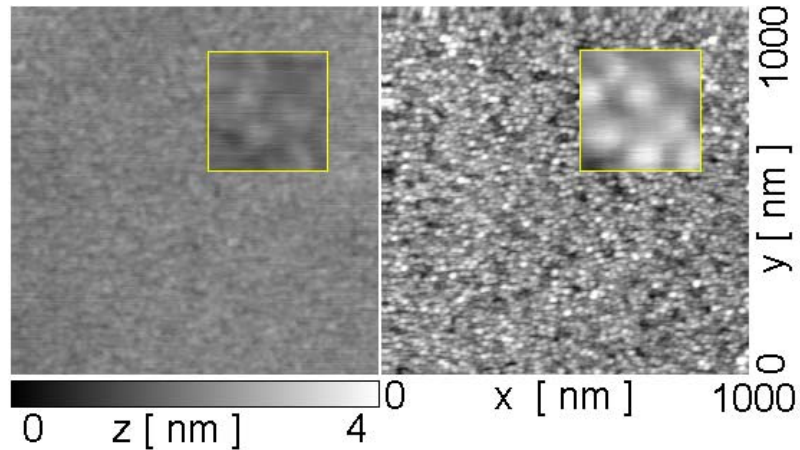


**Fig. 11 Surface topography images for the films with thickness of 6 nm (left part) and 45 nm (right part), respectively, deposited on Si(100). The insets show high-resolution images resulted by scans of  $50 \times 50 \text{ nm}^2$  area of the film surfaces**

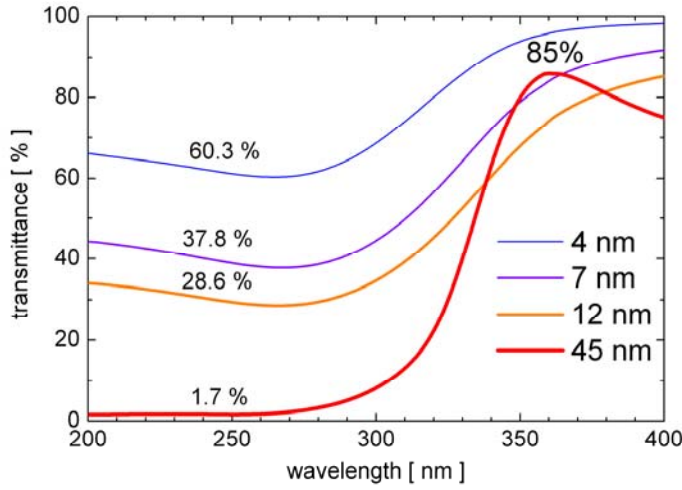


**Fig. 12 Optical transmittance of the films deposited on quartz with different values of the thickness. The values on the plots correspond to the film transmittance at the wavelength of 260 nm.**

The transmittance of the films with thickness of 4, 7, 12 and 45 nm, respectively, deposited on quartz depended strongly on their thickness, which shows that the ultra-thin films adsorb partially the incident UV radiation. By estimating the reflection coefficient of the film interfaces to 15%, it is deduced that the film with the thickness of 12 nm adsorbs less than 60% of the incident UV radiation while the film with the thickness of 45 nm adsorbs almost the whole incident UV radiation.

The last of the causes that could made the ultra-thin films less photocatalytic is related to the charge separation caused by the energy band distortions at the film interfaces. The film interfaces are likely to contain a large number of defects, which are most probably donor sites [55] and can be easily ionized during UV light irradiation. Also, the adsorbed oxygen molecules at the film surface may capture photoelectrons from the conduction band and generate a bounded negative charge on the film surface. Therefore, when the film is irradiated by UV light a space charge is likely to be built at both film interfaces. A space charge at the film surface distort the energy bands over a distance equal to the Debye length, which at a relatively low density of the photoelectrons in the conduction band ( $10^{17} \text{ cm}^{-3}$ ) is comparable with the thickness of the ultra-thin film. Therefore, for the ultra-thin films it is expected an energy band distortion along their whole thickness, a phenomenon that creates charge separation and prevents the holes or electrons to reach the film surface. This charge separation may have a strong effect on the photocatalytic property of the film surface, since it diminishes one of either the reduction power of the electrons from the conduction band or

oxidation power of the holes from the valence band. The charge separation can be proved by experiments on decay of the photocurrent after stopping of the UV light irradiation. If the space charge separation occurs across the whole film, the recombination probability is low and a longer lifetime for the photogenerated holes and electrons is expected. The plots in Fig. 13 showing the time dependence of the photocurrent measured in vacuum ( $10^2$  Torr) during an on-off cycle of UV light irradiation ( $0.4 \text{ mW/cm}^2$ ) confirm this supposition. The plots show much longer decay time values for the photocurrent in very thin films (thickness of 4, 20 nm) comparing to that for the photocurrent in a thick film (thickness of 110 nm). The measurements were performed by applying a voltage of 60 V to a gap (3mm in width and 10mm in length) between two gold electrodes that were deposited by sputtering on the top of the each film (on quartz substrate). The steep decay of the photocurrent in the thick film (immediately after the UV light irradiation was turned off) is attributed to the short lifetime of the photogenerated carriers in the bulk region of the film, where there is no space electrical charge. The long lifetime of the photogenerated carriers in the ultra-thin film is attributed to the charge separation, which is more effective in these films due to their small thickness.

In the selected paper P4, Sirghi et al [39] reported results of a study of the energy transferred by plasma to the deposited films and substrates. The study was motivated by observation of polymer surface buckling instability in case of RFMSDs of  $\text{TiO}_2$  thin films on polymethyl methacrylate (Plexiglas) and polycarbonate substrates.

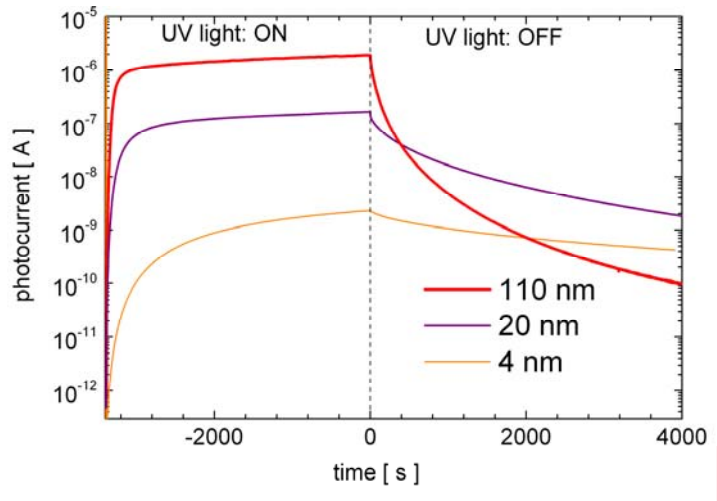


**Fig 13 Time dependence of photocurrent in vacuum during an on-off cycle of UV light irradiation for the films with thickness of 4, 20 and 110 nm deposited on quartz.**

It has been found that the energy flux transported by plasma particles and radiation impinging on the film surface had a big impact not only on film properties, but also on the polymer substrate surfaces, which showed surface buckling instability. Sirghi et al [39] used a dummy substrate consisting of a thermal probe [56, 57] to determine the energy flux that is transported by plasma particles and plasma radiation towards a polymer substrate and TiO<sub>2</sub> film surface during RFMSD. The probe temperature was measured by a thermocouple and the energy transported by plasma to the substrate was evaluated based on the energy balance at the surface of the negatively biased probe. This method allowed for an evaluation of the energy flux that is transported by charged plasma particles towards the surface of an electrically insulated substrate (polymer) along with the energy flux that is transported by other processes (thermal radiation from the cathode target, plasma light radiation, bombardment with excited neutral particles, etc). The temperature of the polymer substrate surface was estimated on the basis of the thermal probe measured values of the energy that is transported by plasma towards an electrically floating substrate. For the experimental conditions of RFMSD, the values of polymer surface temperature were much below the polymer melting temperature. This pointed towards the important role of argon ion bombardment in driving of the polymer surface buckling instability. The instability on polycarbonate and polymethyl methacrylate (Plexiglas) substrates exposed to the deposition plasma was studied by AFM measurements, which revealed increase of the roughness of substrate surfaces by the increase of total energy transferred by plasma to the deposition substrate.

Figure 14 presents a sketch of the experimental setup used for determination of the energy flux density that is transported by plasma towards the deposition substrate surface used for TiO<sub>2</sub> thin film RFMSD. A thermal probe and a surrounding shield made of stainless steel foil (0.1 mm in thickness) were mounted on the axis of the magnetron discharge chamber at a distance of 4 mm from the substrate holder (see Fig. 14). The thermal probe consisted in a square stainless steel foil (0.1 mm in thickness) with the area of 8×8 mm<sup>2</sup>. A thermocouple was welded on the backside of the probe to secure a good thermal and electric contact. The thermal probe was negatively biased by an electrical biasing circuit consisting of a current probe resistor (R) and a direct current power supply source. To avoid any interference between the thermocouple circuit and the probe biasing circuit, the probe temperature was measured immediately after the biasing circuit was disconnected by an electric switch (K) inserted in the probe biasing circuit. The polymer substrates used were

wafers of polycarbonate and Plexiglas with the thickness of 1 mm. The substrates were mounted in thermal contact with the substrate holder. The temperatures of the substrate holder and deposition chamber were monitored by thermocouples.

In the energy balance of the film surface, considered at floating potential,  $V_f$ , with respect to plasma potential,  $V_p$ , the plasma ions contribute with an average kinetic energy  $T_e + e \cdot V_f$ , where  $T_e$  is the electron temperature expressed in  $eV$ , and  $e$ , the electric charge of a positive ion. Moreover, the ions reach the film surface in equal number with the electrons and they recombine releasing for each recombination energy equal to  $eV_i$ , where  $V_i$  is the ionization potential of atoms. The ion kinetic energy, the electron kinetic energy and the energy released in surface recombination are all absorbed by the substrate surface and assimilated to the thermal heat transferred to the substrate surface by charge particle

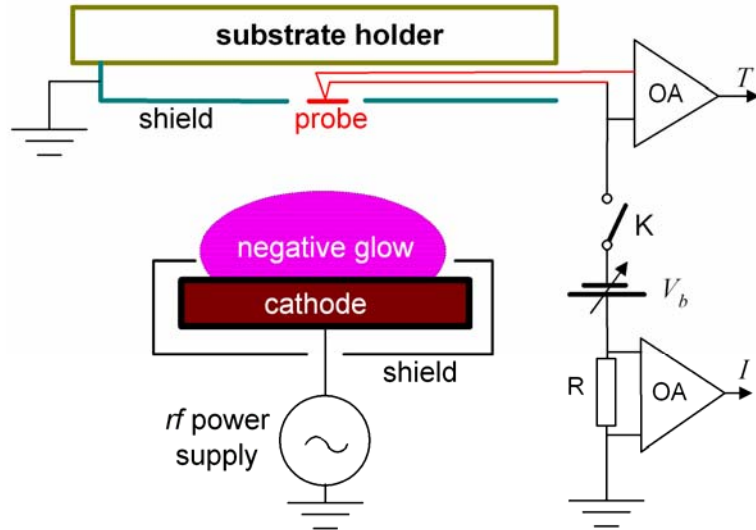


**Fig. 14** Sketch of the experimental setup used to study the energy transfer from r.f. magnetron plasma to the film surface. Differential operational amplifiers (OA) are used to process the electrical signals corresponding to the probe temperature,  $T$ , and probe current intensity,  $I$ . The probe was kept either electrically biased against the ground (discharge chamber) at the potential  $V_b$ , or floating at the potential  $V_f$ .

bombardment. Therefore, the energy flux density that is transferred to the surface of a floating film (or substrate) surface by electrically charged particles,  $q_{ch}$ , may be expressed by

$$q_{ch} = j_{iB} \cdot (V_f + V_i + 2T_e / e), \quad (1)$$

where  $j_{iB}$  is the Bohm density of the ion current,

$$j_{iB} = e \cdot n \cdot \sqrt{T_e / m_i}, \quad (2)$$

$n$ , the plasma density nearby the substrate and  $m_i$ , the mass of positive ions. For an electrically conductive substrate biased to a potential  $V_b$  more negative than  $V_f$ , the contribution of the electron flux may be neglected (most of the electrons do not reach the substrate) and Eq. (1) may be written as:

$$q_{ch}(V_b) = j_i \cdot (V_b + V_i + T_e / e) \quad (3)$$

Here,  $V_f$  and  $V_b$  are taken as absolute values, with plasma potential as the reference potential, and  $j_i$  depends on  $V_b$ . Besides the substrate heating by charge particle, there are other processes of energy transfer to the film surface, as surface de-excitation of metastable atoms, surface reaction of radical molecules, UV, VIS and thermal radiation adsorption. The energy flux density that is transferred to the substrate surface through all these processes is referenced hereafter as  $q_0$ . In contrast with  $q_{ch}$ , which can be evaluated based on the plasma parameter measurement,  $q_0$  is much difficult to be determined.

Because of energy transfer from plasma towards the substrate, the temperature of the film surface increases until a thermal equilibrium is reached, when the inward flux of energy,  $q_{ch} + q_0$ , is equal to the outward flux of energy (energy loss). The substrate surface loses energy by radiation (the thermal energy flux density that is lost by radiation is  $q_r$ ) and conduction (the thermal energy flux density that is lost by conduction is  $q_c$ ). At thermal equilibrium, the following condition is fulfilled:

$$q_{ch} + q_0 = q_r + q_c. \quad (4)$$

The flux density of the thermal energy lost by radiation is

$$q_r = \sigma \cdot (\varepsilon_s T_s^4 - \varepsilon_{env} T_{env}^4), \quad (5)$$

where  $\sigma = 5.67 \cdot 10^{-8} \text{ Wm}^{-2}\text{K}^{-4}$  is the Stefan-Boltzmann constant,  $\varepsilon_s$ , the thermal emittance of the substrate surface,  $T_s$ , the absolute temperature of the substrate surface,  $\varepsilon_{env}$ , the thermal emittance of the environment (deposition chamber) and  $T_{env}$  the absolute temperature of the environment. The thermal energy lost by conduction includes the energy loss by thermal conduction of the substrate towards the substrate holder and the energy loss by thermal conduction of the gas in the deposition chamber. Because the thermal conductivity of the gas at the low pressure in the discharge chamber (less than 10 mTorr) is very low, only the loss of thermal energy by thermal conduction of polymer substrate is taken into the account. The floating thermal probe was as a dummy deposition substrate (Fig. 14) in order to determine

the energy transferred by plasma to the substrate. The thermal probe was thermally insulated, so that  $q_c \equiv 0$ , and the energy balance equation for the probe surface was

$$q_r = q_{ch}(V_b) + q_0, \quad (6)$$

where  $q_{ch}(V_b)$  is given by Eq.(3). A factor of 2 was considered in the expression of  $q_r$  to account for the loss of thermal energy by radiation at both probe surfaces (one faced to the plasma and one faced to the substrate holder (Fig. 14).

$$q_r = 2\sigma \cdot (\varepsilon_s T_s^4 - \varepsilon_{env} T_{env}^4). \quad (7)$$

The temperatures  $T_s$  and  $T_{env}$  were measured by probe and discharge chamber thermocouples, respectively, and their values were used to compute  $q_r$ , which for this case were equal to the total energy flux density transported by the plasma to the substrate (thermal probe) surface. When the thermal probe was electrically insulated (floating), it simulated the thin film surface. The values of  $q_{ch}$  and  $q_0$  can be discriminated by biasing negatively the thermal probe. By biasing the probe at a very negative  $V_b$ , the contribution of electrons to the probe heating was eliminated and the only charged particles that heated the probe surface were the positive ions. According to the Eqs (3) and (10), the quantity  $q_r/j_i$  should increase exactly with the increase of  $V_b$ .

$$q_r / j_i = V_b + V_i + T_e / e + q_0 / j_i. \quad (8)$$

The term  $q_r/j_i$  is expressed in Volts, as all the others terms in Eq. (8). For very negative  $V_b$ ,  $j_i$  reaches saturation and Eq. (8) can be used to determine  $q_0$ . This is illustrated by the plots (Fig. 15) of  $j$  and  $q_r/j$  on  $V_b$  determined for values of 100 W and 10 mTorr of the discharge power and argon gas pressure, respectively. The plots of linear dependence of  $q_r/j$  on  $V_b$  for different power values (not shown here) showed the same slope value of 1. The experimentally determined values of  $q_r/j$  at  $V_b$  close to the  $V_f$  were overestimated due to the contribution of the electrons to the probe current (the approximation  $j_i \approx j$  does not hold at  $V_b$  close to  $V_f$ ). Extrapolation of the dependence of  $q_r/j$  on  $V_b$  towards  $V_f$  is used to determine  $q_0$ . The thermal probe was used as a planar Langmuir probe to determine  $j_{i0}$ ,  $V_f$  and  $T_e$ . Estimation of  $q_0$  based on the method described above showed that  $q_0$  accounts for about 30% of the total energy transferred by magnetron plasma to the substrate surface. Figure 14 shows the dependence of  $q_0$  and  $q_0 + q_{ch}(V_f)$  on the r.f. discharge power at a discharge gas pressure of 1.3 Pa. The experimental data showed a very good linear fit of  $q_0 + q_{ch}$  dependence on the discharge power. This dependence is easy to be explained if one considers that a small

fraction of the power injected to the discharge by the r.f. power supply is lost by the interaction of the discharge plasma with the film surface. Injecting more power into the discharge would increase proportionally the energy density of the discharge plasma and, thus, the energy transferred by plasma to the deposition substrate. The dependence of  $q_0$  on the discharge power is also linear.

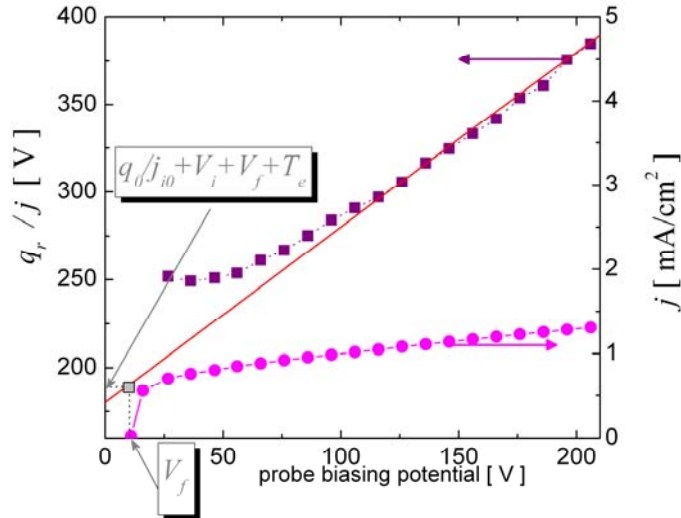


**Fig. 15** Experimentally determined dependence of  $qr/j$  on  $V_b$  for the thermal probe biased at negative potential values. A plot of total current density,  $j = j_i + j_e$ , dependence on  $V_b$  is given as well (solid circles). In these plots, as well as in Eq. (12),  $V_b$  was taken in absolute value. The probe was biased negatively to reject plasma electrons and attract plasma positive ions.

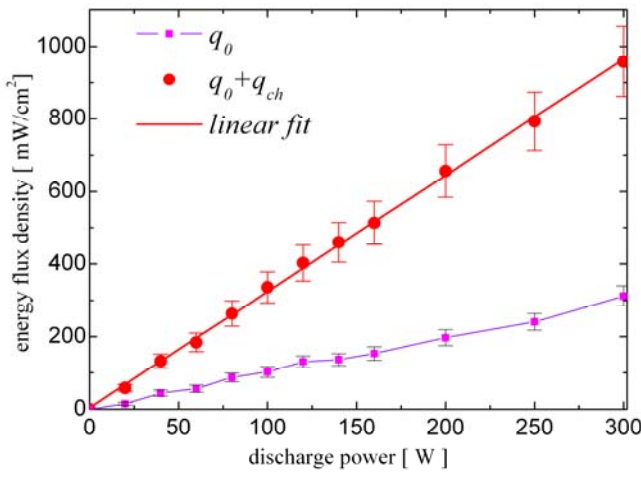


**Fig. 16.** Dependence on the discharge power of the total energy flux density ( $q_{ch} + q_0$ ) for the r.f. magnetron sputtering deposition in argon at 1.3 Pa. The values of  $q_0$  determined by the method described in Fig. 2, are also plotted.

Deposition of TiO<sub>2</sub> thin films on polycarbonate and Plexiglas substrates resulted in buckling of polymer surfaces at nanoscale. The plasma-induced changes in the film surface topography were investigated by AFM. Surfaces of TiO<sub>2</sub> thin films, which were deposited on polymer substrates for different values of the discharge power and deposition time, were scanned by AFM in tapping mode. Figure 17 shows topography images (scanned area of 10 μm × 10 μm) of the surfaces of Plexiglas substrate before deposition (0 minutes), and of TiO<sub>2</sub> thin films deposited during 30 minutes and 60 minutes, respectively, at a discharge power of 40 W and a gas pressure of 10 mTorr. These images show a temporal evolution of surface topography of Plexiglas substrate in its interaction with the deposition plasma. At short deposition time, a granular structure with small grains occurs on the polymer surface. The grains grow in size by the increase of the deposition time. These changes in the topography of TiO<sub>2</sub> film surface are not related to the structure of the deposited film. A deposition rate of about 1nm/minute was measured for films deposited on silicon wafers at a discharge power value of 200W [36, 7]. The thickness of the films analyzed here was estimated to be below 15 nm. The very small values of the thickness of the deposited films was confirmed also by optical transmission spectroscopy measurements, which showed almost no UV light adsorption for the films deposited at low power and relatively short deposition time. Therefore the large topography features as those showed by Fig. 17 can be attributed solely to the effect of polymer surface buckling in the deposition plasma. This assertion is supported by the fact that the TiO<sub>2</sub> thin films deposited in the same conditions on silicon wafers showed much smoother surfaces [7].

The effect of buckling of surface of polymer substrate in plasma was quantified by evaluation of the surface roughness. The root mean square roughness of the TiO<sub>2</sub> thin films deposited on polycarbonate and Plexiglas substrates was determined by processing the AFM images of surface topography of the deposited films. It appeared that the film surface roughness increased by the increase of either deposition time or discharge power in an identical manner. This is an indication that the polymer surface buckling effect is determined by the total energy transported by plasma towards the polymer surface and that the effect is not driven by the rise in  $T_s$ . Relatively the same buckling effect was achieved by depositions at either low discharge power and long deposition time or high discharge power and short deposition time. This observation rules out the possibility that the buckling effect could be caused by the mechanical stress raised by the difference in the thermal expansions of the film and substrate, respectively.

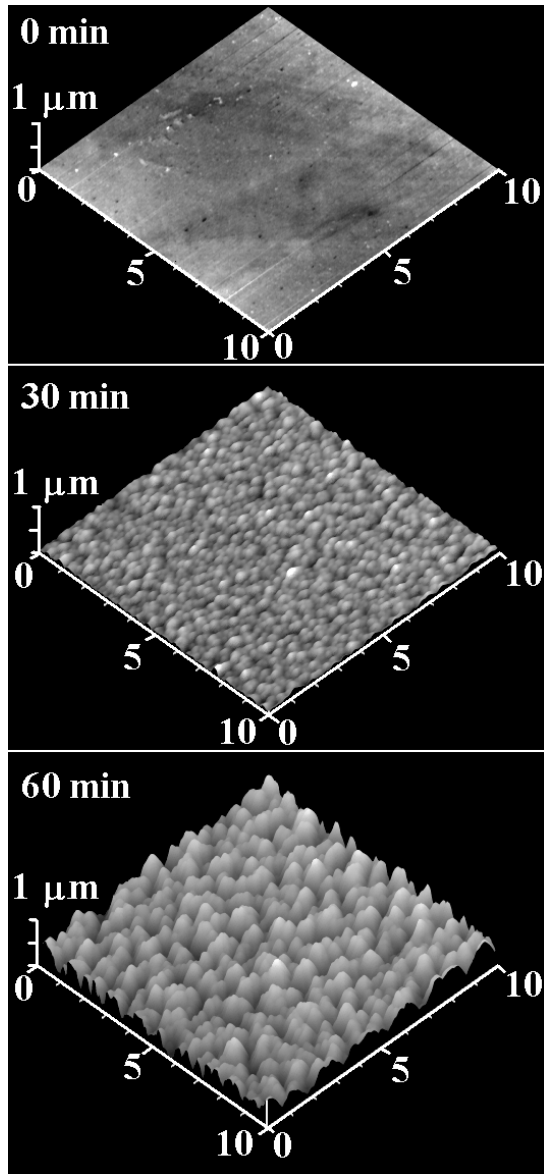


**Fig. 17.** Topography images of the surfaces of the Plexiglas substrate (0 min.) and  $\text{TiO}_2$  films deposited on Plexiglas in 30 minutes (30 min.) and 60 minutes (60 min.), respectively. Depositions were made at discharge power of 40 W and argon pressure of 10 Torr. The scanned surface area is  $10\mu\text{m} \times 10\mu\text{m}$ .

Should the surface buckling be caused by the difference in the thermal expansions of the film and substrate, the effect at low discharge power values (when  $T_s$  is low) would not be observed. The deposition speed in this particular deposition system was low, especially at low discharge power, so that the deposited  $\text{TiO}_2$  films were too thin to generate the mechanical stress required for the observed surface buckling effect. The dependence of the roughness on the product of discharge power and deposition time found for the two substrates is presented in Fig. 18.

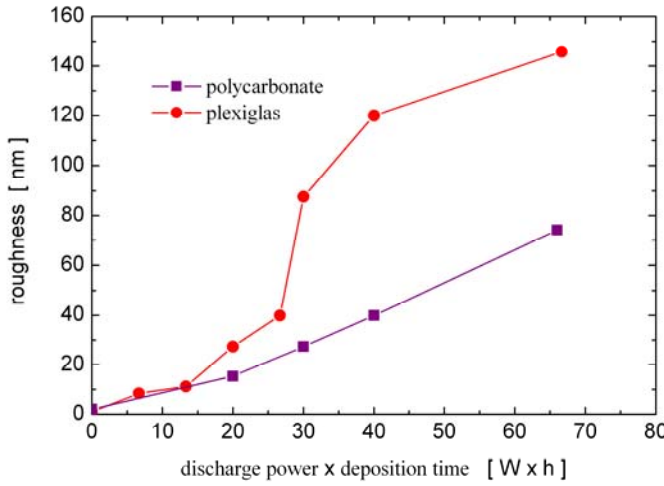


**Fig. 18 Increase of the film surface root mean square roughness due to the substrate surface buckling in magnetron sputtering deposition of TiO<sub>2</sub> thin films on polycarbonate and Plexiglas substrates.**

The surface buckling effect is stronger on the polymer with the smaller melting temperature and it increased monotonically by the increase of the product of the deposition power and deposition time. No saturation effect was observed into the used range of the discharge power and deposition time.

According to the results of substrate temperature computation, the buckling of the polymer substrate cannot be regarded as a result of melting of a thin layer at the top of the polymer substrate, but more as a complex result of energy transfer from the deposition plasma towards the polymer surface. This agrees with the experimental results reported by other authors [58, 59], which showed that the effect of polymer surface buckling in interaction with plasma is related to the total energy transported by plasma towards the polymer surface. It appeared that noble gas plasma, especially helium plasma [59], is very efficient in inducing polymer surface buckling. This is because the bombardment of polymer surface with ions of an inert gas extracts hydrogen atoms from polymer structure and modifies the chemical and physical properties of a thin layer on the top of the polymer surface.

In summary, amorphous TiO<sub>2</sub> thin films with good photocatalytic activity can be obtained by either PECVD or RFMSD. The sputtering deposition produced films with high adhesion and hardness, but with relatively low photocatalytic activity. The low photocatalytic activity of these films corresponds to their heterogeneous crystalline and amorphous mesostructure. An AFM study of surface hydrophilicity of UV-irradiated TiO<sub>2</sub> thin films

obtained by RFMSD and PECVD revealed that PECVD films have higher photocatalytic activity and more homogeneous and smooth surfaces as compared to RFMSD films. However, a good choice of the deposition parameters in RFMSDs yielded amorphous TiO<sub>2</sub> thin films with homogeneous surfaces and high photocatalytic activity. Single Langmuir probe and optical emission spectroscopy diagnosis of RFMSD plasma proved that the pressure value of Ar-O<sub>2</sub> gas has a big impact on plasma parameters and plasma particle bombardment of the deposited films. The low energy of plasma particles (ions and electrons) at relatively high value of the gas pressure (10 mTorr) favored deposition of amorphous TiO<sub>2</sub> thin films with a short range order of anatase type, good UV-light-induced hydrophilicity, microscopically smooth and homogeneous surfaces. At lower gas pressure values, the energy of plasma particles increases, which favor depositions of TiO<sub>2</sub> films with mixed crystalline and amorphous structure and relatively rough and inhomogeneous surfaces. The mixed crystalline structure of the films deposited at low gas pressure (less than 10 mTorr) has been observed as film surface nanoscopic regions of high hydrophilicity mixed with regions of low hydrophilicity on UV irradiated TiO<sub>2</sub> film surfaces. These regions are discriminated by friction force microscopy measurements, the friction force values being larger on hydrophilic regions than the values measured on less hydrophilic regions of the UV irradiated TiO<sub>2</sub> thin films. However, the photocatalytic activity of amorphous TiO<sub>2</sub> ultra thin films (with thickness less than 12 nm) obtained by RFMSDs depended on film thickness and substrate. The weaker effect of UV light irradiation observed for the ultra-thin films (in comparison with thicker films) was explained based on results of measurements of surface topography, UV-light absorption and photocurrent decay in vacuum. Comparing to thicker films, the ultra-thin films have a smoother surface, which diminish their real surface area and density of defects, absorb partially the incident UV light radiation, and exhibit a longer decay time of the photocurrent in vacuum, which proves a spatial charge separation. In case of RFMSDs on polymer substrates, the energy flux transported by plasma particles toward the film surface affects drastically not only the films properties, but also the morphology at nanoscale of the polymer surface. This was the case of RFMSDs of TiO<sub>2</sub> on polymethyl methacrylate and polycarbonate substrates, which showed buckling of their surfaces. The effect was evaluated by analysis of AFM topography images of the deposited TiO<sub>2</sub> films. The amount of energy received by the substrate surface during the film deposition was determined by a thermal probe. Then, the results of thermal probe measurements were used to compute surface temperature of the polymer substrate. The computation indicated substrate surface temperature values under the polymer melting temperature. Therefore, the buckling of

polymer substrate surface in the deposition plasma was not regarded as a temperature driven surface instability, but as an effect of plasma ion bombardment.

This summary does not give a complete description of the results obtained by the author (L. Sirghi) in this filed. Thus, results concerning the effect of the biased grid on plasma parameters and voltage across the wall sheath in r.f. magnetron discharge used for deposition of TiO<sub>2</sub> thin films [60] were not described here. Also, the results of a study of photocatalytic chemisorption of water on titanium dioxide (TiO<sub>2</sub>) thin films obtained by RFMSD based on the photocurrent decay experiments on the films exposed to water vapor [61] were not described.

### **II.1.2 Plasma enhanced chemical vapor deposition of super hydrophobic fluorocarbon thin films with application in nanoindentation lithography**

Fluorocarbon (CF<sub>x</sub>) thin films with good hydrophobic and hardness properties are usually synthesised by PECVD that employs discharge plasmas to dissociate precursor gases [62, 63]. In order to obtain a good compromise between the good hydrophobic property of pure fluorocarbon films and the good hardness and wear resistance of pure hydrocarbon films (which are not hydrophobic) fluorinated carbon films are synthesized by PECVD in mixed hydrocarbon and fluorocarbon gases [62]. For these films, it was found that their hydrophobicity improves by the increase of the fluor content, while the hardness and wearing resistance decrease [63]. An alternative method to synthesise fluorocarbon film consists of sputtering deposition in a r.f. magnetron discharge using polytetrafluoroethylene (PTFE) target [64].

Sirghi et al [40] (see the selected paper P5) has studied fluorinated carbon films obtained by PECVD in pure fluorocarbon gas at low *r.f.* power and *d.c.* biasing potential, films that show especially good hydrophobicity and plasticity compliance. It was found by different authors [65, 66] that the CF<sub>x</sub> films obtained by PECVD in pure fluorocarbon gases at low discharge power have a high density of C-F bonds, which renders a good hydrophobic property to these films. Sirghi et al have shown that the reduction of the discharge power in the PECVD of CF<sub>x</sub> films results in decrease of the film hardness and stiffness and increase in plastic compliance. Moreover, it has been shown that the CF<sub>x</sub> films deposited at low discharge power, while having good hydrophobic property, are suitable to AFM indentation-based nanolithography because of their increased plasticity index.

The fluorocarbon films were deposited on silicon substrate in a plasma reactor that used an asymmetrical r.f. (13.56 MHz) capacitive discharge at low discharge power (5-30 W) in pure  $\text{C}_4\text{F}_8$  gas flow at the pressure of 6.5 Pa (Fig. 19). The deposition substrate was mounted on the active discharge electrode, which was self biased at a negative potential ranged, depending on the discharge power, between -10 V and -80V. The film thickness was measured by a stylus profilometer. The static values of water contact angle were measured with a contact angle goniometer on sessile drops of water on the deposited films.

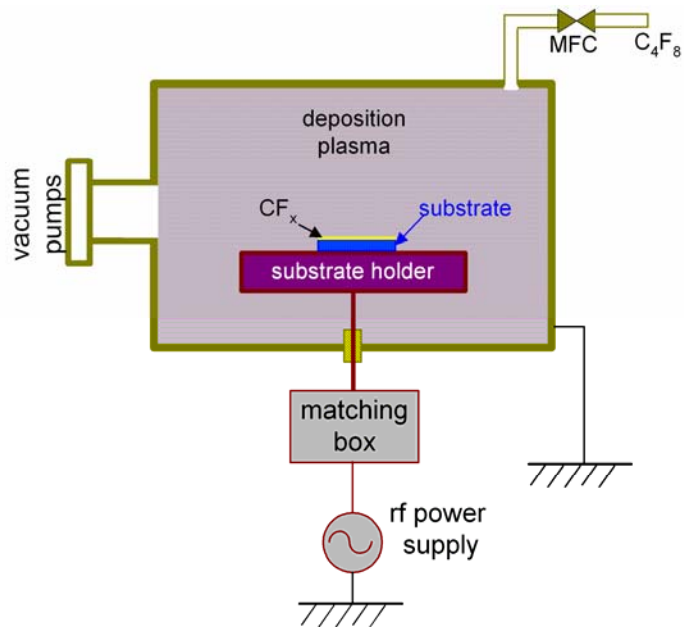


**Fig. 19 Sketch of the PECVD system used for fabrication of  $\text{CF}_x$  thin films**

The surface topography of the films was characterised by taping mode AFM measurements performed with a commercial AFM apparatus with close-loop scanner system. The indentation experiments were performed by the same AFM apparatus and probe that were used for tapping mode AFM characterization of the film surface. Indentation experiments required the use of AFM probes with stiff cantilevers (15-20 N/m) and very sharp tips (curvature radius under 10 nm). The imprints resulted from the indentation experiments were immediately imaged by tapping-mode AFM. Results of these investigations in terms of deposition rate, water contact angle, surface roughness, elasticity modulus, hardness, and plasticity index for the films deposited at different values of r.f. discharge power are given in Table 4.

**Table 4. Deposition parameters and surface properties of  $\text{CF}_x$  films.**  $P$  is the power of r.f. discharge in  $\text{C}_4\text{F}_8$  gas,  $V_{sb}$ , the self-biasing potential of the deposition substrate,  $t$ , the deposition rate,  $\theta_w$ , the water contact angle of the film surface,  $E$ , the Young modulus of elasticity,  $H_n$ , the film hardness at nanoscale, and  $\psi$ , the plasticity index.

$P$ (W)	$V_{sb}$ (V)	$t$ (nm/min)	$\theta_w$ (deg.)	roughness (nm)	$E$ (GPa)	$H_n$ (GPa)	$\psi$
5	-10	7	$106 \pm 1$	$0.36 \pm 0.05$	$1.75 \pm 0.3$	$0.31 \pm 0.03$	$0.84 \pm 0.05$
10	-20	20	$106 \pm 1$	$0.52 \pm 0.07$	$2.1 \pm 0.6$	$0.52 \pm 0.09$	$0.77 \pm 0.04$
20	-60	36	$105 \pm 1$	$0.58 \pm 0.07$	$2.4 \pm 0.6$	$0.88 \pm 0.19$	$0.6 \pm 0.04$
30	-80	45	$106 \pm 1$	$0.59 \pm 0.08$	$3.2 \pm 0.7$	$1.57 \pm 0.46$	$0.55 \pm 0.5$

The values of elasticity modulus and hardness in Table 4 were determined by analysis of force-displacement data acquired on AFM indentation experiments performed on thick  $\text{CF}_x$  films (thickness around 200 nm) in order to avoid the effect of the stiff substrate [67]. The force-displacement data were acquired for indentations performed on array of 49 points on surfaces of  $\text{CF}_x$  films. Figure 20 illustrates a comparison between force-displacement curves obtained in indentation experiments on the film substrate and on  $\text{CF}_x$  films deposited at different r.f. discharge power values. The position of the sample surface before indentation has been chosen as the origin of the indenter (tip of the AFM probe) displacement. The force-displacement curve acquired on the substrate was used for calibration of the cantilever deflection. The force-displacement curves presented in Fig. 20 show that, at the same maximum indentation force, the films deposited at lower r.f. discharge power suffer larger plastic and elastic deformations (larger values of indenter displacement inside the bulk of the films). The plastic deformation occurs during the loading process (portion OA of the force displacement curve of the  $\text{CF}_x$  film deposited at 10 W in Fig. 20) when the AFM tip is displaced until  $h_{max}$ , the loading force increasing until the maximum value,  $F_{max}$ . The unloading process (portion AB of the force displacement curve of the  $\text{CF}_x$  film deposited at 10 W in Fig. 20) is an elastic relaxation of the film surface when the loading force decrease continuously. Because of the adhesive force between the AFM tip and the  $\text{CF}_x$  film surface, the force acquired during the unloading process reaches a negative minimum and cancels out at the moment of detachment [68], which indicates the imprint depth,  $h_{imp}$  (shown by arrows in Fig. 20).

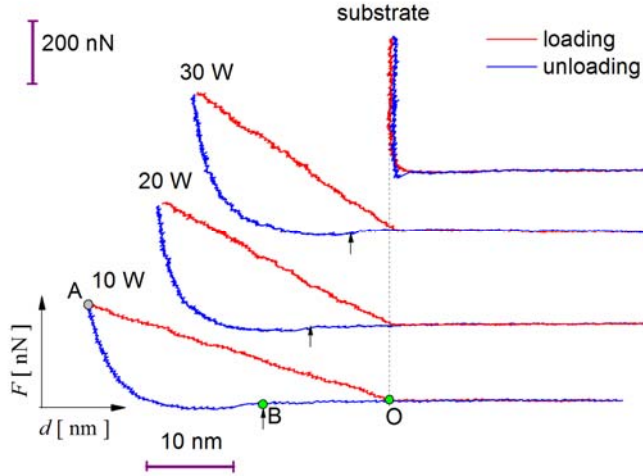


**Fig. 20** Typical force-displacement curves corresponding to indentations of the  $\text{CF}_x$  films deposited at r.f. discharge power values of 10W, 20W and 30W, respectively. The force-displacement curve corresponding to indentation of the substrate (silicon) is also shown. The origin, O, of the AFM tip displacement is corresponding to the non deformed film surface. The arrows indicate the position of the film surface after the indentations.

The mechanical work performed during the loading,  $W_l$ , is partially recovered by the mechanical work of the elastic force of the sample surface during unloading,  $W_u$  ( $W_u < W_l$ ). The area encompassed by the loading and unloading force curves,  $W_l - W_u$ , represents the energy loss in plastic deformation of the sample surface. Therefore, the plasticity index of the sample material is defined as [69]

$$\psi = \frac{W_l - W_u}{W_l}, \quad (9)$$

and represents the fraction of energy used for the plastic deformation from the total mechanical work performed during loading. The value of  $\psi$  ranges between 0 (fully elastic deformation) and 1 (fully plastic deformation). Films with low hardness, high elasticity modulus and high plasticity index are suitable to the indentation lithography because indentation of these films results in large plastic deformations with relatively small elastic deformations. The plasticity index was determined according the Eq.(9) by processing force displacement curves acquired in indentations of the  $\text{CF}_x$  films deposited at different discharge power values. The obtained values of  $\psi$ , which are given in Table 4, shows that the films deposited at discharge power lower than 10 W are suitable to indentation lithography, indentation of these films being mainly plastic ( $\psi > 0.75$ ).

The values of elastic modulus of film surfaces can be determined by Oliver and Pharr model of indentation [70]. The model foresees for the unloading part of an indentation experiment performed with an axis symmetrical indenter a power law dependence of the loading force on the indenter displacement. However, the force-displacement curves acquired in indentations of  $\text{CF}_x$  films did not fit well a power law dependence. This may have happened because: 1) the peculiar geometry of the contact as result of particular geometry of the AFM tip and imprint, and 2) action of the indenter-sample adhesive force. Therefore, the Doerner and Nix [71] approximation of the flat indenter at the beginning of the unloading process has been used to determine the film surface elasticity modulus. According to the Sneddon equation [72], the contact stiffness at the beginning of the unloading process is

$$S_{\max} = \left( \frac{dF}{dh} \right)_{\max} = E^* \cdot 2r_{c,\max}. \quad (10)$$

where  $E^*$  is the reduced elastic modulus of the indenter-sample system, which is

$$\frac{1}{E^*} = \frac{1 - \nu_i^2}{E_i} + \frac{1 - \nu_s^2}{E_s}. \quad (11)$$

The parameters  $E_i$  and  $\nu_i$  are the Young's modulus and Poisson ratio of the indenter, while  $E_s$  and  $\nu_s$  are the same parameters for the sample. Because the  $\text{CF}_x$  films are much softer than the silicon tips of the AFM probes ( $E_s \ll E_i$ ) and

$$E^* \cong \frac{E_s}{1 - \nu_s^2}. \quad (12)$$

The parameter  $r_{c,\max}$  in Eq.(14) is the indenter-sample contact radius at the beginning of the unloading process. Considering that the indentation imprint retains the information of the contact area at the maximum loading force, the contact radius at the maximum loading force can be evaluated as

$$r_{c,\max} \cong \frac{d_{imp}}{2}. \quad (13)$$

Then, according Eqs (10), (12), and (13), the  $\text{CF}_x$  film elastic modulus can be approximated by

$$E_s = (1 - \nu_s^2) \cdot \frac{S_{\max}}{d_{imp}}. \quad (14)$$

The information on the imprint diameter is also used to determine the contact area at the maximum loading force and the nanoscale hardness of the  $\text{CF}_x$  films as:

$$H_n = \frac{F_{\max}}{\pi \cdot r_{c,\max}^2} = \frac{4 \cdot F_{\max}}{\pi \cdot d_{imp}^2} . \quad (15)$$

The acquired force-displacement curves were processed to determine  $S_{\max}$  and  $F_{\max}$ , while the AFM images of the resulted imprints were processed to determine  $d_{imp}$ . The obtained information was used to determine  $E$  and  $H_n$  according the Eqs. (14) and (15), respectively.

Figure 21 presents plots with the dependence of  $H_n$  and  $E$  on the power of the r.f. discharge used for PECVD deposition of the  $\text{CF}_x$  films. Both parameters decrease with the decrease of the discharge power. The hardness of these films is low (typically under 1GPa) due to high density of CF groups in the film structure [16]. It has been shown by different research groups that hardness of  $\text{CF}_x$  films decreases with the increase of fluorine content of the films. Thus, Bottani et al showed for the  $\text{CF}_x$  films obtained by PECVD from  $\text{C}_2\text{H}_2$  and  $\text{CF}_4$  gas mixture that film hardness decreases from 13.5 GPa to 2.5 GPa by the increase of the  $\text{CF}_4$  content of the source gas from 0 % to 60 %, respectively. For the present deposited  $\text{CF}_x$  films, decrease of plasma discharge power from 30 W to 5W reduced the ion bombardment of the film surface and favoured formation of polymeric  $\text{CF}_x$  structures with the effect of decrease of hardness from 1.57 GPa to 0.31 GPa.

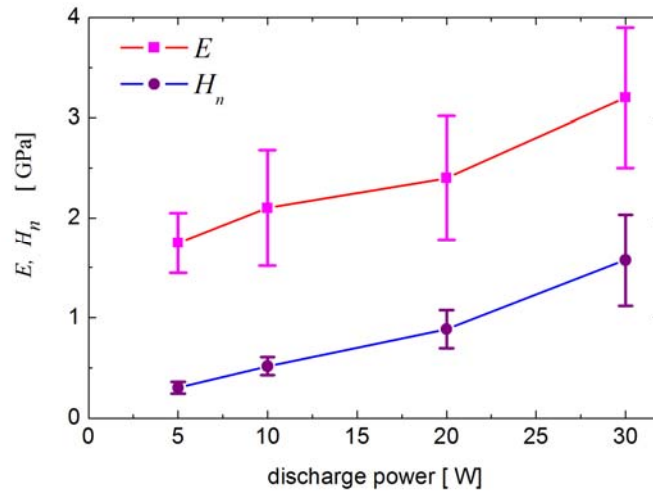


**Fig. 21** The dependence of  $\text{CF}_x$  film hardness ( $H_n$ ) and elasticity modulus ( $E$ ) on the power of the r. f. discharge used in film deposition.

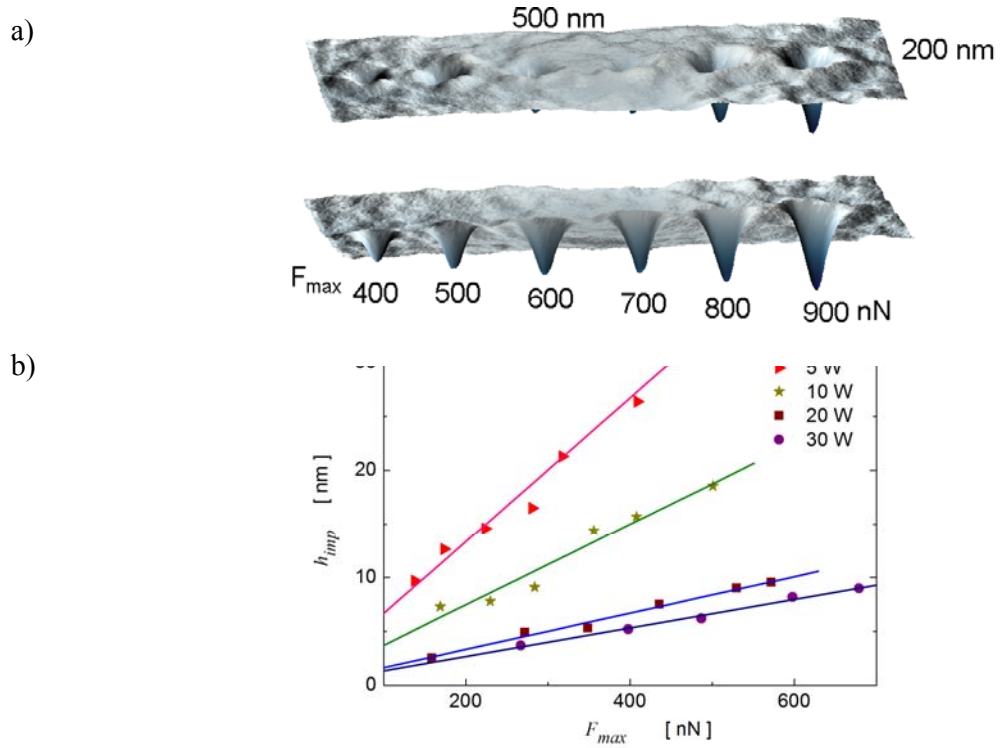


Fig. 22 a) Image (500 nm × 200 nm) of a set of six imprints obtained by indentation with different  $F_{max}$  of the CF<sub>x</sub> film deposited at 10 W r.f. discharge power. b) The dependence of the imprint depth ( $h_{imp}$ ) on the maximum value of the loading force ( $F_{max}$ ) for the thin CF<sub>x</sub> films (thickness of 40 nm) deposited at the r.f. discharge power values of 5, 10, 20, and 30 W, respectively.

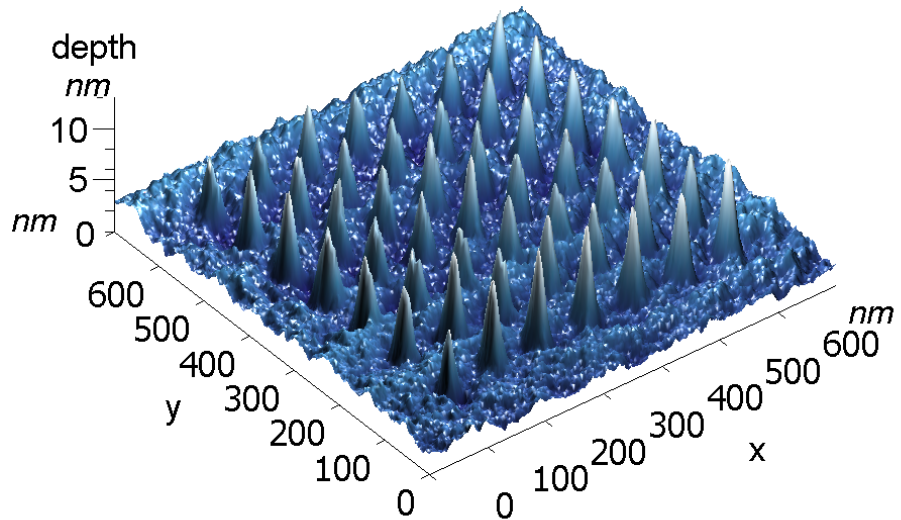


Fig. 23 Inverted 3D image of an array of 7 × 7 pits made by indentation of the CF<sub>x</sub> film deposited at 10 W r.f. power

Indentation of  $\text{CF}_x$  films obtained by PECVD at low power is suitable for nanolithography. Sets of imprints with increasing loading force on thin  $\text{CF}_x$  films (thickness of 40 nm) were performed by indentation with increasing indentation force in order to determine the dependence of the imprint depth on the indentation force. Indentations performed on these films left imprints with slightly larger depth, when compared to the imprints depth performed on thicker films (thickness of 200 nm). This is explained by the fact that the hard substrate limited the elastic deformations of the film, thus enhancing the plastic deformations. Figure 22 a) shows a 3D image of six imprints left by indentation with increasing maximum force,  $F_{max}$ , on the  $\text{CF}_x$  film deposited at 10 W r.f. discharge power. The height profiles of the resulted imprints were used to determine  $h_{imp}$  and  $d_{imp}$  for different values of  $F_{max}$ . Figure 22 b) shows the dependence of  $h_{imp}$  on  $F_{max}$  for thin  $\text{CF}_x$  films deposited at different discharge power values. While the imprint depth remained smaller than the film thickness, it increased linearly by the increase of  $F_{max}$ . Therefore, linear fits of the experimental data are also shown on Fig. 20 b). For these measurements, the values of  $d_{imp}$  were proportional to square root of  $F_{max}$ , which is an indication of constant hardness. Figure 23 shows an array of imprints demonstrating the  $\text{CF}_x$  films deposited at low r.f. power offer suitable surfaces for indentation nanolithography.

In summary, fluorocarbon thin films were obtained by PECVD in an asymmetrical r.f. capacitive discharge at low discharge power (5-30 W) in pure  $\text{C}_4\text{F}_8$  gas flow at low pressure and the film surface properties (hardness, elasticity, plasticity, and hydrophobicity) were studied in connection with the discharge power as a deposition controlling parameter. The motivation of this study is related to fabrication of a highly hydrophobic surface suitable to indentation lithography. The film elasticity modulus and hardness were determined by the AFM indentation experiments performed with commercially available AFM probes with relatively stiff cantilevers and sharpened tips. Tapping-mode AFM images of the imprints resulted from the indentation experiments were used to determine the indenter-film contact radius at the beginning of unloading part of the indentation. Then, the film surface elasticity and hardness were determined by measurements of the indenter-sample contact stiffness at the beginning of the unloading process, maximum indentation force, and indenter-sample contact radius at maximum loading force. These measurements showed that the decrease of the discharge power used in PECVD of the  $\text{CF}_x$  films decrease the film hardness and stiffness, while increased the film plasticity index. For thin  $\text{CF}_x$  films (thickness of 40 nm) the depth of the indentation imprints increases linearly by the increase of the maximum

loading force. The AFM indentation technique was used to build arrays of pits in CF<sub>x</sub> thin films obtained by PECVD on silicon substrate, which demonstrate that thin CF<sub>x</sub> films deposited at low discharge power are suitable to nanolithography because of their good plasticity.

### **II.1.3 High power impulse magnetron sputtering deposition of optically transparent and electrically conductive ZnO:Al thin films**

Growth of polycrystalline thin films of ZnO have been achieved by molecular-beam epitaxy [73], magnetron sputtering [74], pulsed laser [75], and chemical vapor [76] depositions. However, because of its low cost, simplicity and scalability to large areas, the magnetron sputtering is one of the most popular growth techniques of ZnO thin films [77]. It allows for deposition on low-temperature substrates of high-density and adherent films with good optical and electronic properties. Commonly, this growth technique uses a continuous or pulsed r.f. or d.c. electric discharges in low pressure Ar, or Ar/O<sub>2</sub> mixture gases with ZnO or Zn targets. One of the most attractive magnetron sputtering techniques used to produce high-density metal oxide films is high-power impulse magnetron sputtering (HiPIMS) [78] of pure metal targets in Ar/O<sub>2</sub> mixture gaz. This technique uses very short (1-50 µs) high-voltage (1000-2000 V) pulses applied at low repetition frequency (0.1 - 10 kHz) to the magnetron cathode to produce high power (tens of kW) impulse discharges that sputter a large amount of metal atoms and ions in the reactive gas. An improvement of HiPIMS discharge consisting in an increase of the impulse power and a decrease of the rising time of the impulse current intensity can be achieved by using a preionization discharge current in continuous mode [79]. It has been shown that the HiPIMS produces a large amount of ionized metal atoms with beneficial effects on the deposited metal oxide films [80]. HiPIMS technique has been used to grow ZnO thin films, which showed smoother surface as compared with surfaces of ZnO thin films deposited by continuous d.c. magnetron sputtering [81]. HiPIMS of a metallic Zn:Al alloy target (1.5 wt% aluminum) in Ar/O<sub>2</sub> plasma has been used by Ruske et al [82] for deposition of ZnO:Al thin films with electric resistivity as low as  $4 \times 10^{-4} \Omega \times \text{cm}$ .

Recently, Sirghi, Tiron and Popa [41, 42] reported a new method of control of Al doping of ZnO thin films deposited by HiPIMS of a pure Zn target in low-pressure Ar/O<sub>2</sub> gas. The method uses sputtering of an electrically negative biased aluminum electrode placed in the proximity of the negative glow of the magnetron discharge. This controlled doping

method has been confirmed by measurements of resonant laser absorption measurements of Al atom concentration in vapor phase during the depositions and the XPS (X-ray Photoelectron Emission Spectroscopy) measurements of Al concentration in the deposited ZnO:Al films. The new deposition and doping method has been used for fabrication of optically transparent ZnO:Al thin films with good electrical conductivity. The experimental setup used for HiPIMS deposition and control of Al doping of ZnO:Al thin films is presented schematically in Fig. 24. The deposition chamber made from stainless steel is equipped with a water-cooled magnetron cathode with a target of high-purity Zn (a disk with diameter 56 mm and thickness of 4 mm). The Al electrode, which is shaped as a planar spiral from a high-purity Al wire with diameter of 1.5 mm and length of 500 mm, is placed at 30 mm from the cathode and 20 mm from the deposition substrate. The deposition chamber is vacuumed down to  $10^{-5}$  Pa by a vacuum system formed by a turbomolecular pump and a preliminary dry vacuum pump. The gas pressure during depositions is maintained at 6.6 mPa, while the flows of Ar and O<sub>2</sub> are maintained at 49.5 sccm and 0.5 sccm, respectively, by two mass flow controllers. The HiPIMS is obtained by applying short (6  $\mu$ s) high-voltage (900 V in amplitude) pulses on the cathode by a special electrical current source [79] that assures between pulses a constant preionization discharge current of 8 mA. Typical variation of discharge voltage and current intensity during one discharge pulse is shown in Fig. 25.

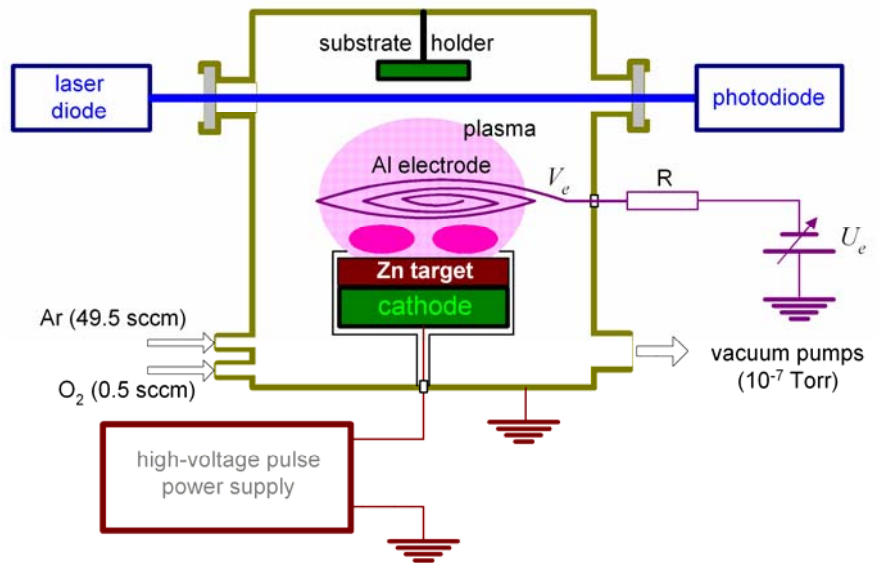


**Fig. 24** Sketch of the experimental setup used for deposition of ZnO:Al thin film with auxiliary discharge on an aluminum electrode for control of aluminum doping.

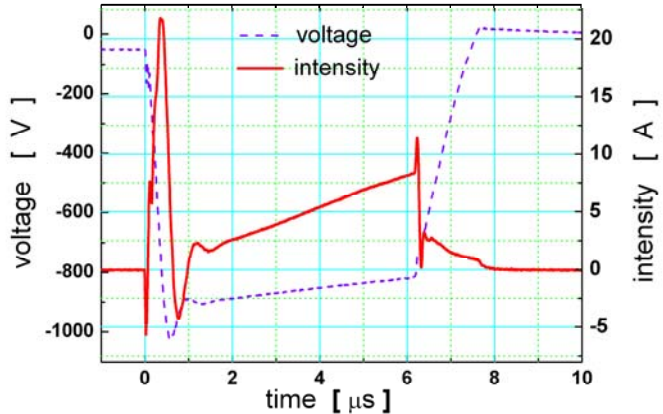


**Fig. 25** Typical variation of discharge voltage and current intensity during one discharge pulse.

A peak value of 20 A is noticed for the discharge current intensity during the application of the high-voltage pulse. The repetition frequency of high-voltage pulses is 1 kHz. The preionization discharge current assures impulses in discharge current intensity as large as 10 A. The deposition chamber is equipped with two glass windows used by the resonant laser absorption measurement system. This system uses a laser diode (Toptica DL 100) to emit radiation with the wavelength of 394.401 nm to excite Al atoms from the fundamental state  $3s^23p$  in the excitation state  $3s^24s$  and a photodetector to acquire the transmitted laser radiation intensity,  $I_t$ . The absorption coefficient,  $A = (I_t - I_0)/I_0$ , where  $I_0$  is the laser radiation intensity, is used to compute the concentration of Al atoms in vapor phase during ZnO:Al thin film deposition [83]. This measured value of Al atom concentration corresponds to integral absorption of laser radiation along a chamber diameter placed at a distance of few mm above the deposition substrate. Figure 26 represents the time variation of the electrode current intensity during HiPIMS discharge at the value of 550 V of the electrode biasing potential,  $V_e$ . This variation shows two working regimes: 1) the anodic regime, during the high voltage pulse and about 80  $\mu$ s after it, when the electrode works as a second anode for the HiPIMS discharge and collects an electronic current (positive values of  $I_e$  on the plot in Fig. 26); 2) the cathode regime, during HiPIMS plasma diffusion, when the electrode is electrically negative with respect to the HiPIMS diffusion plasma and works as a cathode that collects positive ions from plasma (negative values of  $I_e$  on the plot in Fig. 26). The anodic regime for one HiPIMS pulse represented in Fig. 26 is highlighted by a grey rectangle. The average value of the electrode discharge current,  $\langle I_e \rangle$ , is negative, which shows prevalence of the cathode regime and positive ion flux.

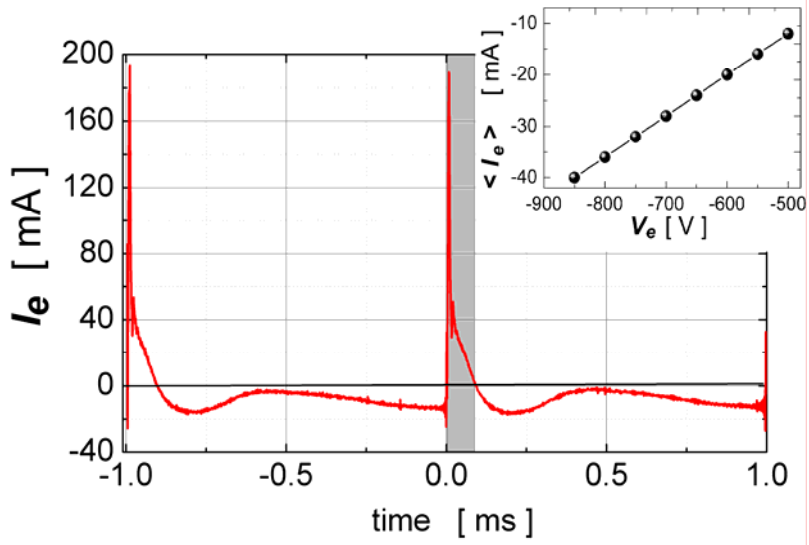


**Fig. 26** Time variation of electrode current intensity,  $I_e$ . The inset presents the dependence of the average value of  $I_e$  on the electrode biasing potential,  $V_e$ . The grey rectangle highlights the anode working regime of the electrode.

A plot, which shows a linear dependence of  $\langle I_e \rangle$  on  $V_e$ , is represented by the inset in Fig. 26. This plot shows that positive ion flux of aluminum electrode and sputtering of aluminum atoms can be enhanced by increasing of the negative values of  $V_e$ .

Results of resonant laser adsorption measurements of aluminum atoms concentration,  $n_{Al}$ , in the vapor phase, which are presented in Fig. 27, show that the increase of the negative value of  $V_e$  from -500 V to -850 V results in an increase of  $n_{Al}$  in vapor phase from  $2 \times 10^{13} \text{ m}^{-3}$  to  $2.5 \times 10^{15} \text{ m}^{-3}$ . This dependence is not linear because the sputtering depends not only on the ion flux intensity, but also on the energy of the positive ions, which increases with  $|V_e|$ . It should be mentioned that the electrical discharge on the Al electrode and the positive ion flux of the electrode are strongly dependent on the parameters of the principal HiPIMS discharge. In order to confirm that the variation of  $n_{Al}$  in the vapor phase determines variation of Al concentration in the deposited films, thin films of ZnO:Al has been deposited on quartz at values of  $V_e$  ranged between -500 V and -850 V. The deposited films had the thickness ranged between 700 nm and 1150 nm, the deposition rate increasing from 6 nm/min to about 10 nm/min with the increase of  $V_e$ . The atomic concentration of aluminum in the deposited films,  $c_{Al}$ , was determined from the O 1s, Zn 2p3, and Al 2p binding peaks in the XPS spectra. The results of these measurements are also shown in Fig. 27. The concentration of Al atoms in the deposited films showed also a drastic increase with the variation of  $V_e$  from 0.1 at. % in the film deposited at  $V_e = -500$  V to 23.1 at. % in the film deposited at  $V_e = -850$  V.

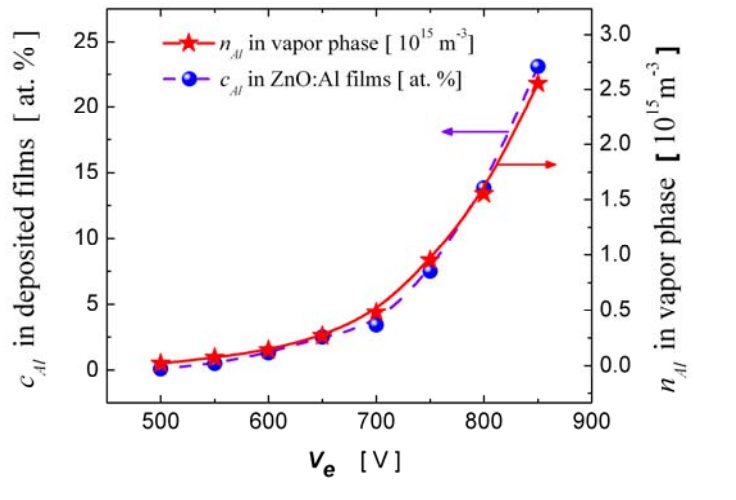


**Fig. 27 Dependence of Al concentration in vapor phase,  $n_{Al}$  ( $\text{m}^{-3}$ ), and in deposited films,  $c_{Al}$  (at. %), on the electrode biasing potential,  $V_e$ .**

As it is shown in Fig. 27, this increase of  $c_{Al}$  follows closely the increase of  $n_{Al}$  in the vapor phase. Therefore,  $V_e$  is a key parameter for the control of the Al doping process in ZnO:Al thin films obtained by the present deposition and doping method.

The optical properties of the deposited ZnO:Al films were investigated by UV-VIS transmission spectroscopy in the spectral range 200 – 1100 nm. Fig. 28 shows the optical transmittance spectra of ZnO thin films with different values of Al doping concentration. In the visible range of the spectra, the deposited ZnO:Al films have a high transmittance with the average value of approximately 85% and small interference oscillations. In the ultraviolet region, the transmission spectra of the deposited ZnO:Al films show strong absorption with the absorption edge in the wavelength range of 320–400 nm. According to the position of the absorption edge in the transmission spectra, the energy band gap of the investigated ZnO:Al films varied with the concentration of Al between 3.28 eV, registered for the film with 3.5 at. % concentration of Al atoms, to 3.56 eV, registered for the film with 23.1 % concentration of Al atoms. The ultraviolet-visible transmission spectra of pure (not shown) or weakly doped (concentration of 0.1 at. % of Al atoms) ZnO films show band gap energy around 3.4 eV. Therefore, at low doping concentration, the energy band gap decreases with the increase of Al atom concentration in the deposited ZnO:Al films, while at high doping concentration (higher than 3.5 at. %) the energy band gap increases with the increase of Al atom concentration.

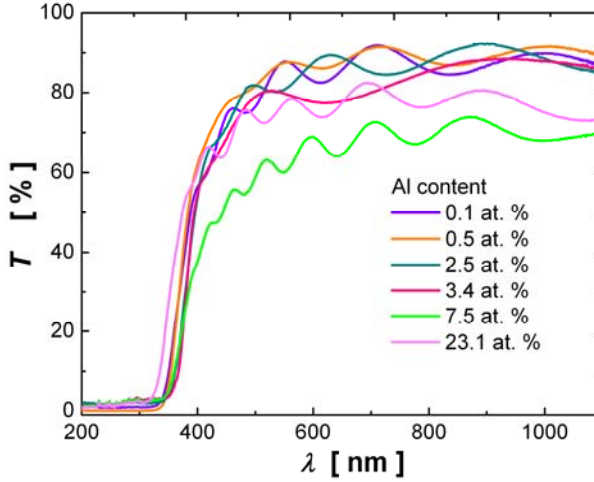


**Fig. 28** The ultraviolet-visible transmission spectra of ZnO:Al thin films deposited at different Al electrode biasing voltage

The photoluminescence (PL) of the deposited ZnO:Al films was studied in order to obtain information on the quality and purity of the deposited films. The PL measurements were performed at room temperature using a 340 nm UV xenon excitation lamp. The PL spectrum of ZnO:Al is normally composed of two parts: one is the excitonic emission with energy around the band gap of ZnO in the UV region [84], the other is the defect-related deep level emission in the visible range. The ultraviolet emission is due to the excitonic related recombination [85]. The exact mechanism for deep level emission is still disputed but extrinsic impurities and intrinsic defects, such as oxygen vacancies [86, 87], oxygen interstitial, and zinc vacancies [88, 89], were reported as the origin of this emission. The emission intensity is determined by the radiative and nonradiative transitions. Therefore, the luminescence efficiency is described by the following formula [90]:

$$\eta = I_R / (I_R + I_{NR}), \quad (16)$$

where  $\eta$  is luminescence efficiency,  $I_R$  and  $I_{NR}$  are radiative and nonradiative transition probabilities, respectively. In the case of ZnO, the nonradiative transition is induced by crystal imperfections, such as point defects, dislocations and grain boundaries. These defects produce various nonradiative centers and reduce the emission intensity from the ZnO. Therefore, the emission properties of ZnO films are strongly dependent on the growth condition. It has been reported that the PL emission characteristics of ZnO films are strongly dependent on both the crystallinity of the film and the film stoichiometry [91]. Figure 29 shows that relative PL emission intensity of the deposited ZnO:Al films increases with

increasing Al content in films. This indicates that PL radiative transition probability increases with the Al atom concentration in the film while the nonradiative transition probability remains constant due to good stoichiometry and crystallinity of the deposited films.

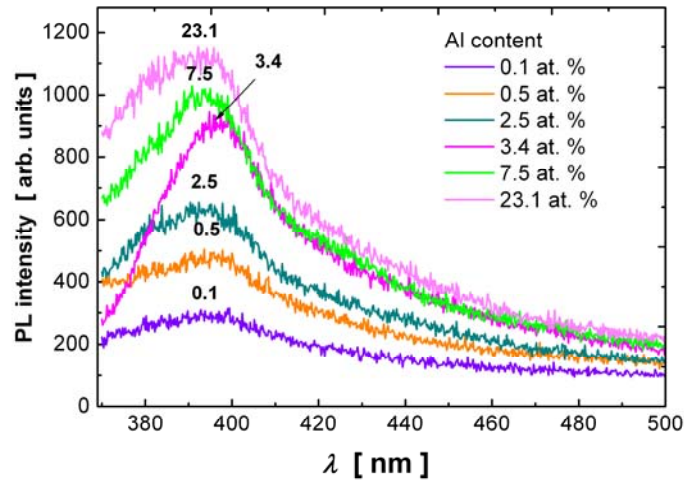


**Fig. 29** The PL spectra of ZnO:Al films with different Al doping concentration values.

The crystalline structure the deposited ZnO:Al thin films were characterized by X-ray diffraction (XRD) of Cu  $K\alpha$  radiation in the usual  $\theta$ - $2\theta$  geometry (Shimadsu). The grain size  $d_g$  was derived from the diffraction line width at half the maximum intensity,  $\beta$ , of the (002) line according to the Scherrer formula:

$$d_g = \frac{k \cdot \lambda}{\beta \cdot \cos \theta} , \quad (17)$$

where  $\lambda = 0.15409$  nm (the wavelength of the  $K\alpha$  radiation of Cu), the shape correction factor  $k = 1.05$ , and  $\theta$ , the diffraction angle. The XRD patterns (Fig. 30) show that the concentration of Al atoms has a significant influence on ZnO:Al film structure. At small content of Al atoms (0.1 % at. Al), the ZnO:Al films have a single-phase wurtzite ZnO structure with no preferential orientation in the film. The XRD patterns of the ZnO:Al films with an increased content of the Al (up to 23.1 at. %), show a ZnO (002) diffraction peak that, by the increase of the Al content, increases in intensity and broadening, fact that indicates that these films have very small crystallites (few nm) with  $c$ -axis preferential orientation. In addition, the location of the ZnO peak (112) has been shifted by the increase of the Al content to lower diffraction angles (ex. for ZnAl<sub>2</sub>O<sub>4</sub> peak (422) from 56.54° to 55.5°). This indicates the appearance in the ZnO:Al films with high content of Al of the cubic structure of ZnAl<sub>2</sub>O<sub>4</sub> in

mixture with the hexagonal structure of ZnO. The width of the diffraction ZnO peak (002) shows that the grain size decreases as the Al concentration increases. The average grain size of the films with Al concentration of 0.1 at.%, 2.5 at.%, 7.5 at.%, 13.8 at.% and 23.1 at.% is 14, 10, 8, 6 and 4 nm, respectively. This indicates that the Al atoms act as a grain growth inhibitor in ZnO films.

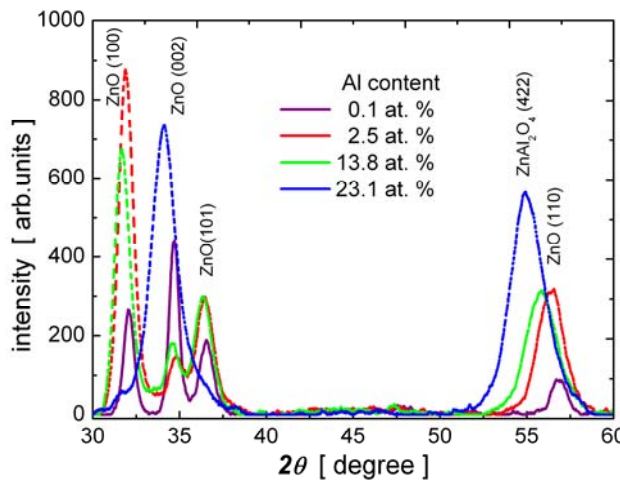


**Fig. 30** XRD patterns of ZnO:Al films prepared with the Al contents of 0.1, 2.5, 13.8 and 23.1 at.%.

The smaller grain size caused by higher Al concentration may result in higher grain boundary scattering of free charge carriers with effect of higher electrical resistivity. According to the resistivity measurement results, which are described below, we can reasonably infer that the increase of resistivity of the ZnO films at high concentration of doping aluminum atoms is mainly due to this effect.

Figure 31 shows that the electrical resistivity of the deposited films varied drastically with the change of the  $c_{Al}$  in the films. An optimum electrical conductivity (minimum of electrical resistivity of  $3.6 \times 10^{-3} \Omega \times \text{cm}$ ) has been obtained at  $c_{Al} = 1.5$  at.%. Decrease of  $c_{Al}$  from the optimum value results in an increase of the film electrical resistivity due to decrease of concentration of donor atoms. Increase of  $c_{Al}$  from the optimum value results in deposition of films with smaller grains, which results in an increase of the electrical resistivity by the effect of increasing of grain boundary scattering of free charge carriers. Variation of deposition parameters (gas pressure and composition, duration and frequency of voltage pulses) or further treatments of the deposited films (as substrate heating or annealing [92]) may result in an improvement of the electrical conductivity of the deposited films, this being subject of ongoing studies.

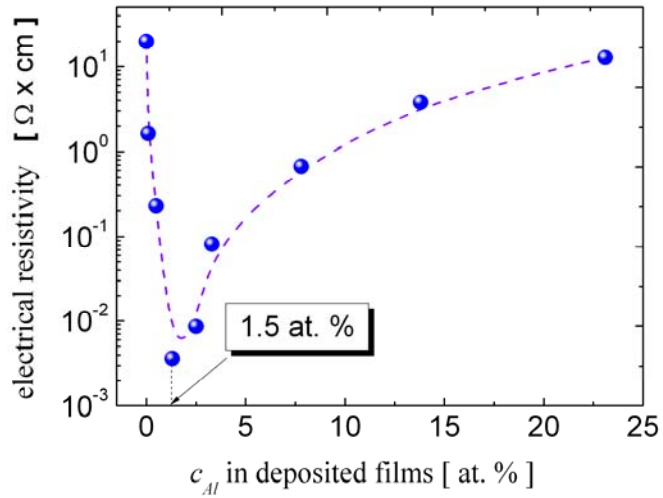


**Fig. 31 Dependence of the electrical resistivity of the deposited ZnO:Al thin films on Al concentration.**

In summary, control of Al doping of ZnO thin films deposited by HiPIMS can be achieved by sputtering of a negatively biased aluminum electrode placed in the proximity of the negative glow of the magnetron discharge. The biasing potential of the electrode is the key parameter that controls the flux of positive ions on the electrode and thus the concentration of Al atoms in vapor phase and in the deposited ZnO:Al thin films. Investigation of the optical and electrical properties of the deposited films showed a good optical transparency and, for the films with 1.5 at.% of Al atom concentration, an optimal (minimum) value of electrical resistivity of  $3.6 \times 10^{-3} \Omega \times \text{cm}$ . The minimum of the film electrical resistivity is explained by two opposite effects of increasing of the Al doping concentration in the deposited films, *i. e.* the increase of the free charge carrier density and the increase of boundary scattering of free charge carriers. The latter effect is suggested by XRD investigation of the film structure, which showed a decrease of the crystalline grain size with the increase of Al doping concentration.

## ***II.2 Application of low-pressure discharge plasma in atomic force microscopy and nanotechnology***

This section presents the results obtained by the author (L. Sirghi) in use of low pressure plasma to clean and hydrophilize surfaces of AFM probes {selected paper P6 [93]} and/or cover them by titanium dioxide {selected paper P8 [94]} or polyethylene glycol oxide (PEO) [95] thin films. Effects of plasma surface treatment and coatings on surface forces measured by AFM techniques in air and in water were investigated [93]. Hydrophilization of the AFM probe increased the tip-sample adhesion and friction forces on hydrophilic surfaces in air [93, 94]. Sirghi et al [96] have used this effect to enhance the chemical contrast in friction force microscopy (FFM) images of electron beam lithography nanopatterns on PEO surface (selected paper P9). The enhancement of adhesion and friction force in air is explained by the effect of capillary condensation of water at AFM tip-sample contact {selected paper P7 [97]}. The TiO<sub>2</sub> coating was used to control the hydrophilicity of AFM probes in a study of the effect of capillary condensation of water on the friction force at a single-asperity contact in ambient air {selected paper P8 [94]}. The PEO coating is used to reduce or eliminate the adhesion between AFM tips and biologic samples (living cells) with benefits for AFM imaging and indentation of living cells [98]. Sirghi et al [6] have shown that some AFM indentation experiments are strongly affected by the adhesion forces between the AFM tip and sample surfaces {selected paper P10 [99]}, while elimination of indenter-sample adhesion simplifies very much the analysis of indentation force versus displacement curves. Also, PEO covered AFM tips were used to study the optimal conditions for protein transfer in microcontact printing [3].

Invention of atomic force microscope [100] provided a powerful tool for a variety of research areas as colloidal physics [101], tribology [102], molecular [103] and cellular [104] biophysics, material research [105], nanotechnology [106], etc. These applications require a good control of chemistry of the atomic force microscopy (AFM) probes. The AFM techniques use the interaction between a probe with a very sharp tip (apex curvature radius of 5-10 nm) and sample surfaces in order to acquire topography images of the surfaces or to measure surface and molecular forces. In AFM imaging it is important to decrease as much as possible the region of interaction by manufacturing very sharp tips and eliminating long range surface forces. Measuring of molecular bonding strength and stretching force of single molecules requires chemical binding of molecules to the chemically functionalized surfaces of AFM tips [103]. Usually, these applications use gold covered AFM probes functionalized by wet chemistry technique of self assembled monolayers (SAM) of organothiol molecules [107]. Chemical functionalization of silicon oxide nanoprobes is

possible by SAM depositions of organosilane molecules [108]. It is widely recognized that AFM measurements of surface forces are strongly affected by the chemistry of the AFM tip and sample surfaces [109, 110]. This led to initiation of a new AFM technique, i. e. chemical force microscopy (CFM), which is used to probe at nanoscale chemically different regions on a sample surface [109]. The chemistry of the AFM probe surfaces can be controlled by several surface functionalization techniques including coating with thiols, silanes, polymer, tungsten carbide, diamond-like and metal oxide layers, or attachment of carbon nanotubes or colloidal particles [111, 112]. However, because of the surface adsorption of airborne and package-released organic contaminants [113], the surface chemistry of most of the as-received commercial AFM probes remains unknown. Cleaning of the AFM probe surfaces is the simplest probe treatment that can be done to control the probe surface chemistry. Various cleaning methods for silicon and silicon nitride AFM probes are currently used in different laboratories for removing the thin films of the contaminant organic molecules adsorbed on the probe surfaces [114, 115] or for removing contaminant particles attached to the tips of the AFM probes [116, 117]. Because of the small size of the AFM tips, direct characterization of the tip surface chemistry is difficult and in most of the cases the quality of the surface cleaning is probed indirectly by the reproducibility of the force measurements. Bonaccorso and Gillies [118] showed that it is possible to reveal contamination on AFM cantilevers by measuring the contact angle of sessile water microdrops on their surface or by tip-air bubble force measurements in water. The effectiveness of different cleaning methods used for removing of organic contaminants adsorbed on silicon and silicon oxide surfaces was ascertained by Time of Flight-Secondary Ion Mass Spectroscopy (TOF-SIMS) and X-ray Photoelectron Spectroscopy (XPS)[119], scanning Auger Microscopy [113], Fourier Transformed Infrared Attenuated Total Reflectance [120] and in situ spectroscopic ellipsometry [121]. It is worthwhile to note that however good is the cleaning of the AFM probe and sample surfaces, the contamination by absorption of airborne organic molecules during the AFM measurements in air is inevitable [122]. Contamination through organic molecule adsorption can easily occur during the AFM measurements in liquid as well. Therefore, cleaning of AFM probes is required for most of the AFM measurements and especially for measurements of surface adhesion forces [112].

Negative glow plasma in low-pressure air has been used by Sirghi *et al* [93] to clean silicon surfaces of the AFM probes and the results were compared by the classical wet chemistry method of piranha solution. This particular plasma cleaning method creates on the AFM probe surfaces many radical hydroxyl groups, which makes the probe surface super hydrophilic. This property of the plasma cleaned AFM probes was used by Sirghi et al in a recent paper [96] investigating the chemical contrast obtained in friction force and phase lag AFM images of nanopatterns fabricated

by electron beam lithography on polyethylene glycol oxide (PEO) surface. Cleaning and hydrophilization of the AFM probe surface strongly enhanced the contrast in friction and phase lag images of patterns. It has been shown that plasma cleaning and hydrophilization of AFM probe and sample surfaces have a strong impact on surface forces in water and air (Sirghi et al) [93]. The capillary force of the water meniscus formed through capillary condensation at the AFM tip sample contact is strongly dependent on surface hydrophilicity and air humidity. The contrast in adhesion and friction force images acquired in air has been used by Sirghi et al [123, 124] to discriminate between nanoscopic surface regions of different hydrophobicity on UV irradiated TiO<sub>2</sub> thin films obtained by RFMSD.

An alternative method to control the chemistry of AFM probe surface is coating of the probes by thin solid films. Sirghi et al [94] covered the AFM probes by thin layers of TiO<sub>2</sub> in order to control the probe surface hydrophilicity by UV radiation and study the dependence of friction and adhesive forces in air on the AFM probe and sample surface hydrophilicity. The AFM probes used in surface force measurements on biologic probes (proteins and cells) were covered by a thin polyethylene glycol oxide (PEO) layer, a material known as protein antiadhesive and cell repellent. Such probes were used in a study of adhesion force in air between fibronectin on PEO surface, a study relevant for the transfer of fibronectin on PEO surface by microcontact printing [95]. The PEO coating is also used to reduce or eliminate the adhesion between AFM tips and living cells with benefits for AFM imaging and indentation of living cells. Elimination of indenter-sample adhesion improve the AFM imaging in liquid of living cells and simplify very much the analysis of indentation force versus displacement curves [98].

### **II.2.1 Plasma cleaning and hydrophilization of silicon surface of AFM probes**

This section presents results reported by the Sirghi *et al* [93] on plasma cleaning method used to clean silicon and silicon nitride surfaces of the AFM probes. The classical wet chemistry method of piranha solution used to oxidize and remove organic contaminants from silica surface was used as reference cleaning method in this study. The study has shown that the silicon surface of commercial atomic force microscopy (AFM) probes loses its hydrophilicity by adsorption of airborne and package-released hydrophobic organic contaminants and cleaning of the probes by acid piranha solution or discharge plasma removes the contaminants and renders very hydrophilic probe surfaces. Time-of-flight secondary-ion mass spectroscopy (ToFSIMS) and X-ray photoelectron spectroscopy (XPS) investigations were performed to show that the native silicon oxide films on the AFM probe surfaces are completely covered by organic contaminants for the as-received AFM probes, while the cleaning methods effectively remove much of the hydrocarbons

and silicon oils to reveal the underlying oxidized silicon of the probes. Also, it has been shown that cleaning procedures affect drastically the results of adhesive force measurements in water and air. Thus, cleaning of silicon surfaces of the AFM probe and sample cancelled the adhesive force in deionized water. The significant adhesive force values observed before cleaning were attributed to formation of a bridge of hydrophobic material at the AFM tip-sample contact in water. On the other hand, cleaning of the AFM tip and sample surfaces resulted in a significant increase of the adhesive force in air. This result was ascribed to presence of water soluble contaminants at the tip-sample contact, contaminants that lower the capillary pressure in the water bridge formed by capillary condensation at the AFM tip-sample contact, and this consequently lower the adhesive force.

Two plasma cleaning methods were investigated: (I) the AFM probes were placed on the cathode surface of a d.c. discharge in air at low pressure, the probes being protected by an electric shield against the high electric field of the cathode sheath [93]; (II) the AFM probes are immersed in the negative glow plasma of a d.c. discharge in air at low pressure, the probes being placed on a thick glass slide placed on the cathode [125]. Sketches illustrating the two plasma cleaning methods are given in Fig. 32. Both methods use the negative glow discharge plasma of a d.c. discharge in air at pressure of 900 Pa, discharge voltage of 350 V, and discharge current intensity of 5 mA in a commercial plasma sputtering/cleaning system (Edwards Sputter Coater S150B) working in the cleaning mode. The cathode was a tantalum disk with diameter of 10 cm. In the method I, the shield created an electric field-free volume where the oxygen radicals produced in the negative glow plasma in air can diffuse in through the open sides. In the method II, the probe surface was maintained floating in negative glow plasma by a thick glass slide. In the latter case, the cleaning is attributed to radical oxygen species and positive ion bombardment of the floating probe surface.

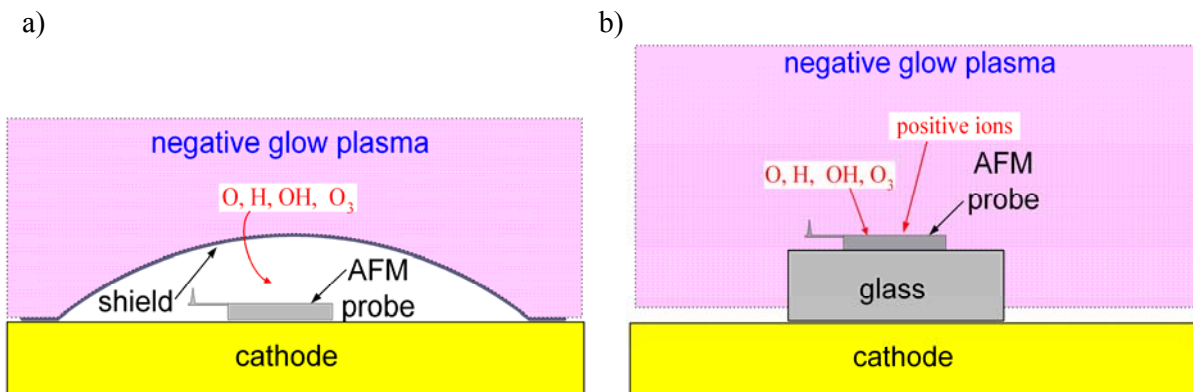


**Fig. 32** Sketches illustrating the two methods used for plasma cleaning of the AFM probes. The dimension of the AFM probe is exaggerated for clarity.

Plasma cleaning of the AFM probes may harm the AFM probes by altering the cantilever elasticity, tip geometry, and quality of metallic reflex coating. The integrity of the AFM probe cantilevers after the cleaning was checked by measurements of thermal noise spectra. No significant changes in cantilever resonant frequency was observed, which proves that the elasticity of the cantilevers was not affected by the cleaning procedure. The integrity of the probe tips after cleaning was checked by analysis of images of sharp edges (nominal curvature radius of 5 nm) of a grating sample (TGG1 from NT-MDT). Cleaning resulted in no significant change of tip curvature radius. The damage caused by cleaning procedure to the reflex coatings of the AFM probes have been evaluated by measurements of the total intensity of the laser light beam reflected by the as-supplied and cleaned AFM probes. It was found that the reflectivity of the aluminum reflex coating decreased to about 50% of the initial values, while the reflectivity of the gold reflex coating decreased to no less than 90% of the initial values.

The contaminant molecules are hydrophobic and they render a hydrophobic character to the surface on which they are adsorbed. Thus, a simple way to check the cleanness of the AFM probes is to determine the water contact angle of their surfaces. Cleaning of silicon AFM probes removes the contaminants and renders very hydrophilic probe surfaces. States of AFM probe surfaces before cleaning, after pre cleaning with organic solvents, and after cleaning by the two methods were evaluated by measurements of water contact angle and adhesive force. Figure 33 presents results of water contact angle measurements as function of treatment time. Both plasma cleaning methods are efficient in removing contaminants from AFM probe surfaces, a treatment time of 10 minutes resulting in a decrease of water contact angle from 90° to about 5°.

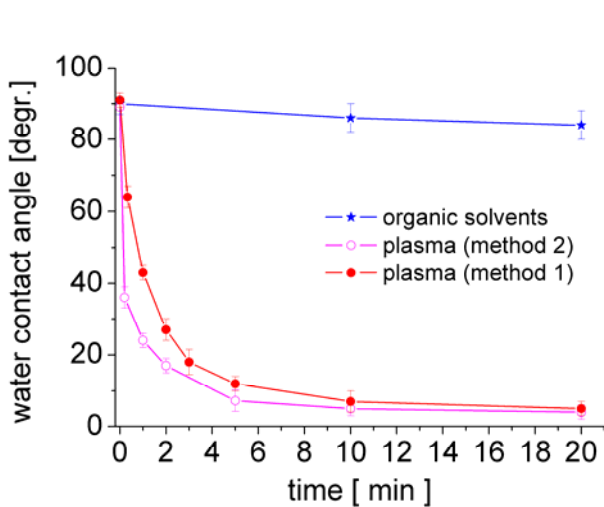


**Fig. 33 Water contact angle measured at different treatment time values (silicon probes NSG 11 from NT-MDT)**

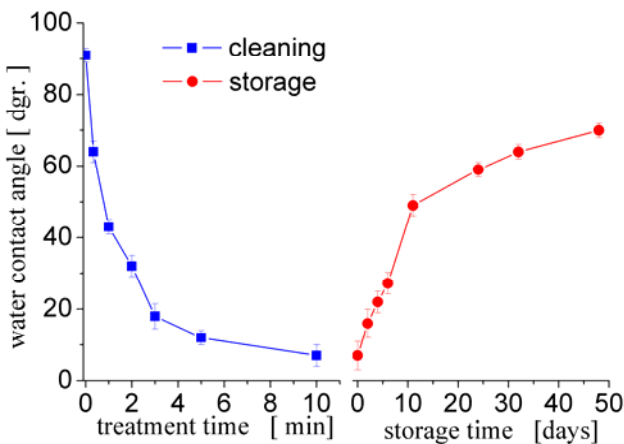


**Fig. 34 Water contact angle measured at different treatment time values and after storage in normal laboratory conditions (silicon probes NSG 11 from NT-MDT).**

Also, the water contact angle measurements showed that cleaning by organic solvents is not efficient. Water contact angle measurements for AFM probes cleaning by Piranha solution (not shown) showed same cleaning efficiency as plasma cleaning methods [93]. The improvement of the AFM probe surface hydrophilicity is not permanent. As a result of storage in air, the probe surface hydrophilicity worsens due to the absorption of airborne hydrophobic contaminants (hydrocarbons). Thus, the water contact angle of AFM probes increased to about 70 degrees in 50 days (Fig. 34). However, the water contact angle of the probe surface during storage in air did not reach the value of the water contact angle of the as-received AFM probes. This may be attributed to difference in the contamination of the as-received probes and cleaned and air-exposed probes.

Surfaces of the as-received and cleaned AFM silicon probes provided by different manufacturers were chemically characterized by TOF-SIMS and XPS techniques in a combined XPS and TOF-SIMS surface analysis system. The positive ion spectrum of the as-received probe supplied by NT-MDT Co. (Fig. 35, upper part) indicates the presence of molecular fragments ( $\text{CH}_3\text{Si}^+$  and  $\text{C}_3\text{H}_9\text{Si}^+$ ) that are characteristic of surface contamination by poly(dimethylsiloxane) (PDMS). The same results were found by Lo *et al* [120] for the as-received AFM probes supplied by Park Scientific Instruments. For the as-received AFM probes supplied by Nanosensors<sup>TM</sup> (Fig. 35, below part), the main contaminant materials identified on the probe surface were airborne hydrocarbons with little or no trace of PDMS. The positive ion spectra of as received and plasma-cleaned AFM probes provided by NT-MDT are shown in the Fig. 36 and indicate that the plasma cleaning successfully removed the PDMS contaminants. The residual contaminants on the cleaned probe are composed of a mainly hydrocarbon material ( $\text{C}_x\text{H}_y$ ) but with the underlying probe now being detectable as shown by the higher silicon ion peak together with the appearance of boron in the spectra. A similar result has been obtained in case of the AFM probes provided by Nanosensors<sup>TM</sup>.

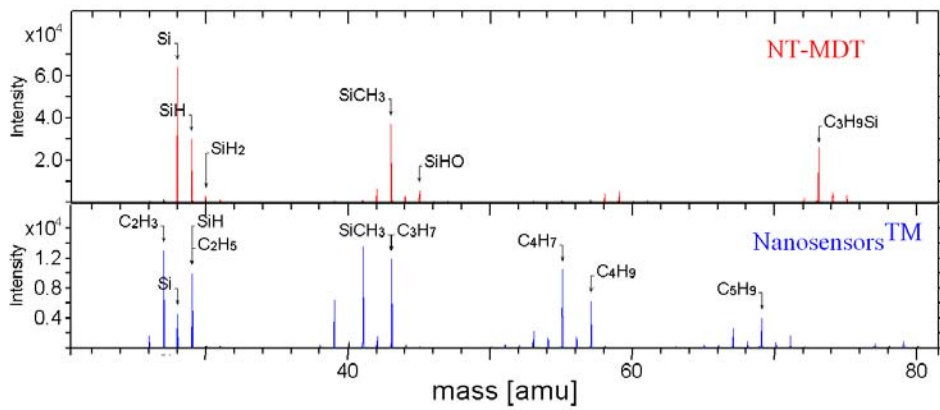


**Fig. 35 Positive ion TOF-SIMS spectra of silicon surface of the as-supplied AFM probe provided by NT-MDT Co. (CSG 11) and Nanosensors™ (PPP-BSI). Spectra shows contamination of probe surfaces with poly(dimethylsiloxane) (fragments  $\text{CH}_3\text{Si}^+$  and  $\text{C}_3\text{H}_9\text{Si}^+$ ) and airborne hydrocarbon.**

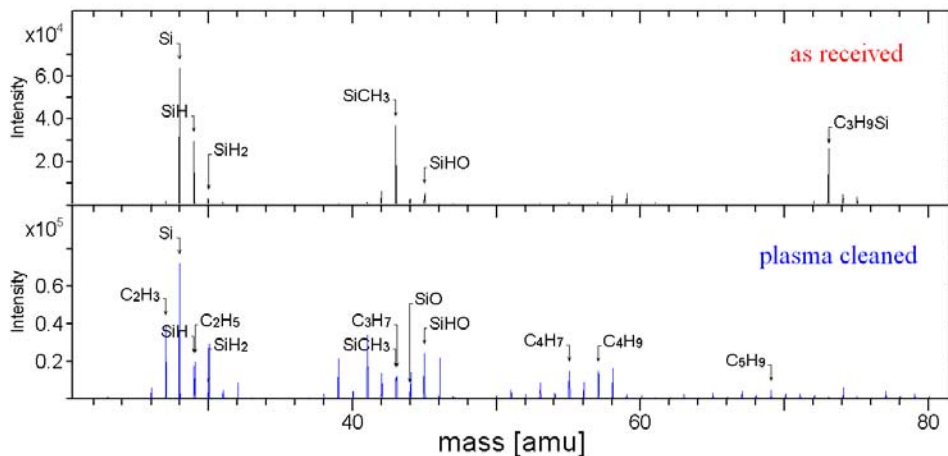


**Fig. 36 Positive ion TOF-SIMS ( $\text{Bi}^+$  primary ion gun) spectra of silicon surfaces of the as-supplied and plasma-cleaned AFM probes provided by NT-MDT Co. (CSG 11).**

XPS analysis of the Nanosensors™ probes before and after cleaning showed principally the presence of C, O, and Si with the normalized atomic concentrations being reported in Table 5. By deconvolution of the C1s core level XPS spectra, it has been observed two components, C0(285eV) and C1(285.5eV), that were attributed to hydrocarbon bonding (C-C/C-H) and C-O single bonding, respectively. The high proportion of the C-H component (98%) confirms the dominance of hydrocarbon contamination observed in the TOF-SIMS spectra. Following the cleaning procedures a significant reduction of the carbon content is observed with corresponding increases in the silicon and oxygen concentrations. In this respect, the plasma cleaning seems to be more effective treatment for carbon reduction than the cleaning by piranha solution.

**Table 5. Elemental composition of the AFM probe surfaces (Average of three measurements; standard deviation in brackets)**

sample	C [at%]	O [at%]	Si [at%]
as-received	58.4 (8.8)	13.06 (1.7)	28 (7.5)
plasma-cleaned	19.9 (6.2)	32.8 (4.9)	47.24 (3.7)
piranha-cleaned	28 (5.8)	23.8 (2.5)	48 (6.3)

While plasma cleaning method is effective, the removal of the airborne hydrocarbon contaminants from the AFM probe surface is not permanent. Normal storage of the cleaned probes in air results in coverage of the probe surface with a layer of hydrocarbon after only a few days. Positive ion spectra of the cleaned AFM probe recorded after the probe had been stored in ambient laboratory air for 6 days (not shown) indicates that the surface is already contaminated with a sufficient amount of the airborne hydrocarbons as to mask almost completely the  $\text{SiOH}^+$  peaks in the TOF-SIM spectra. Long-time storage of the Nanosensors<sup>TM</sup> probes on silicone mat in plastic boxes results in contamination with PDMS. TOF-SIMS analysis (spectrum not shown) of probe surface after six month of storage revealed a complete coverage of the surface with PDMS contaminant.

### **II.2.2 Coating of AFM probes by plasma assisted depositions of thin films**

Hydrophilic AFM probes were also obtained by sputtering deposition of amorphous titanium oxide on commercially available silicon nitride cantilevers (Olympus, OMCL-TR800PSA-1) in a low power (20 W) r.f. magnetron discharge in Ar-O<sub>2</sub> gas mixture at 10 mTorr {Sirghi et al [94]}. In this study the AFM probes were covered by thin layers of TiO<sub>2</sub> in order to control the probe surface hydrophilicity by UV radiation. The depositions were made at low r.f. discharge power to prevent destruction of the cantilevers of the AFM probes. Depositions at relatively large values of r.f. discharge power (200 W) resulted in a completely loss of cantilever elasticity. Details on the deposition method and film characterization are given in section II.1.1. Measurements of the film thickness performed by ellipsometry yielded values around 10 nm and measurements of the cantilever resonant frequency before and after the deposition showed little modification of the cantilever elasticity constant (nominal value of 0.57 N/m). The hydrophilicity of the as-received silicon nitride and TiO<sub>2</sub> covered AFM probes was characterized by measurements of water contact angle on sessile droplets on the AFM probe basis. The TiO<sub>2</sub> covered AFM probes after UV

irradiation showed a hydrophilic character, its water contact angle being around  $10^\circ$ . On the other hand, for the as received silicon nitride AFM probes showed a slightly hydrophobic character, their water contact angle being around  $100^\circ$ . The hydrophilic and hydrophobic probes were used in friction force measurements in a study of the effect of water vapor on nanoscale friction {Sirghi et al [94]}. In the followings, the main results of the study are presented.

Figure 37 presents the results of the friction force microscopy (FFM) measurements for the hydrophobic AFM probe and a hydrophilic silicon surface (water contact angle of  $50^\circ$ ) at four values of RH. The plots show a dependence of the average friction force on the external load in good agreement with the model proposed by Fogden and White [126] and extended by Sirghi [94], model which foresees a dependence of the friction force enhanced by the water meniscus-generated load  $L_0$ , and friction force at meniscus contact lines,  $F_{wm}$ , according the equation

$$F_f = \tau \cdot \pi \cdot \left[ 3R_t(L + L_0)/4E^* \right]^{2/3} + F_{wm}. \quad (18)$$

Here,  $\tau$  is the shear strength of the contact,  $L$ , the externally applied load,  $R_t$ , the AFM tip radius, and  $E^*$ , the combined Young's modulus of the AFM tip and sample surfaces. For hydrophobic AFM probe, there were observed values of  $F_{wm}$ , much smaller than the shear friction generated by  $L$  and  $L_0$ . To determine  $L_0$ , measurements of the tip-sample pull-off force were performed at 100 points randomly placed on a sample surface area of  $1\mu\text{m} \times 1\mu\text{m}$ . The measurements yielded Gaussian-like distributions ( $1\text{nN}$  in half width) of pull-off force value probability and the most probable values are also displayed in Fig. 37. The pull-off force values were close to the minimum value of the external load in friction force curve measurements.

Results of the friction measurements performed by the hydrophilic AFM probe on the same hydrophilic silicon sample showed a much stronger dependence of the tip-sample friction force on the RH. While the RH was increased, the friction force increased in relatively dry atmosphere but suffered a drastic decrease in very humid atmosphere (see Fig. 38). The turning point in the friction dependence on the RH occurred at a value around 50% when the measurements showed a large dispersion of the friction force values (data not shown). The dependence of the friction force on the external load fits well the theoretical dependence described by Eq. (18), especially at very low (1%) or very high (94%) RH values. Noticeable large fluctuations of friction force were observed in these measurements and the error bars on the plots showed in Fig. 38 represent the root mean square values of these fluctuations. The amplitude of friction force fluctuations depended also on the RH, larger fluctuations being observed at larger friction force values. The strong effect of the RH on the friction force in this case can be attributed mainly to the contribution of the water meniscus friction

force  $F_{wm}$ . Thus, the plots of the friction force versus the external load in dry atmosphere appear to be shifted towards larger values by the significant values of  $F_{wm}$ , while the low friction force values observed in very humid atmosphere (RH = 94%) are due to a very low value of  $F_{wm}$ . Since changes in  $L_0$  may also contribute to the effect of the RH on the friction force, measurements of pull-off force were also performed. However, for this case the measurements could not determine a unique value for the pull-off force. Except for the case of RH = 1%, relatively wide distributions of the pull-off force values were obtained. The distributions showed two most probable pull-off force values, which are shown also in Fig. 38. The wide distribution of the pull-off force values can be attributed to the formation of a large variety of water menisci at the tip-sample contact.

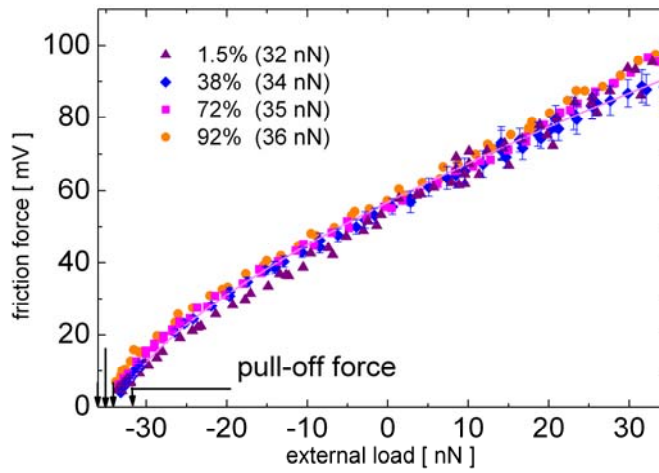


**Fig. 37** Plots of the average friction force versus the external load at four values of RH for the hydrophobic silicon nitride tip and Si(100) surface.

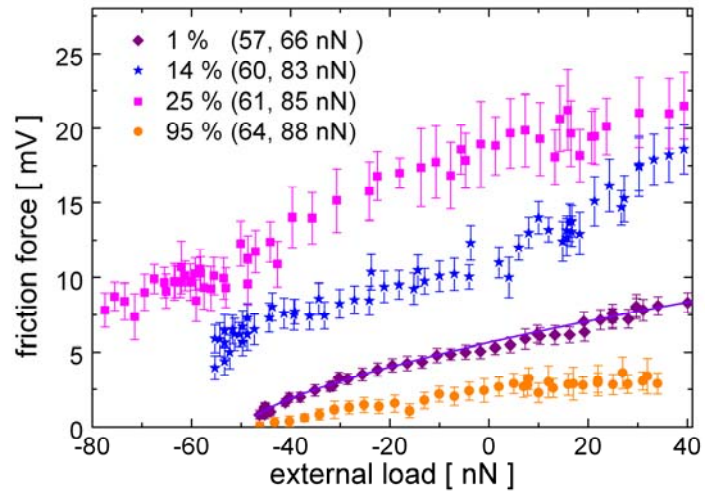


**Fig. 38** Plots of the average friction force versus the external load at four values of RH for the hydrophilic titanium dioxide tip and Si(100) surface.

In summary, FFM measurements on a hydrophilic silicon sample showed a weak effect of humidity on friction for a hydrophobic AFM tip and a strong and complex effect for a hydrophilic tip. The variation of the load (adhesive force) generated by the water meniscus could not solely explain the observed effect of RH on the friction force between hydrophilic surfaces (which showed friction at no or very small load). Therefore, a part of the friction force between hydrophilic surfaces was attributed to the process of dragging of the capillary condensed water by the tip-sample contact (see the selected paper P8).

In a recent work {Ruiz *et al* [95]}, Sirghi used polyethylene glycol oxide (PEO) coated AFM probes to study the optimal conditions for the protein transfer from a elastomer [poly(dimethylsiloxane) PDMS] stamp to the PEO surface. The PEO films have been deposited by plasma-enhanced chemical vapor deposition in a pulsed (time-on = 10ms, and time-off = 100ms) capacitively coupled r.f. plasma at low nominal power (5 W) in pure Diethylene Glycol Dimethyl Ether (DGDE) vapor at pressure of 15 mTorr. The deposition substrates (silicon wafers and AFM probes) were placed on the passive electrode (electrically connected at the stainless steel reactor chamber, which was grounded) with the face towards the active electrode, which was positioned at 140 mm above the substrate (Fig. 39). The electrodes consisted in stainless-steel disks with diameter of 140 mm. More details on the deposition system and characterization of the deposited PEO thin films are given in reference [127]. The film characterization [35] has demonstrated that this particular deposition setup allowed for fabrication of stable PEO thin layers with a high retention of polyethylene oxide character. Such coatings have been proved to be highly stable in water, ethanol or PBS, and to provide a non-fouling surface for proteins and cells. However, it is possible to obtain micro patterns of proteins on PEO surface in dry conditions by microcontact printing [95] and microspotting [128] in order to obtain bioadhesive/biorepellent surface contrast. Figure 40 shows a sketch of the microcontact printing process of fibronectin on PEO surface and an AFM image of the obtained micropattern. A PDMS stamp was inked by protein solution in PBS at different value of pH and salt concentration in order to find optimal conditions for protein transfer from the PDMS stamp to the PEO surface. The inked stamp was kept in contact with the PEO surface for 10 minutes and removed. This left a pattern of proteins on PEO surface thus creating a protein or cell adhesive/repellent surface contrast.

Atomic force microscopy measurements of the adhesive force between a PEO covered AFM probe (NSG 11 from NT-MDT) and poly-l-lysine (PLL) covered PDMS surface were performed in order to study the optimal conditions for the protein transfer from a PDMS stamp to the PEO surface. A sketch of the AFM experiment is shown in Fig. 41.

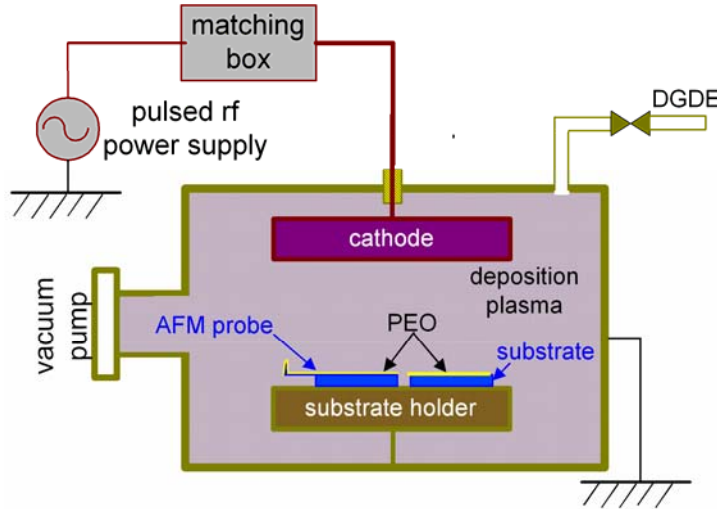


**Fig. 39** Sketch of the PECVD reactor used for PEO depositions on AFM probes and silicon substrates. The reactor used a low power ( 5W) pulsed (time-on 10 ms, time-off 100 ms) capacitively coupled r.f. discharge in Diethylene Glycol Dimethyl Ether (DGDE) vapour at 15 mTorr.

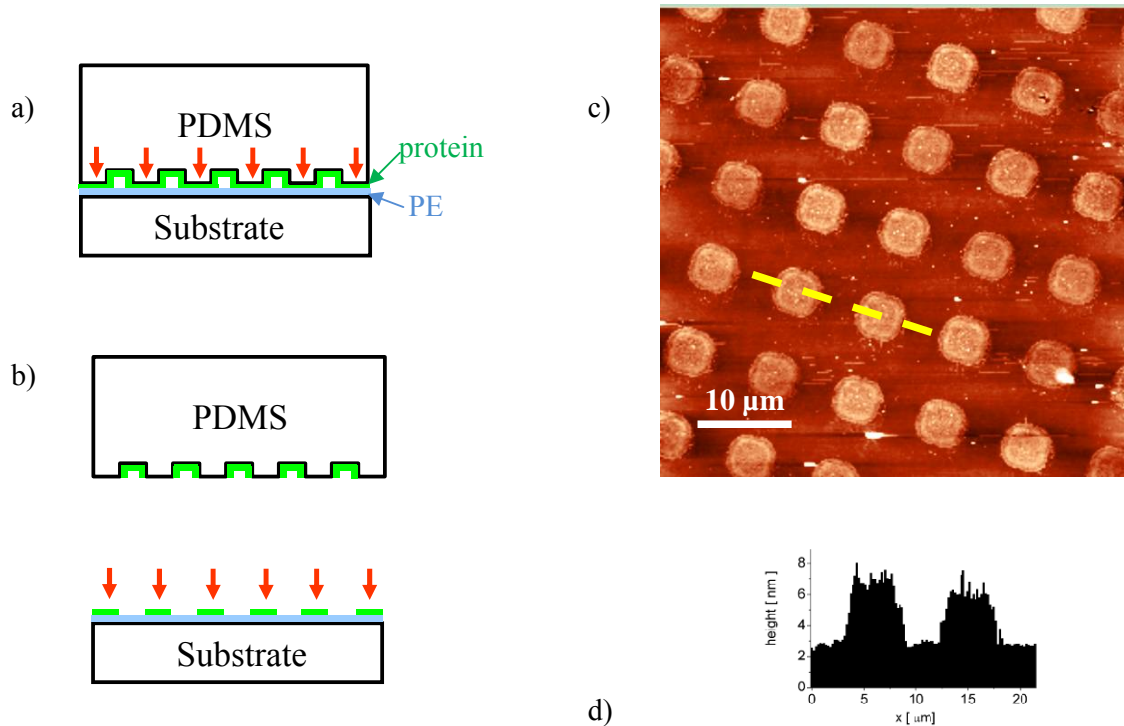


**Fig. 40** Process of fabrication of protein patterns on PEO surface by microcontact printing. a) The inked PDMS stamp is driven into contact with the PEO-coated substrate and kept in contact for certain time; b) The PDMS stamp is lifted up vertically from the substrate to leave the protein pattern; c) AFM topography image of fibronectin patterned on PEO surface by microcontact printing; d) The height profile along the dashed line on the AFM image.

The sample substrate was a PDMS slab with the thickness of about 2mm prepared by curing molds of polymer:curing agent (Sylgard from Dow-Corning Co.) for 3 hours at 60°C. The substrate was inked by phosphate buffer saline (PBS) solution of PLL with different salt concentration and pH. The PEO was deposited on the AFM probes by the same method as that described above. The radius of the tip of the AFM probe was measured by scanning a silicon grating with very sharp topography features (TGG1 from NT-MDT). The radius of the AFM tip was about 7 nm before PEO deposition and 24 nm after PEO deposition, which indicates a thickness of 17 nm of the PEO layer on the AFM tip. The adhesive force was determined as the value of the AFM tip-sample detachment force observed on retract force-displacement curves acquired on arrays of 10 x 10 points homogeneously distributed on an area of 1 $\mu$ m x 1 $\mu$ m of the sample surface. Figure 42 shows the histograms of the adhesive force between the PEO coated AFM probe and PLL adsorbed to PDMS at different values of pH and buffer concentration. The measurements show that the adhesive force increases by the decrease of the either pH or salt concentration. The adhesive force was dependent on air relative humidity (RH), which indicated that it was created mainly by the capillary water meniscus formed at tip-sample contact. The histograms shown in Figure 41 were obtained at relatively low RH. At large values of the RH the distributions of the adhesive force (not shown) broadened and shifted towards larger values. Patterns printed at low pH and salt concentration may collapse due to the strong adhesion force between the inked stamp and PEO surface.

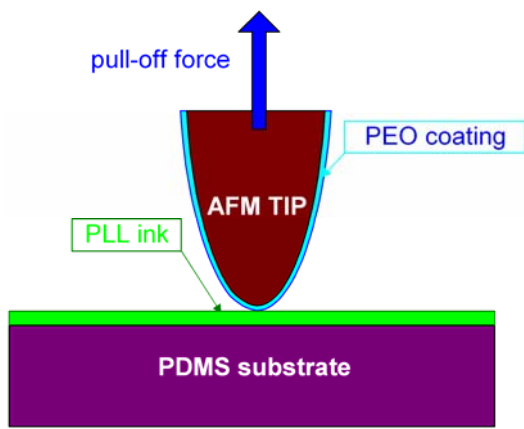


**Fig. 41 Sketch of the AFM study of adhesion of PLL protein on PEO surface in dry atmosphere.** The AFM tip was covered by a thin PEO layer while the PDMS substrate was covered by a PBS solution of PLL. The pull-off force required to detach the AFM tip from the sample surface indicates the adhesion of protein to PEO surface in dry atmosphere.

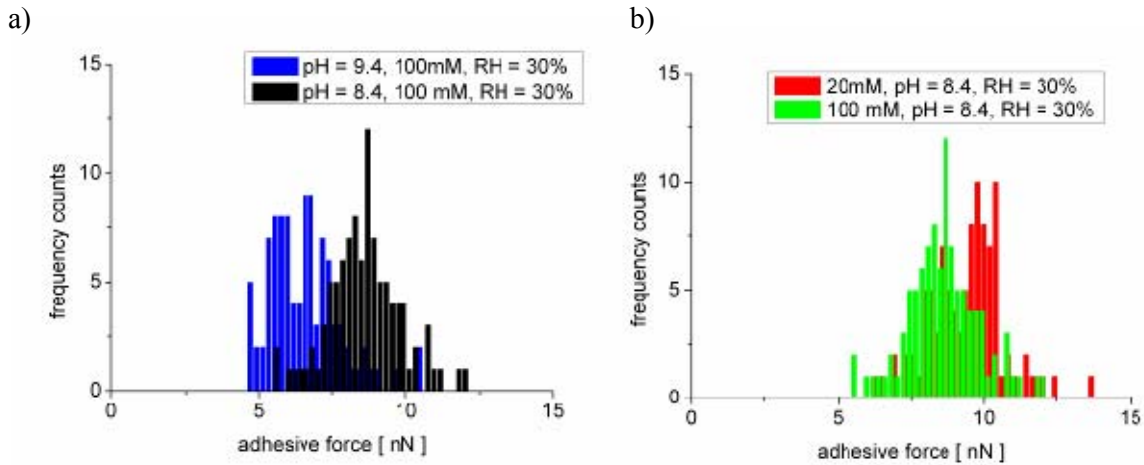


**Fig. 42 Histograms of adhesive force values that were measured between a PLL-coated PDMS surface and a PEO-coated AFM probe on an array of  $10 \times 10$  points distributed in  $1\mu\text{m}^2$  area. (a) shows the dependence of the adhesive force on pH while (b) on the buffer concentration.**

On the other hand, low quality patterns are fabricated at high pH and salt concentration due to the weak adhesive force, which is cause of a low protein transferring efficiency. Therefore, these measurements show that optimal conditions for micro contact printing of protein patterns are situated at intermediate values of pH and salt concentration.

In summary, AFM tips were covered by thin PEO layers in order to study the optimal conditions of protein transfer from the surface of a PDMS stamp to PEO surface, a process important in fabrication of bioadhesive/biorepellent micropatterns by microcontact printing [95]. The study revealed a strong dependence of the adhesive force of protein on PEO surface on air humidity, pH and salt concentration of protein solution. It has been concluded that good protein transfer from the inked PDMS stamp to the PEO surface required moderate values of pH and salt concentration of the protein solution. The measurements revealed also that the air humidity plays an important role in the process of microcontact printing and protein transfer from the PDMS to PEO surface.

### **II.2.3 Effect of plasma surface treatment of AFM probe and sample surfaces on microscopic adhesive forces.**

Hydrophilic surfaces do interact in aqueous solutions by weak Van der Waals, electrostatic double layer, and stearic forces [129]. Atomic force microscopy measurements showed that all these forces in case of cleaned silicon (covered by native silicon oxide layers) surfaces of AFM tip and samples in pure water are negligible small. This section presents and discusses results of such AFM adhesive force measurements performed by Sirghi et al [93] in deionized water with as-received and plasma cleaned tips. It is shown that contaminated surfaces of silicon AFM probes and

samples interact by a finite short-range adhesion force, while the adhesive force between plasma cleaned surfaces is negligible. The finite adhesive force between contaminated silicon surfaces in water is explained by the formation of a capillary bridge of hydrophobic material between the AFM tip and sample surfaces. A similar explanation was used by Kanda *et al* [130] to explain the very large adhesion force between silica and mica surfaces in an aqueous solution of n-propanol at high concentration. Typical force–distance curves measured in deionized water before and after plasma cleaning of the AFM probe and sample surface are presented in Fig. 43, parts (a) and (b), respectively. The force-distance curves for the as-received AFM silicon probe and the silicon sample showed a snap-in instability on the approach part at a tip-sample distance of about 2 nm and a snap-out instability on the retract part, at a tip-sample distance of about 6nm. This pattern of the force-distance curves indicates formation of a bridge of contamination material at the tip-sample contact. The snap-in instability on the approach part of the force-distance curve corresponds to coalescence of the layers of contaminants on the tip and sample surfaces. Therefore, the snap-in distance can be considered as a rough indicator of the thickness of contaminant layers on the AFM tip and sample surfaces [131], which in this case is less than 2 nm. While the tip is pushed further towards the sample surface the contaminant material gathers at the contact and form a meniscus that surrounds the contact. When the tip is retracted, the bridge of contaminants in water is elongated until it breaks up at certain tip-sample separation distance. This behavior of the bridge of contaminants at the tip-sample contact in water is similar to the behavior of the water bridge formed by capillary condensation of the water vapor at the tip-sample contact in ambient air. Generally, formation of a bridge of different material at the contact raises a meniscus adhesive force that is roughly computed as [129]:

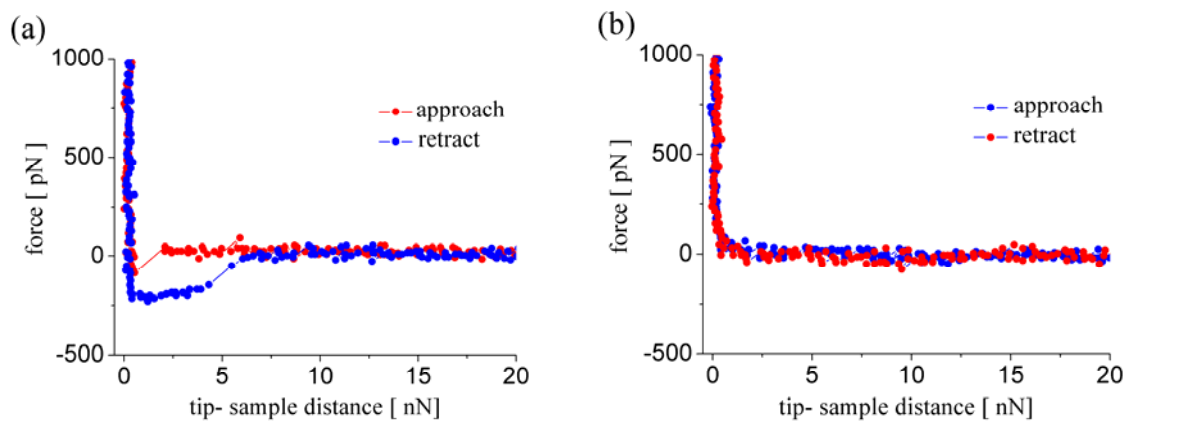


**Fig. 43** Typical force-distance curves measured on silicon in deionized water with as-supplied (a) and plasma-cleaned (b) AFM probe, respectively. The AFM probe used in this experiment was CSG 11 from NT-MDT and it had the nominal cantilever spring constant of 0.1 N/m and the nominal tip curvature radius of 10 nm.

$$F = 4\pi \cdot \sigma_{wc} \cdot R \cdot \cos \theta, \quad (19)$$

where  $F$  is the adhesive force,  $\sigma_{wc}$ , the surface free energy of the contaminant-water meniscus interface, and  $R$ , the equivalent radius of the contact (in this case, because the sample surface is flat, the radius of the AFM tip). Taking into account values of 0.28 nN for  $F$ , 10 nm for  $R$  and 0.5 for  $\cos \theta$  computes a value of 4.4 mJ/m<sup>2</sup> for the  $\sigma_{wc}$ , which is much smaller than the surface free energy of water (72 mJ/m<sup>2</sup>). This small value of  $\sigma_{wc}$  is an indication that the organic contaminant molecules are not very hydrophobic. Cleaning of the AFM probe and sample surfaces in plasma resulted in cancellation of any adhesive force between surfaces. Figures 43 (b) shows that there is no long- or short-range force between cleaned silicon surfaces in water. Absence of any electrostatic double layer force on the force-distance curves shows that either contaminated or clean silicon surfaces do not electrically charge in the deionized water (pH = 6). Although the adhesive force between contaminated AFM silicon probe and sample surfaces is small, its value (287 pN) is important for the case of AFM measurements on biological samples, where typical values of forces may be below 100 pN [132].

Typical force–distance curves measured in ambient air (RH = 33% and 24 °C), before and after plasma cleaning of a silicon AFM probe (NSG 11 from NT-MDT with cantilever spring constant of 15 N/m and nominal tip curvature radius of 10 nm) are presented in Fig. 44, parts (a) and (b), respectively. Prior to the adhesive force measurements, the surface of the silicon sample was cleaned by acetone, ethanol and deionized water and dried in pure nitrogen. As a result of plasma cleaning of the AFM probe, the tip-sample adhesive force increased about three times. A statistical analysis of the adhesive force values measured for a set of one hundred force-distance curves for the as-supplied AFM probe showed a Gaussian distribution with the most probable value of 9.2 nN and the width of 5.3 nN. Same measurements performed after plasma cleaning of the AFM probe resulted in a Gaussian distribution with the most probable value of 29.4 nN and width of 5.3 nN. Therefore cleaning of the AFM probe resulted in an increase of tip-sample adhesive force about three times. This strong effect of plasma treatment of AFM probe surface on the AFM measurements of adhesive force in air is explained by the capillary force origin of adhesive force at a nanoscopic contact between hydrophilic surfaces in humid air.

Since the main component of the AFM tip-sample adhesive force in the ambient air is the capillary force of the liquid bridge formed by capillary condensation of water at the tip-sample contact [133], the increase of the adhesion force in these experiments is attributed to the effect of surface cleaning on the properties of the capillary bridge.

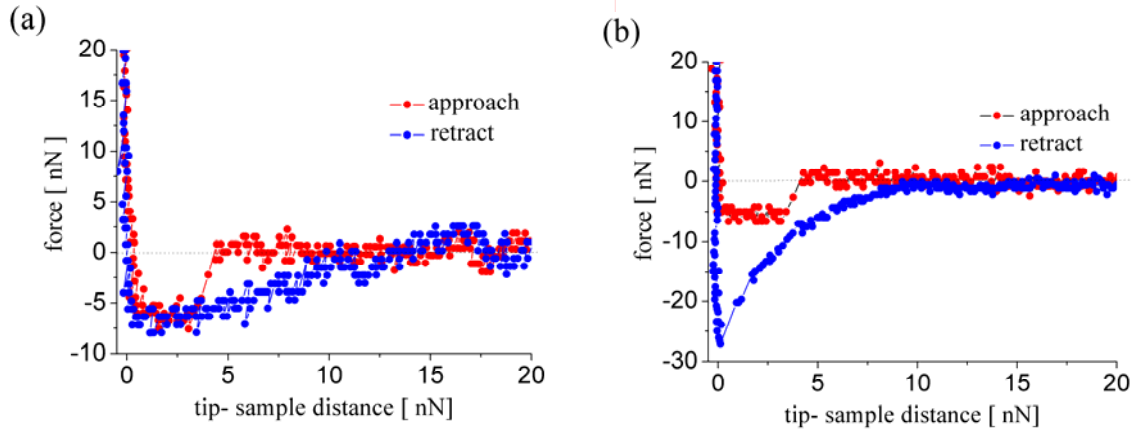


**Fig. 44** Typical force-distance curves measured on a silicon sample in air ( $\text{RH} = 33\%$ ,  $t = 24^\circ\text{C}$ ) with as-supplied (a) and plasma-cleaned (b) AFM probe (NSG11 provided by NT-MDT), respectively.

The silicon surfaces of the AFM tip and sample are covered by layers of adsorbed water. When the AFM tip comes in contact with the sample surface, the two layers of adsorbed water and contaminant molecules coalesce and form a bridge. Moreover, the water vapor in the ambient air condenses into the small gap formed by the AFM tip and sample surfaces and contributes to the bridge formation {Sirghi [134]}. The moment of bridge formation is registered as snap-in instability on the approach part of the force-distance curve (Fig. 44). The tip-sample distance at which the snap-in instability occurs indicates the maximum value of the thickness of the adsorbed layers of water and/or contaminant molecules on the AFM tip and sample surfaces. During the tip retraction, the AFM tip-sample interaction force decreased monotonically to zero for the either of cleaned or as-received AFM probes. The most common theoretical approach to the capillary condensation is based on the Kelvin equation [129]. The equation expresses the thermodynamic equilibrium between the pressure reduction in the liquid phase,  $\Delta p = (RT/V_m)\ln(p/p_s)$ , and the Laplace pressure, which is computed by the well-known Young-Laplace equation,

$$\Delta p = \sigma / r, \quad (20)$$

where  $r$  the meniscus total curvature radius. At equilibrium the total curvature radius of meniscus is Kelvin radius,  $r_k$ , which is defined by the Kelvin equation:

$$\frac{\sigma}{r_k} = \frac{RT}{V_m} \cdot \ln(p/p_s) \quad (21)$$

Here,  $R$  is the ideal gas constant,  $T$ , the absolute temperature,  $V_m$ , the molar volume of the liquid water,  $\sigma$ , the superficial tension of water ( $\sigma = 72 \text{ mN/m}$  at  $20^\circ\text{C}$ ),  $p$ , the pressure of the under

saturated vapor phase and,  $p_s$ , the water vapor saturation pressure. The Kelvin equation for water vapor in air at room temperature is [129]

$$r_k [\text{nm}] = \frac{0.54}{\ln(p/p_s)}. \quad (22)$$

For AFM measurements of adhesion force between hydrophilic AFM tip and sample in air, Sirghi et al [135] have reported a strong dependence of the capillary and superficial tension force on the AFM sample surface curvature. Significant changes in the capillary and superficial tension force were observed when the absolute value of sample curvature radius,  $|R_s|$ , was small enough to be comparable with the AFM tip curvature radius,  $R_t$ . In another paper Sirghi et al [123] reported a theoretical and experimental study on the dependence of the capillary and superficial tension force on the  $\text{TiO}_2$  surface wettability. The theoretical study neglected the sample curvature ( $|R_s| >> R_t$ ) and considered the interaction between a spherical tip and a flat sample through the capillary water bridge formed at tip-sample contact (Fig. 45). Considering the circular contour of radius  $r_2$  for the tip-water contact line of an axisymmetric meniscus formed between AFM tip and sample surfaces, the capillary and tension adhesive force,  $F_a$ , can be found as

$$F_a = -\frac{\pi \cdot r_2^2 \cdot \sigma}{r_k} + 2\pi \cdot r_2 \cdot \sigma \sin(\theta_t + \theta_{tw}), \quad (23)$$

where  $\theta_t$  and  $\theta_{tw}$  are the tip surface angles at the contact line and the tip wetting angle, respectively (Fig. 45). As it has been described in reference [135], under the approximations of thermodynamic equilibrium, spherical AFM tip and of symmetrical and spherical water meniscus formed at the tip-sample contact region, an analytical solution for the radius  $r_2$  can be found from a relation based on the geometry of the water meniscus

$$-r_1(\cos\theta_{tw} + \cos\theta_{sw}) + r_1 r_2 \left( \frac{\sin\theta_{tw}}{R_t} + \frac{\sin\theta_{sw}}{R_s} \right) = \frac{r_2^2}{2} \left( \frac{1}{R_t} + \frac{1}{R_s} \right) + d, \quad (24)$$

where the total curvature of the meniscus is:

$$\frac{1}{r_k} = \frac{1}{r_1} + \frac{1}{r_2}, \quad (25)$$

$r_1$ , the meniscus curvature radius in the vertical plan (see Fig. 45) and  $\theta_{sw}$ , the sample contact angle. By neglecting the distance between tip apex and the sample surface ( $d \approx 0$ ) and the sample curvature ( $1/R_s \approx 0$ ), the Eq.(28) is simplifies to:

$$-r_1(\cos\theta_{tw} + \cos\theta_{sw}) + r_1 r_2 \left( \frac{\sin\theta_{tw}}{R_t} \right) = \frac{r_2^2}{2} \left( \frac{1}{R_t} \right). \quad (26)$$

The Eqs (25) and (26) give the following analytical solution for the water meniscus radius  $r_2$ :

$$r_2 = r_k \cdot \left[ 1/2 + \sin \theta_{tw} + \sqrt{(\sin \theta_{tw} + 1/2)^2 - 2R_t \cdot (\cos \theta_{tw} + \cos \theta_{sw}) / r_k} \right] \quad (27)$$

Therefore, the dependence of the capillary and tension adhesive force  $F_a$  on the sample contact angle is described by the eqs (23) and (27). Since the approximations of spherical and symmetric water meniscus (Fig. 45) does work only for a limited range of sample contact angle values, values of the capillary and superficial tension forces were alternatively computed based on numerical integration of the Young-Laplace equation for a rotationally symmetric meniscus, which is [136]:

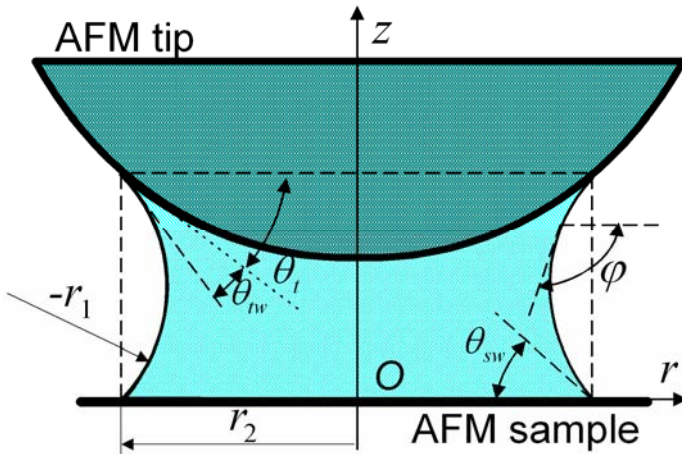


**Fig. 45** Schematic of the capillary water bridge formed between AFM tip and sample surfaces under approximations of spherical AFM tip, flat sample and of symmetrical and spherical water meniscus formed at the tip-sample contact region. Here,  $r_1$  and  $r_2$  are water-vapor interface principal radii,  $\theta_t$  the tip slope angle at tip-water contact line,  $\phi$  the meniscus surface slope angle and  $\theta_{tw}$  and  $\theta_{sw}$  are the tip and sample contact angles, respectively.

$$\begin{cases} \frac{dr}{d\varphi} = \frac{\cos(\varphi)}{1/r_k - \sin(\varphi)/r} \\ \frac{dz}{d\varphi} = \frac{-\sin(\varphi)}{1/r_k - \sin(\varphi)/r} \end{cases}. \quad (28)$$

The integration variable,  $\varphi$ , is the angle between axis  $Or$  and meniscus surface in the vertical plan,  $Orz$  (see Fig. 45). In this case, the radius  $r_2$  was found as the radius of the tip-meniscus contact line resulting from the numerical solution of Eq.(28) that satisfied simultaneously the boundary conditions  $\varphi = \pi - (\theta_t + \theta_{tw})$  at  $r = r_2$  and  $\varphi = \theta_{sw}$  at  $z = 0$ , where  $\theta_t$  is the tilt angle of the tip surface at the tip-meniscus contact line (Fig. 45). The numerical solution of the ordinary differential Eq. (28) was computed by a fourth-order Runge-Kutta routine with fixed step size.

Based on the assumptions and approximations described above, the dependence of the capillary and superficial tension force on the sample wettability (water contact angle) was found and this dependence is illustrated by Fig. 46. The solid line shows the dependence  $F_a(\theta_{sw})$  computed by Eq. (24) for the analytical solution found under the approximation of a spherical and symmetrical meniscus, while the points shows the dependence computed by the same equation for the axisymmetric meniscus shape resulted from numeric integration of Eq. (28). In these computations, values of 50 nm, 50% and  $60^\circ$  were taken for the tip radius, air humidity and tip surface contact angle, respectively. By increasing of the water contact angle of sample surface, the capillary and superficial tension adhesion force decreases monotonically.

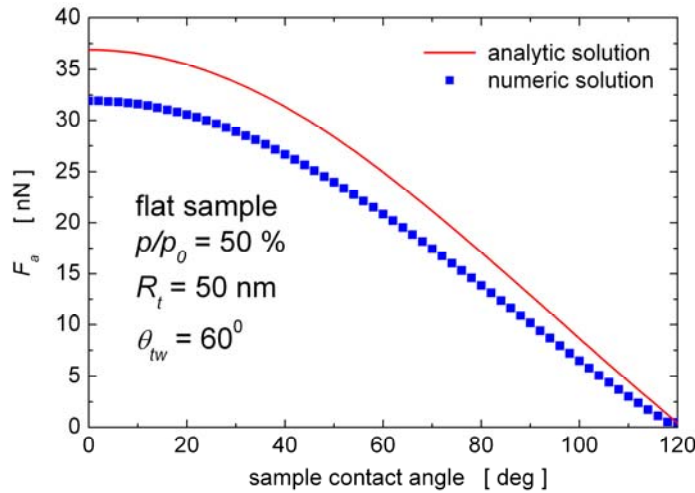


**Fig. 46 Dependence of the AFM tip-sample capillary and superficial tension force on water contact angle of the sample surface as resulted from analytical and numerical solutions for water meniscus. Values of 50 nm for AFM tip radius,  $R_t$ ,  $60^\circ$  for tip contact angle,  $\theta_{tw}$ , and 50% for air humidity were assumed.**

This monotonic dependence of the capillary and superficial tension adhesion force enables us to infer from the AFM measurements of adhesion force the information about the sample surface wettability at the microscopic level. The computation based on the analytical solution slightly overestimates the capillary and superficial tension force values due to the overestimation of the analytical solution for the radius  $r_2$  of the tip-meniscus contact line. Therefore, the effect of plasma treatment on the adhesion force can be understood as caused by the increase of the hydrophilicity of the AFM tip surface. Decrease of  $\theta_{tw}$  from about  $100^\circ$  to less than  $5^\circ$  results in a significant increase of meniscus size (value of  $r_2$ ) with a corresponding increase of capillary and superficial tension force of the meniscus.

During the pull-of experiments, the water menisci at AFM tip-sample contact stretch and break up at contact rupture. During meniscus elongation, the meniscus capillary and superficial tension force decreases monotonically reaching zero value at the meniscus breakup distance (Fig. 44). Sirghi et al [97] showed that the monotonic decrease of the meniscus attraction force by the increase of the tip-sample distance is related to the elongation and breakup of the liquid bridge formed by capillary condensation at the tip-sample contact. It was shown that the distance at which the liquid bridge breaks up is related to the volume of the bridge. Figure 47 shows numerical solutions of the meniscus surface during retraction of the AFM tip computed by Eq. (28) considering constant meniscus volume and tip and sample contact angle values. During the elongation, the meniscus curvature decreases. This means that the elongated meniscus is not in thermodynamic equilibrium with water vapor. Decrease of meniscus curvature results in a monotonic decrease of the meniscus attraction force. Figure 48 shows a comparison between experimentally values of meniscus force, the meniscus force computed by the model presented above, and the meniscus force computed considering the elongated meniscus in thermodynamic equilibrium with water vapor. The experiment showed that the elongated meniscus is not in thermodynamic equilibrium with water vapor and the breakup distance is much larger than  $2r_K$ .

The theoretical model of water meniscus elongation presented above foresees a meniscus breakup distance roughly equal to cubic root of meniscus volume. Interestingly, although the cleaning of the AFM probe resulted in an important increase of the adhesive force, the bridge breakup distance remained the same (about 10 nm).

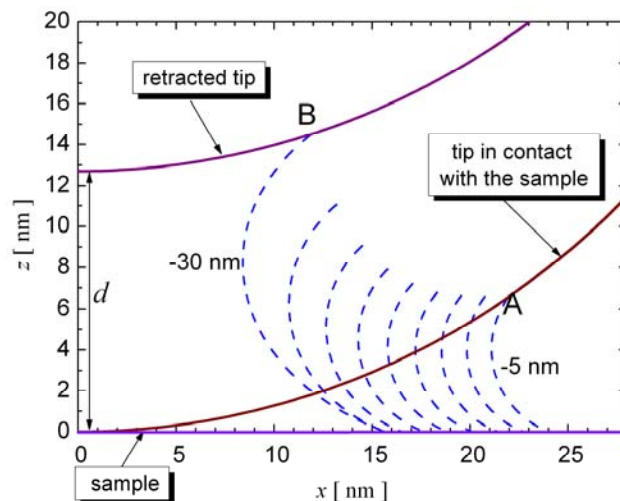


**Fig. 47 Illustration of a set of Young-Laplace solutions for stretching of a water meniscus during retraction of an AFM tip. Values  $R_t = 40$  nm, RH = 90 %,  $\theta_t = 20^\circ$  and  $\theta_s = 20^\circ$  were taken for this numeric simulation.**

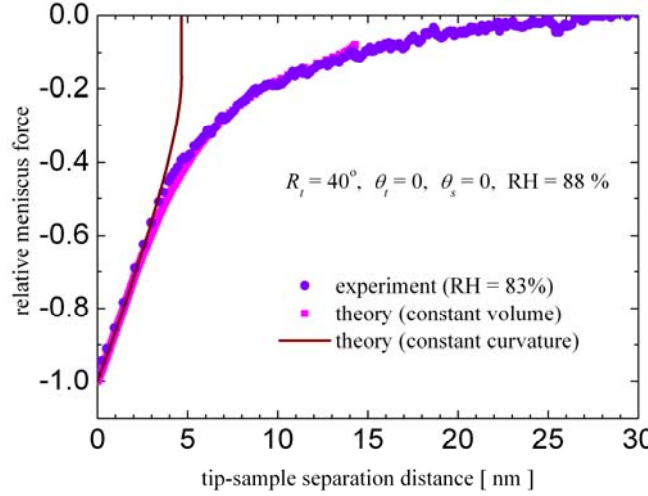


**Fig. 48 Comparison between an experimental force distance curve and the theoretically predicted force curves obtained for constant water meniscus volume and constant water meniscus curvature, respectively. The experimental force distance curve were acquired in 0.1 s by an AFM probe with a sharp silicon tip ( $R_t = 40 \text{ nm}$ ) on glass at RH = 83%. The numerical simulation was performed for RH = 88 %,  $\theta_t = 0^\circ$ ,  $\theta_s = 0^\circ$  and  $R_t = 40 \text{ nm}$ .**

This means that the volume of the liquid bridge formed at the tip-sample contact remained roughly the same. The increase of the capillary force created by a bridge of pure water in equilibrium with water vapor in air is commonly understood as an increase of the amount of water at the tip-sample contact, but it seems that this is not the case for AFM measurements of meniscus adhesive force with the as-received and cleaned AFM tip. Since the water bridge volume does not change much as result of the AFM probe cleaning, it is reasonable to consider that meniscus size does not change and the cleaning-induced increase of meniscus force is caused mainly by the increase (in absolute value) of pressure reduction in the liquid phase,  $\Delta p$ . This increase of  $\Delta p$  can be understood if some of the organic contaminant molecules on the AFM probe and sample surfaces are considered soluble in water. Thus, the bridge formed at the contact of the contaminated AFM tip and sample surfaces can be considered as formed by an aqueous solution of organic contaminants. According with the Raoult's low, the solute contaminants lower the saturation pressure of water vapor to  $p_s' < p_s$ , which means they lower (in absolute value)  $\Delta p$  to

$$\Delta p' = \frac{RT}{V_m} \ln(p / p_s'). \quad (29)$$

Another way to understand the decrease in the capillary pressure is to consider that the solute organic contaminant molecules create an osmotic pressure,  $p_{osm}$  in the liquid bridge that diminished the capillary pressure of the bridge,

$$\Delta p' = \Delta p - p_{osm}. \quad (30)$$

The presence of water soluble contaminants at the AFM tip-sample contact lowers the capillary pressure of the liquid bridge meniscus and the capillary component of the tip-sample adhesion force. Correspondingly, the removal of the organic contaminants from the AFM tip surface results in an increase of  $\Delta p$  and the capillary force.

In summary, plasma treatment of silicon AFM probes and samples remove efficiently the adsorbed hydrophobic contaminant molecules adsorbed on surfaces [93]. Thus, the plasma treatment cleans the silicon surfaces and renders them highly hydrophilic. The plasma treatment has a big impact on adhesion forces measured in water and ambient air. Treatment of silicon AFM probe and sample surfaces results in a strong increase of adhesion force in air and a cancelation of the adhesion force in deionized water [93]. The effect of adhesion force cancelation in deionized water is attributed to removal of layers of hydrophobic molecules on the two surfaces. Before treatment the hydrophobic molecules adsorbed on AFM tip and sample surfaces generate a bridge at the tip sample contact and a corresponding small adhesion force. Although this adhesion force is small (typically few hundreds picoNewtons), it can perturb AFM experiments as single molecule stretching where measured forces are typically few tenths of picoNewtons. On the other hand, plasma treatment of AFM probe and sample surfaces results in a strong increase of the adhesion force measured in air at moderate humidity values. This is happening because the adhesion force in air is generated mainly by the water bridge formed by capillary condensation of water vapor at the AFM tip-sample contact. The water bridge forms in a very short time at the AFM tip-sample contact through the capillary condensation of water vapor in the ambient air and generate a large adhesion force due to the action of capillary and superficial tension forces [134]. According to Sirghi et al [123] increase of AFM tip and sample surface hydrophilicity is associated to a larger water meniscus at the AFM tip-sample contact and, correspondingly, to a larger adhesion force. However, the meniscus breakup distance, which according to Sirghi et al [97] gives an indication on the size (volume) of the water meniscus, does not change as a result of plasma treatment. Then, the increase of the adhesion force was not attributed to the increase of the size of water meniscus, but to the effect of water soluble organic contaminant molecules on the capillary pressure. Solute contaminant molecules in the water meniscus diminish the capillary pressure and decrease the capillary force. Removing of contaminant molecules from AFM tip and sample surfaces results in an increase of the capillary pressure and to a corresponding increase of the capillary force.

#### **II.2.4 Sensing the chemical contrast by hydrophilic AFM probes**

Plasma cleaned and hydrophilized AFM probes were used recently by Sirghi et al [96] to study the chemical contrast of nanopatterns obtained by electron beam lithography (EBL) on

polyethylene glycol oxide (PEO) surface [137]. A thin layer of PEO (about 20 nm in thickness) was deposited on silicon substrate by PECVD in a reactor using a capacitively coupled r.f. discharge operating in pulsed mode (time-on = 10ms, and time-off = 100ms) at low nominal power (5 W) in pure Diethylene Glycol Dimethyl Ether (from Sigma-Aldrich) vapour at pressure of 15 mTorr. The substrate was placed on the passive electrode (electrically connected at the stainless steel reactor chamber, which was grounded) with the face towards the active electrode, which was positioned at 140 mm above the substrate. The electrodes consisted in stainless-steel disks with diameter of 140 mm. More details on the deposition system and characterization of the deposited PEO thin films are given in reference [138].

The EBL has been performed by a standard Scanning Electron Microscope (SEM) LEO 435VP equipped with an external beam controller system (Elphy Quantum, Raith GmbH). The acceleration voltage of the EB was set at 20 keV, while the intensity of the EB current was set to 0.200 nA.

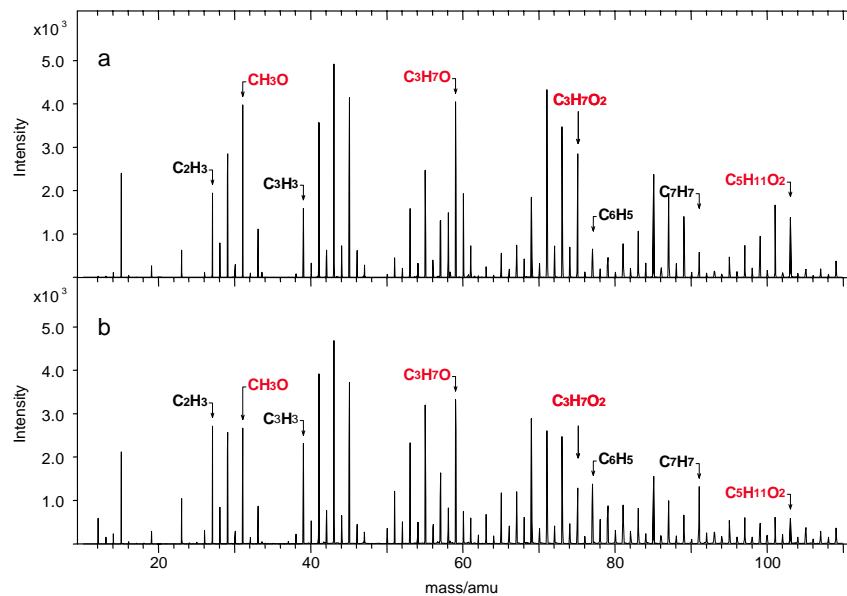


**Fig. 49 Comparison of normalized positive ToF-SIMS spectra acquired for untreated PEO surface(a), and EB irradiated (irradiation dose =  $6000 \mu\text{C}.\text{cm}^{-2}$ ) PEO surface (b). The peaks:  $\text{CH}_3\text{O}^+$ ,  $\text{C}_3\text{H}_7\text{O}^+$ ,  $\text{C}_3\text{H}_5\text{O}_2^+$ ,  $\text{C}_5\text{H}_{11}\text{O}_2^+$  have been considered for the oxygenated species, while the peaks:  $\text{C}_2\text{H}_3^+$ ,  $\text{C}_3\text{H}_3^+$ ,  $\text{C}_6\text{H}_5^+$ ,  $\text{C}_7\text{H}_7^+$  have been considered for hydrocarbons species.**

The EB irradiation dose (expressed as the electrical charge of the incident electrons per unit area of the sample surface) was controlled by varying of the irradiation time in 30 steps, from 200 to 6000  $\mu\text{C}.\text{cm}^{-2}$ . Patterns with array of 30 columns of spots, each column being irradiated with a different dose, were fabricated and studied by AFM. Alternatively, patterns of 30 traces, each trace being

irradiated with a different dose, were also fabricated and studied. The EB irradiation induces changes of the chemical and physical properties of the PEO surface. A direct proof of the induced changes of the surface chemical properties is provided by ToF-SIMS spectra acquired for EB irradiated and non-irradiated PEO surfaces, respectively. A comparison of these spectra is given in Fig. 49. The surface of the as-deposited PEO coating is characterized by the presence of oxygen peaks in the positive spectra (Fig. 47 a), such as  $\text{CH}_3\text{O}^+$  (31 amu,  $\text{CH}_3\text{-O-}$ ),  $\text{C}_3\text{H}_7\text{O}^+$  (59 amu,  $\text{CH}_3\text{-O-CH}_2\text{CH}_2\text{-}$ ),  $\text{C}_3\text{H}_5\text{O}_2^+$  (73 amu,  $\text{CH}_3\text{-O-CH}_2\text{CH}_2\text{-O-}$ ) and  $\text{C}_5\text{H}_{11}\text{O}_2^+$  (103 amu,  $\text{CH}_3\text{-O-CH}_2\text{CH}_2\text{-OCH}_2\text{CH}_2\text{-}$ ), which are representative of the ether bounds [139] contained in the coating, in agreement with the chemical structure of the starting monomer used for the plasma polymerization  $[(\text{CH}_3\text{-O-CH}_2\text{-CH}_2\text{-})_2\text{-O}]$ . The existence of hydrocarbons moieties can be also identified as the peaks  $\text{C}_2\text{H}_3^+$  (27amu),  $\text{C}_3\text{H}_3^+$  (39amu),  $\text{C}_6\text{H}_5^+$  (77 amu),  $\text{C}_7\text{H}_7^+$  (91 amu) in the spectrum. The ToF-SIMS spectrum of the EB irradiated PEO surface (Fig. 47 b) does not show new peaks to be assigned to generation of a complete new chemical structure on the PEO surface. However, the spectrum shows a decrease in the intensity of the characteristics oxygen peaks along with an increase in the intensity of the hydrocarbon peaks. A similar chemical change has been observed to be induced by the interaction of the PEO surface with Ar/H<sub>2</sub> microwave plasma [140]. The EB irradiation etches a thin layer (few nanometers) of material on the top of the PEO surface, as it is illustrated by the topography AFM image in the Fig. 50 a), where the sample height profile along a line of the irradiated dots shows etching of holes with a depth of about 4 nm. Therefore, the change of the surface chemical properties on the EB irradiated PEO may be related also to a possible inhomogeneity of the chemical structure of the PEO thin film. The decrease in the ether bond density on the EB irradiated PEO surface along with an increase of hydrocarbon bond density cause a decrease of surface energy resulting in a deterioration of hydrophilicity of PEO surface. These changes in the surface chemistry make the AFM measurements of friction and adhesive forces suitable for the characterization of chemical contrast of patterns fabricated by EBL on PEO. The chemical change induced by EB irradiation on the PEO surface has been also proved by a protein adsorption study [137]. Similar to the case of the plasma treatment, the EB irradiation diminishes the PEO-like character of the surface, rendering the surface protein adhesive. To probe the ability of EBL to produce protein repellent/adhesive nanopatterns on PEO surfaces, the patterned surfaces were incubated in bovine serum albumin (BSA) solution in PBS. The topography image (Fig. 50 b) of the patterned surface after incubation, water washing and drying indicates clearly the confinement of the proteins only into the irradiated areas keeping the non-irradiated surface free of proteins.

Atomic Force Microscopy imaging of friction force, adhesive force and phase lag in ambient air with a plasma-cleaned and hydrophilized AFM probe was used to characterize the chemical contrast induced by electron beam irradiation on PEO surface. The AFM measurements showed smaller phase lag and lower friction and adhesive forces on the EB irradiated PEO surface, as compared to the non-irradiated PEO surface. As the friction and adhesive forces depended on the AFM probe hydrophilicity and air humidity, the contrast in friction and adhesive forces is ascribed to different capillary condensation of ambient water vapour at the AFM tip contact with the EB irradiated and non-irradiated PEO surfaces, respectively. Before measurements, the probes were cleaned in discharge plasma for cleaning and hydrophilization of their surfaces. Details on AFM probe surface cleaning and characterization of the cleaned surface have been given in section II.2.1. The nanoscale patterns fabricated by EBL on PEO were characterized by AFM measurements in ambient air in contact and tapping modes. Figure 51 shows the topography (a), friction force (b), and phase-lag (c) images of a pattern with 30 columns of spots, each column of spots being irradiated with an increased (from left to right) EB dose. The friction force and topography images were acquired simultaneously in contact AFM mode with a plasma-cleaned AFM probe (CSG 11 from NT\_MDT) at low loading force (0.4 nN) and air relative humidity (RH) of 35%. The phase-lag image was obtained by scanning of the same pattern in tapping AFM mode with a plasma-cleaned AFM

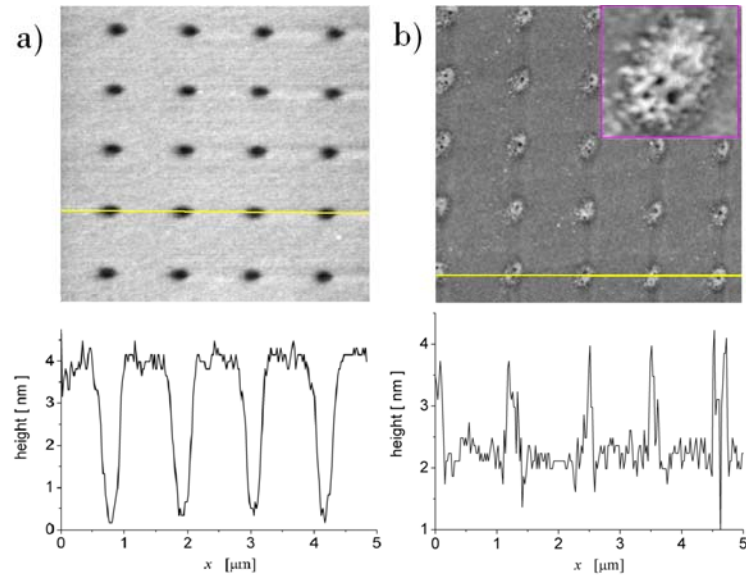


**Fig. 50 a)** Topography image ( $5\mu\text{m} \times 5\mu\text{m}$ ) of PEO surface patterned by EBL with column and rows of dots. The height scale is 5 nm. The profile of the surface height along the line indicated on the topography image is also shown. **b)** Topography image of the PEO patterned surface after it was incubated in BSA solution, washed and dried. The area and the height scale of the image are  $5\mu\text{m} \times 5\mu\text{m}$  and 5 nm, respectively. The inset shows a detailed image ( $0.5\mu\text{m} \times 0.5\mu\text{m}$ ) of the BSA deposited on the dot in the center of the large image. The height profile along the white line indicated on the topography image is also shown.

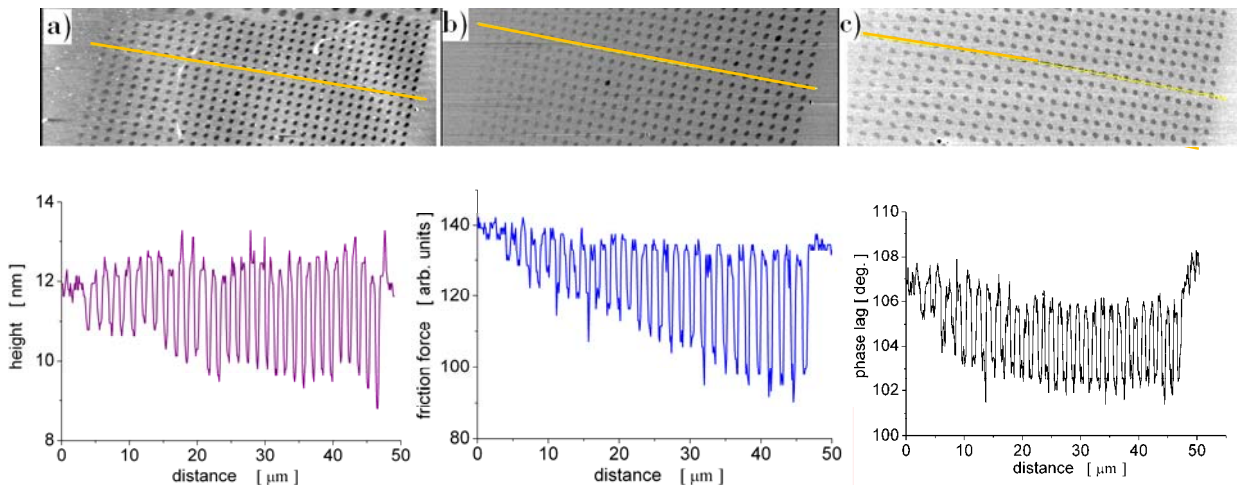


**Fig. 51** Topography (a) and friction force (b) images acquired simultaneously by scanning of a patterned PEO surface in contact AFM mode. The phase-lag image (c) obtained by scanning of the same patterned PEO surface in tapping mode AFM. The corresponding topography image, which was simultaneously acquired in tapping AFM mode, is not shown.

probe (NSG11 from NT-MDT) with a hard cantilever driven at resonant frequency (128.28 KHz) with the free amplitude of 64 nm and the set point amplitude of 32 nm. The EB irradiation of PEO surface results in an array of circular spots of about 300 nm in diameter. The topography image [Fig. 51 (a)] shows that the EB irradiation etches slightly the PEO surface, the etching depth varying according to the EB irradiation dose from 0.5 nm to 2.5 nm. The friction force image shows smaller friction force values on the EB irradiated PEO surface, as compared to the friction force values measured on the non irradiated PEO surface. The profile of the friction force variation along one line of spots, which is indicated by the yellow line depicted on the friction force image [Fig. 51 (b)], shows that the contrast in friction force increases linearly with the increase of the EB irradiation dose. The data concerning the friction force values measured on 10 spot lines of this pattern were statistically analysed and the dependence of the relative decrease of friction force versus the EB irradiation dose is plotted in Fig. 52 (a). The best linear fit of the data is also shown on the plot. The friction force on the EB irradiated PEO surface decreases linearly with the increase of the irradiation dose, the decrease reaching 40% of the friction force value recorded on the non irradiated PEO surface. Altering of the measurement conditions (scanning speed, feedback of the AFM system, change of the AFM probe, etc.) did not change the linear character of the friction force contrast dependence on the EB irradiation dose, while the slope of the linear dependence did change.

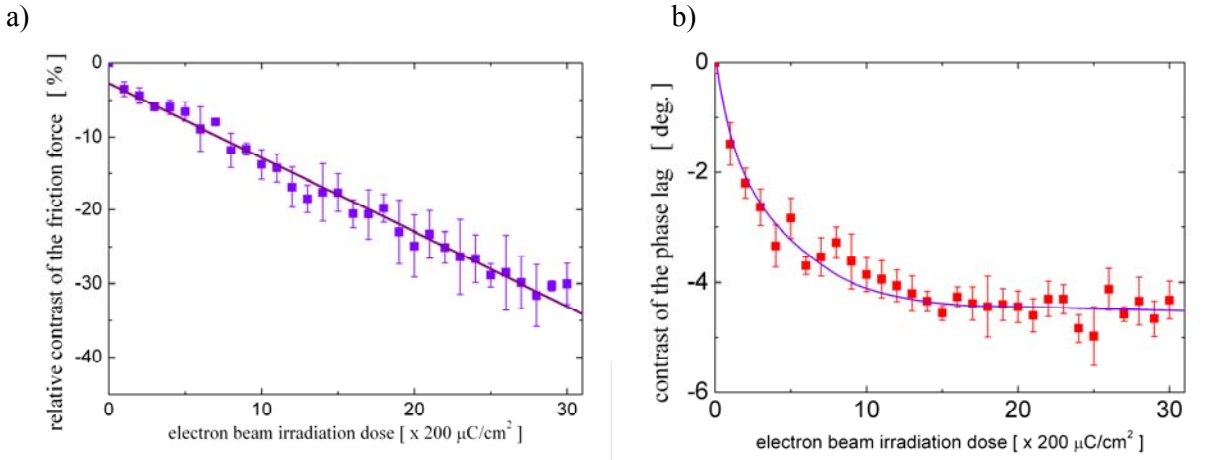


**Fig. 52** a) Dependence of the relative contrast of friction force on the EB irradiation dose. (b) Dependence of the contrast in the phase lag on the EB irradiation dose. The continuous line on this plot is drawn to guide the eye.

The phase-lag image obtained by tapping-mode AFM scanning of the same EBL pattern as that used for the friction force measurements was also analysed. The figure 51 (c) shows the phase-lag image and the phase-lag variation along one line of spots. The phase-lag values on the EB irradiated spots are smaller than those on the non-irradiated PEO surface. The data concerning the phase-lag values measured on 10 lines of spots of this pattern were statistically analysed and the dependence of the phase-lag contrast on the EB irradiation dose is plotted in Fig. 52 (b). Contrasting with the results of the friction force measurements, the phase lag shows a very nonlinear dependence on the EB irradiation dose. The variation of phase lag acquired in tapping AFM mode is usually interpreted in relation with the energy loss by the oscillating AFM probe during tapping of the sample surface [141]. While the contrast in phase lag reflects the differences in the surface chemistry, it has also a strong dependence on the tapping regime. Figure 53 shows the curves of the phase lag dependence on the AFM probe displacement measured on EB irradiated and non-irradiated PEO surfaces, respectively. Far from the sample surface, the AFM probe oscillates at resonance with a phase lag of 90°. While the AFM probe approach the sample surface (of which position is chosen as reference for the AFM probe displacement in the plots shown in Fig. 53), the phase lag decreases to values smaller than 90°, which correspond to the non-contact tapping regime. At certain value of the AFM displacement, which corresponds to the same value of the oscillating amplitude, the state of the AFM probe oscillation shifts suddenly to the intermittent-contact regime, when the phase lag is larger than 90°. This transition is indicated by the symbols A and B on Fig. 53. Characterization of the chemical contrast in the phase lag is performed in the intermittent-contact regime, when the AFM probe looses energy by strong interaction with the sample surface. The contrast in the phase lag between EB irradiated and non-irradiated PEO surfaces,  $\Delta\psi$ , at the set-

point amplitude of 32 nm (corresponding to the position of 32 nm on the AFM probe displacement) is illustrated in Fig. 53. The phase-lag contrast depended on the tapping ratio (the ratio of set-point amplitude on free-amplitude) and increasing of the set-point oscillation amplitude towards the free oscillation amplitude results in decrease of phase-lag contrast to zero and reversing of the contrast. An image showing reversal of the phase-lag contrast while the tapping ratio is increased is given in Fig. 54. For hard tapping (small set-point amplitude), the AFM probe works in the intermittent-contact regime. In this regime the AFM probe loses energy at each intermittent contact with the sample surface. Then, the contrast in the phase lag is associated with a smaller energy loss of the AFM probe while it taps the EB irradiated regions of the PEO surface than while it taps the non-irradiated PEO surface. This change in the energy loss may be caused by the EB irradiation effects of hardening and decrease hydrophilicity of the PEO surface. The nonlinearity of the phase lag dependence on the irradiation dose is related to the nonlinear character of oscillation movement of the AFM probe in tapping of the sample surface. The nonlinear character of the dependence of the phase-lag contrast on the EB irradiation dose did not changed by altering of the scanning parameters (tapping ratio, oscillating frequency, change of the AFM probe, etc). Since friction force measurements in contact AFM mode showed a linear dependence of the friction force on the irradiation dose, it is concluded that the friction force measurements are more suitable then phase lag measurements for the characterization of the chemical contrast of EBL patterns on the PEO surface.

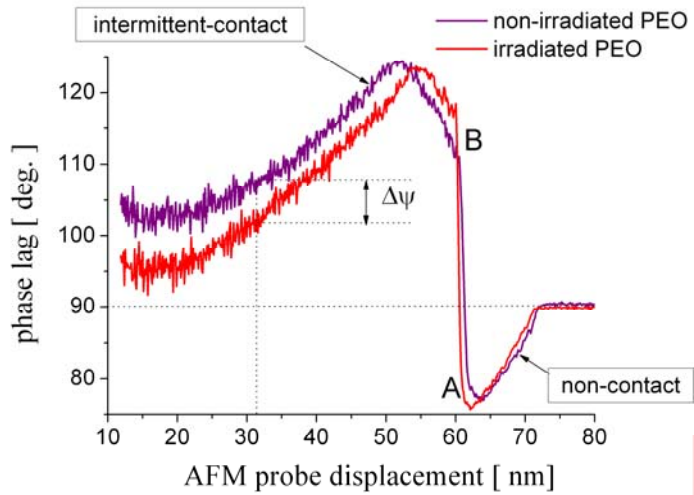


**Fig. 53** Curves of phase lag versus AFM probe (cantilever base) displacement measured on EB irradiated and on non-irradiated regions of the PEO surface. The height of the sample surface is taken as reference for the displacement in these plots. The symbol  $\Delta\psi$  represents the contrast in the phase lag for the set-point amplitude (32 nm). The symbols A and B indicate the transition between non-contact and intermittent contact regimes.

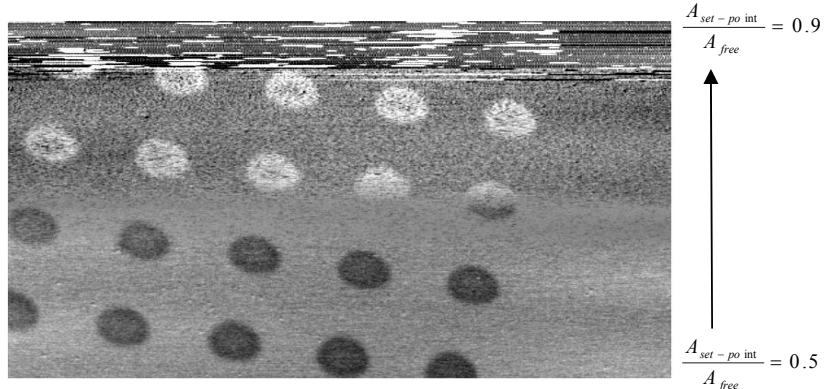


**Fig. 54** Image showing reversal of the contrast in the phase lag, which was observed during a gradual change of the tapping regime from hard tapping (bottom) to soft tapping (top). The intensity scale is 10 degrees. The image size is  $10\mu\text{m} \times 7\mu\text{m}$ . The tapping ratio was 0.5 at the bottom and 0.9 at the top of the image.

To elucidate the origin of friction contrast observed on the nanoscale patterns fabricated by EBL, force volume measurements were performed on an area of  $800\text{ nm} \times 800\text{ nm}$  of the sample surface comprising a single EB irradiated spot (maximum dose) surrounded by the non irradiated PEO surface. Figure 55 shows the topography (a) and friction (b) images along with the corresponding map of the adhesive force (c). These data were obtained in measurements performed with a plasma-cleaned AFM probe (CGS 11) in air at RH = 35%. The oval shape of this particular spot is due to poor stigmatisation correction of the EB during processing of this specific sample. As it was discussed before, the irradiated spot shows a reduction of about 2.5 nm in the PEO surface height and a friction force reduced to about half of the friction force value on the non irradiated surface. The corresponding adhesive force image was obtained by off-line processing of the force-displacement curves acquired on an array of  $20 \times 20$  points homogeneously distributed on the sample surface. The profile of the adhesion force values, which is also shown on Fig. 55 (c), was built with the adhesive force values determined by processing force-displacement curves acquired on 100 points homogeneously distributed along the line illustrated on the adhesion force map.

Figure 56 shows two typical force-displacement curves obtained on the non irradiated (a) and irradiated (b) PEO surfaces respectively. The adhesive force is determined as the minimum value of vertical force observed during retraction of the AFM tip (detachment force). The adhesive force on the irradiated PEO surface was with about 33% smaller than the adhesive force observed on non-irradiated surface.

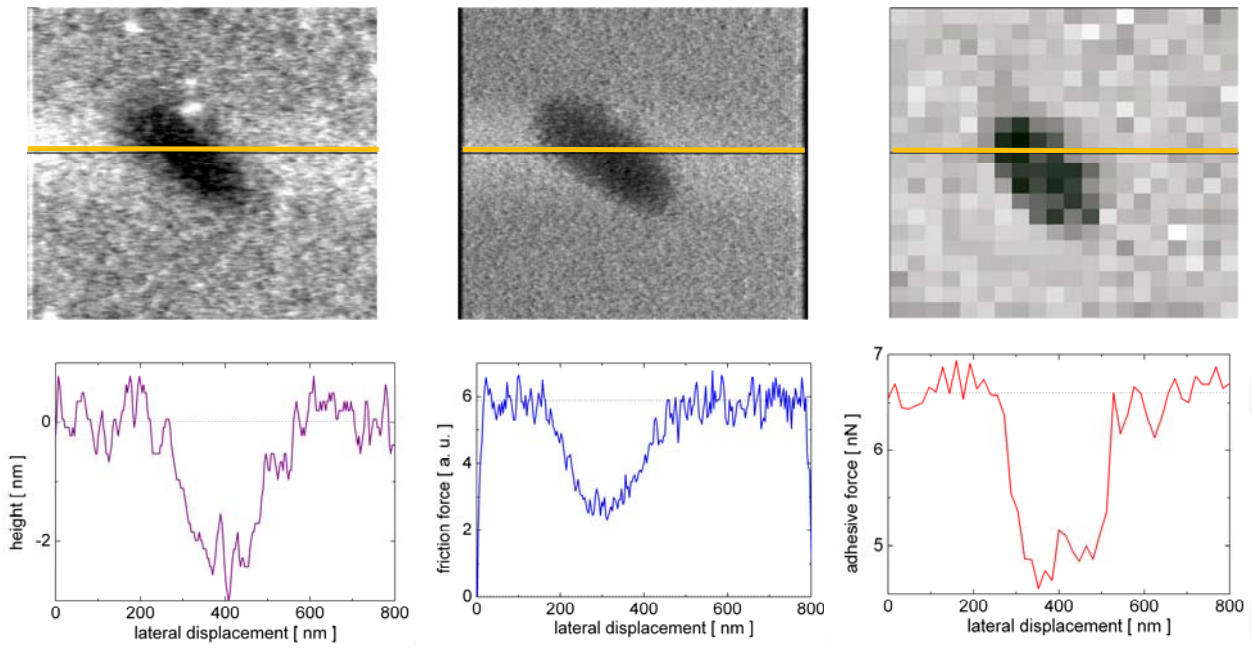


**Fig. 55 Topography (a) and friction force (b) images along with the corresponding map of the adhesion force (c) of a single EB irradiated spot (with maximum irradiation dose) on the PEO surface. Profiles of height, friction force, and adhesion force along the lines illustrated on the images are also shown.**

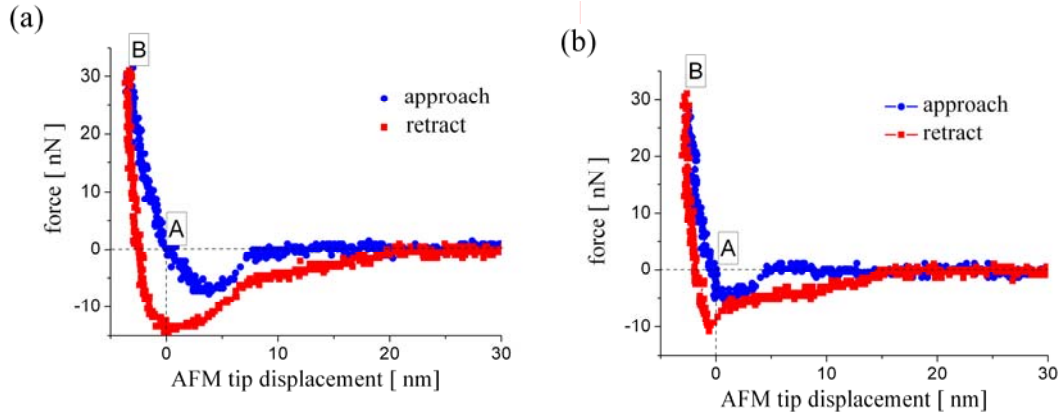


**Fig. 56 Typical curves of force versus the AFM tip displacement obtained with a hydrophilic AFM probe on the non-irradiated PEO surface (a) and on the EB irradiated PEO surface (b).**

The adhesive force in air is created mainly by the water bridge formed by capillary condensation at the contact between the AFM tip and sample surfaces. A relatively large adhesive force is expected at contact of hydrophilic surfaces in moderate humid air [123]. The force-distance curves shown in Fig. 56 were obtained with a plasma-cleaned AFM probe with a hard cantilever (spring constant of 5 N/m) in order to avoid jump-out instability caused by break up of the water bridge at the contact. While the AFM tip is retracted, the water bridge at the tip-sample contact

elongates and its capillary and superficial tension forces decrease until a tip-sample separation distance when the water meniscus breaks up. If the volume of the water meniscus is constant during the meniscus elongation, the meniscus break up distance is the cubic root of the water volume at the tip-sample contact [97]. Then, the meniscus break up distance is an indicator of the amount of water present at the tip-sample contact. Taken into account the force displacement curves presented in Fig. 56, it is determined that the water meniscus break up distance was about 22 nm on the non irradiated PEO surface and about 17 nm on the EB irradiated PEO surface. This is an indication of the effect of decrease of surface hydrophilicity caused by the EB irradiation, in agreement with the results of ToF-SIMS measurements.

The force-displacement curves presented in Fig. 56 shows also a stiffness difference between the EB irradiated and non-irradiated regions of the PEO film. The surface stiffness can be roughly estimated by the slope of the portion AB of the force versus displacement curve. After the AFM tip made contact with the sample surface, at the position A on the loading force-displacement plot presented in Fig. 56, the PEO film is squeezed between the AFM tip and the hard silicon substrate. The behaviour of the EB irradiated PEO film during this process is different from that of the non irradiated PEO film, at the same squeezing force a larger surface deformation being noticed for the non-irradiated PEO film. Therefore, the EB irradiation increases the stiffness of the PEO surface. This change can modify the tip-sample contact area contributing to the contrast in the adhesion and friction force images of the PEO patterned surface. However, because the friction force images were acquired at constant loading force that was too small to cause a noticeable difference in the contact area, we conclude that the main source of the friction contrast is the difference in the adhesion force.

To prove the role of water vapour condensation at the tip-sample contact for the chemical contrast of the friction force images, we compared the friction force images taken with the same AFM probe before and after cleaning and hydrophilization of its surface by discharge plasma (see the friction force images in Fig. 57). The water contact angle of the AFM probe surface, which was measured for a small sessile droplet of water on the base on the AFM probe, was about 90° before cleaning and less than 5° after the cleaning. The relative humidity of the ambient air during the measurements was 35%. A pattern consisting of 30 stripes, each of them being obtained by EB irradiation with a different dose (decreasing linearly from left to right), was used for this measurement. Plots of the friction force variation along one scanning line are also given in Fig. 57. It is noticed that cleaning and hydrophilization of the AFM probe surface increase the friction force

on the non-irradiated PEO surface of about three times. The contrast in friction force increased also of three times.

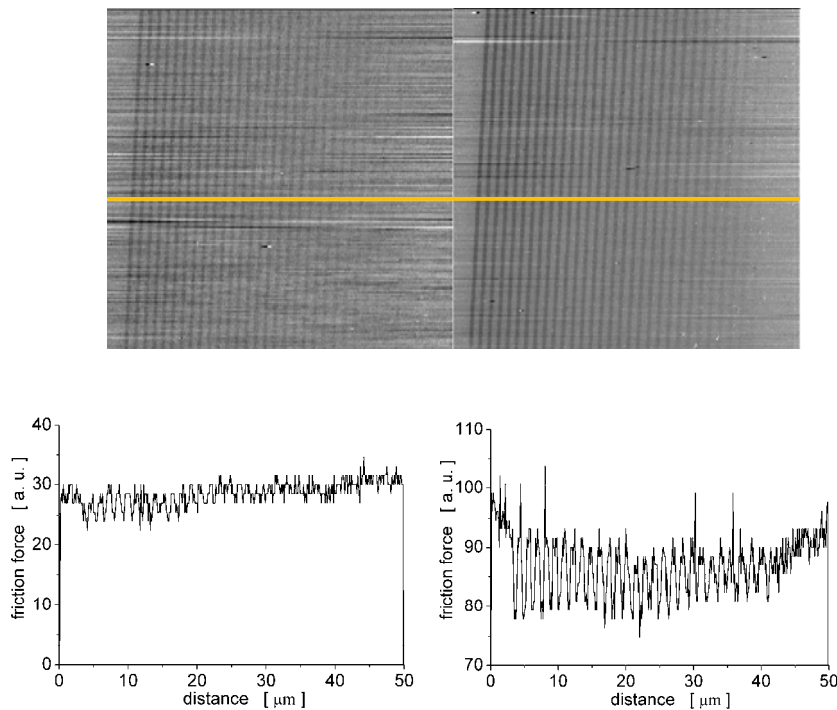


**Fig. 57 Enhancing the contrast in friction force by plasma cleaning and hydrophilization of the AFM tip.**  
Friction force images of a pattern with 30 stripes irradiated by EB with different dose (increasing from left to right) obtained with as received AFM probe (a) and with a plasma-treated AFM probe (b). Friction force profiles along scanning lines are shown in the lower part of figure.

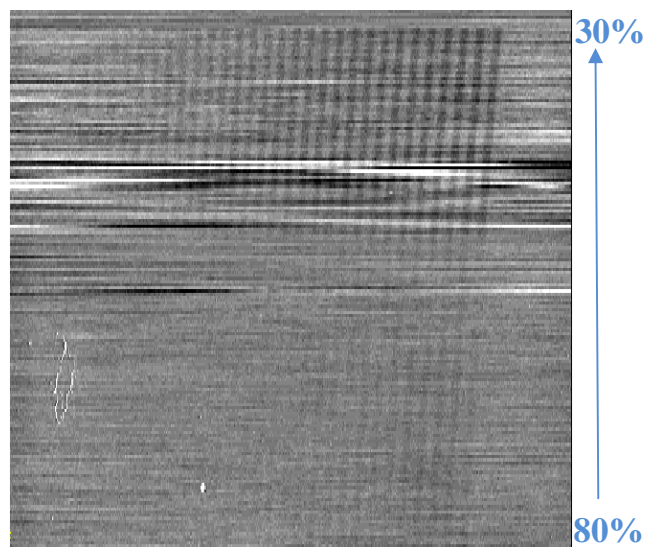


**Fig. 58 Prove of the air humidity effect.** Friction image acquired at constant loading force while the RH decreased from 80 % (bottom) to 30% (top)

An even more relevant proof of the role of capillary condensation of water at tip-sample contact on the contrast of the friction force image has been obtained by variation of the air humidity during friction force measurement. Figure 58 shows a friction force image that was acquired for the same pattern with stripes during variation of the air relative humidity from 80% (bottom of the image) to 35% (top of the image). In this measurement the loading force at the tip-sample contact was maintained constant to about 4 nN. In this experiment the AFM system was placed in a closed chamber filled with humid air ( $RH = 80\%$ ). In this humid air, the contrast in the friction force image vanished (bottom part of the friction force image). Force-displacement curves (not shown) acquired in humid air on the EB irradiated and non-irradiated PEO surface indicated disappearance of the contrast in the adhesion force and very large water menisci at the AFM tip-sample contact. At high humidity, the patterned PEO surface adsorbed a thick layer of water that cancelled out the contrast in friction and adhesive forces. Then, during scanning of the patterned surface, the air humidity was decreased by flowing relatively dried air ( $RH = 35\%$ ) through the AFM chamber. In the relatively dry air, the water on the sample surface evaporated restoring the contrast in the friction force image, as it is seen on the top of the friction force image shown in Fig. 58. This latter two experiments show that the friction force contrast is related to the differences in the hydrophilic property of the nanoscale patterns built by EBL on the PEO surface.

Sirghi et al [123, 124] have shown that mapping of adhesion and friction forces can be used for sensing of chemically different nanoscopic regions of  $TiO_2$  thin film surfaces. As it has been shown in section II.1.1, the  $TiO_2$  thin films obtained by radio frequency magnetron sputtering deposition (RFMSD) of a pure sintered  $TiO_2$  target in  $Ar/O_2$  mixture gases at pressure of 1 mTorr have a heterogeneous mesoscopic structure characterized by a mixture of rutile and amorphous phases. The difference in the photocatalytic activity of the two phases can be sensed by friction force microscopy and also by maps of force adhesion. In principle, the two phases show different wettability surfaces after being irradiated by UV light, which caused a difference in capillary water condensation at AFM tip contact with these surfaces. Large adhesive and friction forces values were measured on the super hydrophilic regions of amorphous phase, while small adhesive and friction force values were measured on the regions of low hydrophilicity of rutile phase. The relation between adhesive and friction forces and their dependence on the surface wettability were discussed in reference [142]. Figure 59 presents the typical force curve, i. e. tip-sample interaction force versus tip-sample distance,  $F(d)$ , during the approach and retract movements of the tip, obtained in AFM measurements for a silicon nitride tip (Olympus, OMCL-TR800PSA-1) and  $TiO_2$  thin film. On the approach curve, at a tip-sample distance around 5 nm, is observed a tip snap on instability

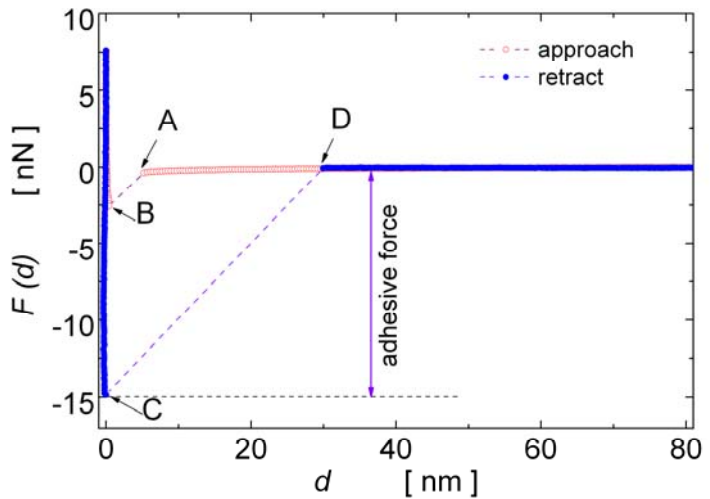


**Fig. 59** Typical force curve, i. e. tip-sample interaction force ( $F$ ) versus tip-sample distance ( $d$ ) for the approach and retract movements of the AFM tip, recorded for the interaction of a silicon nitride AFM tip with  $\text{TiO}_2$  thin film surface. The adhesive force is measured as the pull-off force required to detach the AFM tip from the sample surface.

(A-B). This instability is attributed to formation of the capillary water bridge between the AFM tip and sample surfaces. On the retract curve it is observed another discontinuity (C-D) consisting in tip snapping out of the sample surface. This instability is attributed to the break up of the capillary water bridge between the AFM tip and sample surface. The maximum attractive force on the retract force curve, which is measured just before the capillary water bridge breaks up, is taken as the tip-sample adhesive force that, neglecting other forces, can be attributed to capillary and surface tension forces of water meniscus formed by capillary condensation between AFM tip and sample surfaces. Because of the high dielectric constant of  $\text{TiO}_2$  [143] and the presence of water between the tip apex and sample surfaces at the moment when the water meniscus breaks, the force due to van der Walls interaction may be repulsive and negligible [144]. A computation of the Hamaker constant by the approximate formula of Israelachvili [129] for a configuration consisting of a spherical  $\text{Si}_3\text{N}_4$  tip ( $R_t = 50$  nm), water and a flat  $\text{TiO}_2$  sample gives a negative value of  $-4.9 \times 10^{-21}$  J for the Hamaker constant and a repulsive van der Waals force value of 1 nN at tip-sample distance of 0.2 nm. An analysis of a large number of force curve data taken for equally spaced points on the sample surface results, in addition to the sample surface topographic image, in an image showing the distribution of the adhesion force. Figures 60 show the topographic [(a) and (c)] and corresponding adhesion force [(b) and (d)] images obtained by AFM measurements in force curve mapping mode of a RFMSD  $\text{TiO}_2$  thin film (scanned area is  $600 \times 600$  nm $^2$ ) before and after UV light irradiation of the samples in atmospheric air. On the topographic images [Fig. 60 (a) and (c)] there are observed grains with 200 nm in diameter and 20 nm in height. However, the images with the adhesive force distribution on the film surfaces [Fig. 60 (b) and (d)] show very inhomogeneous

adhesive force distributions either before or after UV irradiation. However, the UV irradiation broadened the value range and increased the values of adhesive force values. Figure 60 (d) shows that the surface of some grain continued to present low adhesive force after UV irradiation, while the adhesion force increased in regions between grains. The effect of sample surface curvature [135] can not explain the broad distributions of adhesive force values.

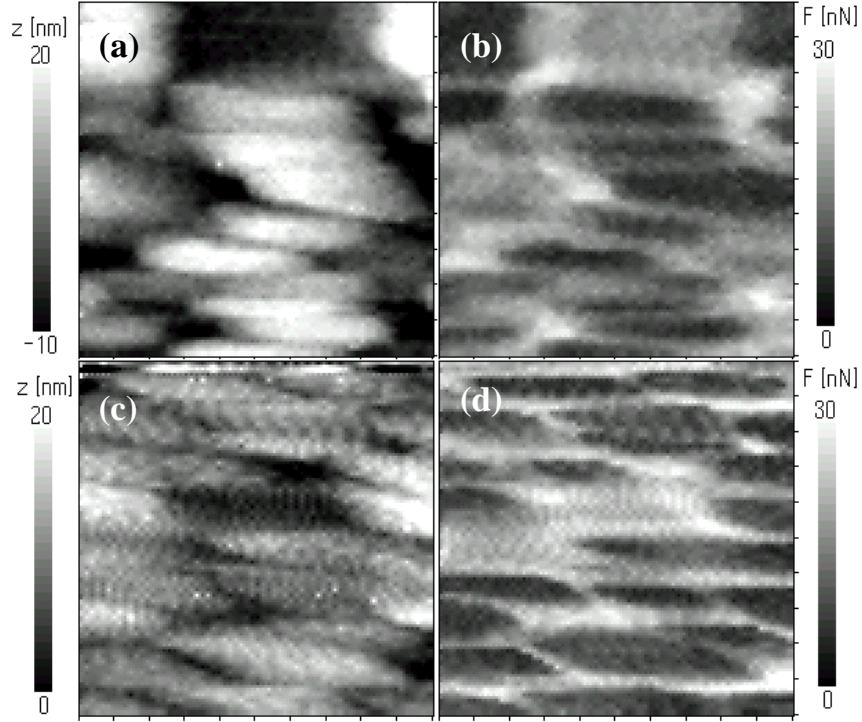


**Fig. 60** Images of the topography and corresponding adhesive force maps on the  $\text{TiO}_2$  thin film surface before and after UV light irradiation. Figures (a) and (c) display topographic images before and after UV light irradiation, respectively, and figure (b) and (d) are their corresponding images of adhesive force.

The sample surface curvature values were much smaller than the AFM tip curvature, which means that the tip-sample adhesive force values could be affected by the sample surface curvature in a limit of less than 10% from the force value corresponding to a macroscopically flat sample. Therefore, the wide distributions of adhesive force on the UV irradiated  $\text{TiO}_2$  surface were attributed to heterogeneous crystalline structure of these films. The results of adhesive force mapping experiments were confirmed also by friction force images obtained in FFM. Figure 61 shows topography (upper left) and friction force (upper right) images obtained by AFM scanning of UV irradiated  $\text{TiO}_2$  thin film surface. The lower part of the figure shows the profiles of sample height and friction force along one scanning line AB. The friction force image shows regions of low friction that corresponds to some grains on film surface, which confirms the results of adhesive force mapping measurements.

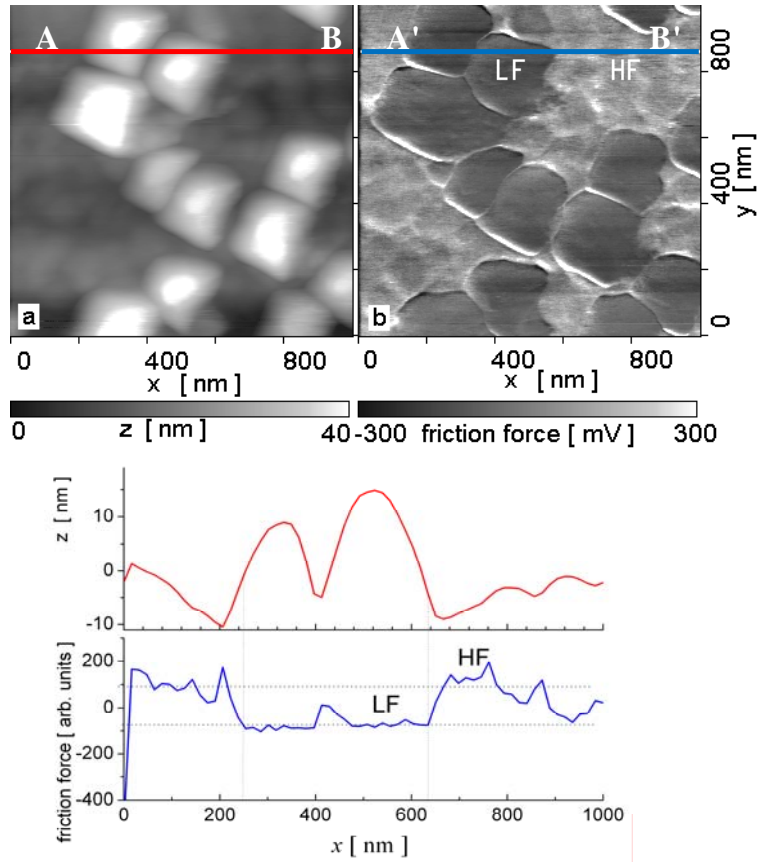


**Fig. 61** Images of the surface topography (upper left) and friction force distribution (upper right) on the TiO<sub>2</sub> thin film surface after UV light irradiation. The lower part of figure presents profiles of sample height (red) and friction force (blue) along a scanning line AB.

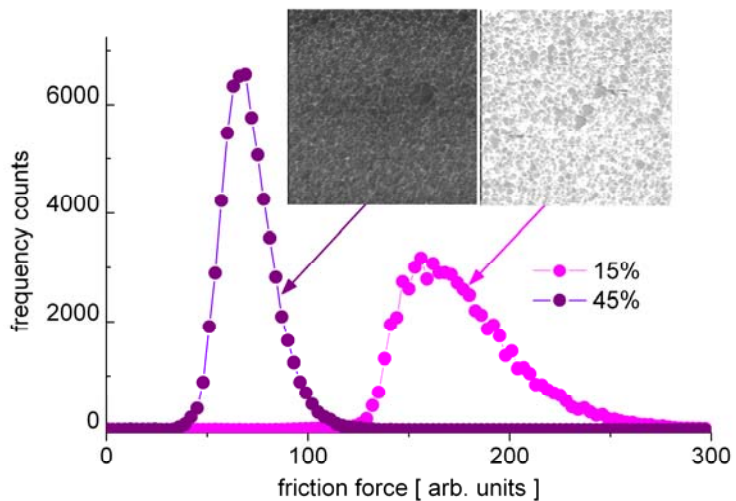


**Fig. 62** The histograms of the frequency counts of the friction force values on an area of  $2000 \times 2000 \text{ nm}^2$  of the super hydrophilic surface of sample c (after it was irradiated by UV light) at two values of RH. The inset shows the friction force images at RH = 15% (left part) and RH = 45% (right part).

The strong effect of the capillary wetting on friction force of the AFM tip-sample contact was proved by FFM measurements in air at different humidity values on the super hydrophilic surface of the UV-light irradiated surface of a TiO<sub>2</sub> thin film obtained by RFMSD in Ar/O<sub>2</sub> at 10 mTorr. This particular film showed a highly photocatalytic homogeneous surface corresponding to amorphous TiO<sub>2</sub> structure with short range order of anatase type. The measurements were performed by a commercial AFM (Seiko Instruments Inc., SPI 3800) with a soft Si<sub>3</sub>N<sub>4</sub> cantilever ( $k = 0.03 \text{ N/m}$ ) and a sharpen tip (nominal curvature radius of 10 nm). The external normal load applied on the tip-sample contact was kept to a value under 0.1 nN, which was much lower than the estimated loading force generated by the capillary meniscus (6 nN). The low value of RH was achieved by flowing dry nitrogen through the environmental chamber housing the AFM. The histograms representing the frequency counts of the friction force values measured over an area of 2000×2000 nm<sup>2</sup> of the sample and an inset showing the images of the friction force on the sample surface at RH = 15% (left) and RH = 45% (right) are presented in the Fig. 62. The histograms show that the friction force values decreased more than two times by the decrease of RH from 45% to 15%. This drastic decrease of the friction force is explained by the decrease of the size of water meniscus formed at the tip-sample contact. Also, one notices that the distribution of the frequency counts of the friction force values is broader at RH = 45% than at the RH = 15%, which is also an evidence of the effect of the tip-sample contact wetting on the friction force. When the AFM tip is dragged along the sample surface under a low external load, variations of the sample topography may result in variations of the shape and size of the water meniscus at the tip-sample contact, which induces variations of the friction force that broaden the friction force value distribution.

In summary, plasma cleaned and hydrophilized AFM tips are suitable for sensing chemically different regions on a sample surface by either friction force microscopy or adhesive force mapping measurements in ambient air at moderate values of humidity. Increase of the humidity towards saturation may result in loss of the chemical contrast. This is also happening when the measurements are done in very dry atmosphere (very low humidity). The chemical contrast in friction and adhesion forces is attributed to the effect of capillary condensation of water vapor at the contact of AFM tip and sample. The water meniscus formed by capillary condensation generates a large contact adhesive force due to capillary and superficial tension forces of the meniscus. More hydrophilic regions on a sample surface are characterized by larger water menisci and adhesive force values as compared to less hydrophilic (or hydrophobic) regions. This principle has been used to distinguish regions of different photocatalytic activity of TiO<sub>2</sub> thin films deposited by radio frequency magnetron sputtering deposition. Surface of these films becomes superhydrophilic by UV irradiation due to decomposition of adsorbed water and hydrophobic

contaminant molecules. However, thin films deposited at low values of Ar/O<sub>2</sub> gas mixture (1 mTorr) showed a heterogeneous surface with regions of less photocatalytic activity (attributed to rutile nanocrystals) surrounded by regions of high photocatalytic activity (attributed to amorphous structure with short range crystalline order of anatase type). Such regions were discriminated by AFM measurements in moderate humid air of friction and adhesion forces. Large values of friction and adhesion forces were observed on highly photocatalytic regions (superhydrophilic after UV irradiation) while smaller force values were observed on less photocatalytic (less hydrophilic) regions. Plasma treated AFM tips were used also in study of chemical contrast shown by nanopatterns obtained by electron beam lithography of polyethylene glycol oxide surface obtained by PECVD. The electron beam irradiated regions of PEO surface showed a larger stiffness and were less hydrophilic as compared to the non irradiated PEO surface. Therefore, AFM measurements of friction and adhesion forces in air showed a chemical contrast of the patterns, the friction and adhesion forces being larger on non irradiated PEO surface as compared to the electron beam irradiated PEO surface. It has been shown that the contrast in friction force increased linearly with the electron beam irradiation dose. The phase lag images acquired in AFM tapping (intermittent contact) mode can be also used for characterization of chemical contrast created by electron beam lithography on PEO surface. However, in this case the contrast did not show a linear dependence on the electron beam irradiation dose. These studies have shown that the AFM tip hydrophilicity and air humidity are important factors in sensing of chemical contrast on a sample surface.

## **II.2.5. Control of adhesion in AFM indentation experiments**

Control of adhesion forces between AFM tips and sample surfaces may play an important in AFM indentation experiments. With the advent of the atomic force microscopy (AFM), many of the indentation experiments moved towards very small scale. Nanoscale indenters (tips of AFM probes) are used in indentation experiments on thin films [145, 146] and small objects as bacteria [147], living cells [148], *etc*, with the goal of assessing their mechanical properties. The decrease in the indenter and sample dimensions goes along with decrease in indentation force and increase of the role of contact adhesion in the indentation mechanism [149, [150]. The adhesion force can have values comparable to the elastic force values in nanoindentation experiments on biological samples and polymer films. One important application of atomic force microscopy in study of living cell is sensing of cell mechanical properties, i.e. elasticity and viscosity by nanoscopic indentation experiments. In a recent paper, Sirghi et al [98] have shown that AFM indentations of living cells are strongly affected by nonspecific adhesion forces between cell membrane and AFM tip. By

covering of the AFM tips with a cell repellent polyethylene glycol oxide layer, the adhesion force is reduced to negligible values, which make the analysis of force versus distance data much easier {Sirghi and Rossi [99]}.

In spite of the important role of adhesion in nanoscale indentation experiments, the assessment of mechanical properties is often based on the Oliver and Pharr analysis [151] of the indentation force-displacement data, an analysis that ignores the indenter-sample adhesive force. Sirghi and Rossi [99] (see the selected paper P8) proposed an extension of Oliver and Pharr analysis, extension that accounts for the effect of indenter-sample adhesion force on the unloading force-displacement curves obtained in nanoscale indentation experiments. The proposed analysis is developed for the conical indenter-sample geometry, which is the likely geometry of sharpened tips of AFM probes [see Fig. 63 (a)], but it can be easily applied to other axis-symmetrical geometries. Besides determination of the Young's modulus of the sample, the proposed analysis allows for determination of indenter-sample work of adhesion. The analysis was applied on the unloading force-displacement data obtained in AFM indentation experiments on poly(dimethylsiloxane), PDMS, with sharp silicon conical tips.

Assessment of elasticity at nanoscale is usually based on Sneddon [152] solutions of elastic indentation of half space samples by rigid indenters of arbitrary axis-symmetric profiles. According to Sneddon, the stiffness of the axis-symmetric elastic contact,  $S = \frac{dP}{dh}$ , is

$$S = 2 \cdot E^* \cdot r_c, \quad (31)$$

where  $P$  is the loading force,  $h$ , the indentation depth,  $r_c$ , the radius of indenter-sample contact line [see Fig. 63 b)], and  $E^*$ , the reduced elastic modulus of the indenter-sample system, which is

$$\frac{1}{E^*} = \frac{1 - \nu_i^2}{E_i} + \frac{1 - \nu_s^2}{E_s}. \quad (32)$$

Here,  $E_i$  and  $\nu_i$  are the Young's modulus and Poisson ratio of the indenter, and  $E_s$  and  $\nu_s$  are the same parameters for the sample. When samples are much softer than the indenters ( $E_s \ll E_i$ ):

$$E^* \cong \frac{E_s}{1 - \nu_s^2}. \quad (33)$$

Pharr *et al.* [153] showed that Sneddon equation [Eq (31)] is generally applicable to any axis-symmetric geometry of the indenter-sample contact. Sneddon equation can be used for determination of sample elasticity provided  $r_c$  is accurately measured.

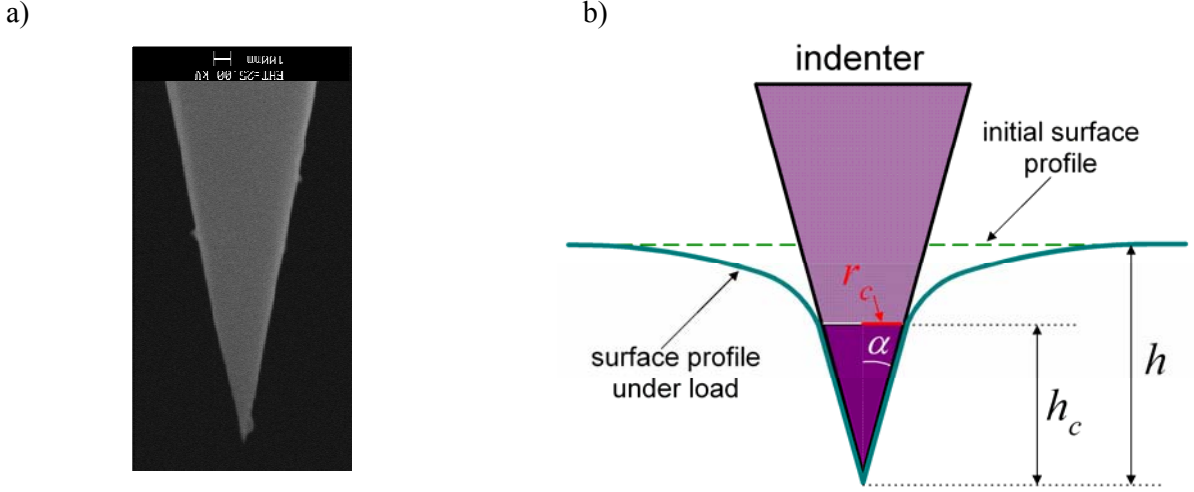


**Fig. 63** SEM image of the AFM tips used in indentation experiments (a). A schematic representation of a conic tip indenting a half-space sample (b). Displacement of the tip ( $h$ ), elastic displacement of sample surface at the contact line with the indenter ( $h_e$ ), contact depth ( $h_c$ ), contact radius ( $r_c$ ) and cone angle ( $\alpha$ ) of the indenter are shown.

In some indentation experiments,  $r_c$  at maximum load can be determined by analysis of the image of the remnant plastic imprint on the sample surface [154, 155]. However, for most of the indentation experiments  $r_c$  is not a directly measurable parameter. If the equation that defines the geometry of the axis-symmetrical indenter,  $r = f_i(h)$ , is known,  $r_c$  is determined by the contact depth,  $h_c$  [see Fig. 63 b) for illustration of indentation parameters]. However,  $h_c$  is also not a directly measurable parameter. For the sink-in deformation of the sample surface,  $h_c$  is smaller than the total indenter displacement,  $h$ , with the elastic displacement of the sample surface at the contact line with the indenter,  $h_e$  [Fig. 63 b)].

$$h_c = h - h_e \quad (34)$$

Doerner and Nix [156] proposed a simple method to evaluate  $h_c$  at maximum load,  $P_m$ . They considered that at the beginning of the unloading process  $r_c$  is constant (approximation of a flat punch), which allows to approximate  $h_e$  at maximum load as  $P/S$ . According to their analysis, the contact depth at beginning of the unloading process is

$$(h_c)_m = h_m - (P/S)_m, \quad (35)$$

where the index  $m$  signifies that the parameters are taken at maximum load. Oliver and Pharr [151] improved the Doerner and Nix method by showing that  $S$  and  $r_c$  are changing continuously during unloading, in which case the process is described by a nonlinear force-displacement dependence of general form:

$$P(h) = a \cdot (h - h_f)^n, \quad (36)$$

where  $h_f$  is the depth of the remnant indenter imprint on the sample surface. The parameter  $n$  is 1.5, 2, and 1 for sphere and paraboloid of revolution, cone, and flat cylinder indenter-sample contact geometries, respectively. It should be mentioned that the indenter-sample contact geometry may differ from the indenter geometry because of the remnant imprint on the sample surface. In deriving the Eq. 36, it is considered that  $P$  equilibrates solely the elastic force resulting from the elastic deformation of a half-space sample surface. Sirghi and Rossi followed the Oliver and Pharr approach by considering Sneddon's solutions [152] for the shape of the sample surface outside the contact area. Therefore,  $h_e$  was considered to be determined as:

$$h_e = \varepsilon \cdot h, \quad (37)$$

where  $\varepsilon = 1-2/\pi$ , 1/2, and 1, for conical, spherical, and flat cylinder indenter-sample contact geometries, respectively. Considering the Eqs. (34) and (37), it follows that

$$h_c = (1 - \varepsilon) \cdot h. \quad (38)$$

For the conical indenter-sample contact geometry,  $h_c$  determines the contact radius as

$$r_c = h_c \cdot \tan \alpha, \quad (39)$$

and  $r_c$  is determined by geometry of indenter as:

$$r_c(h) = h \cdot (1 - \varepsilon) \cdot \tan \alpha, \quad (40)$$

where  $\alpha$  is the cone angle. The model was further improved by Sirghi and Rossi, which in reference [157] considered that the adhesion affected the contact radius and proposed the following equation for  $r_c$ :

$$r_c = r_a + h \cdot (1 - \varepsilon) \cdot \tan \alpha, \quad (41)$$

where  $r_a$  is the finite value of  $r_c$  at  $h = 0$ . The value of  $r_a$  was found to be dependent on the indenter apex radius, sample stiffness, and contact adhesion strength. Figure 64 shows the dependence  $r_c(h)$  found experimentally for indentation of polydimethylsiloxane (PDMS) samples (slabs with the thickness of about 2mm) obtained by curing molds of polymer:curing agent (Sylgard from Dow-Corning Co.) for 16 hours at 60°C. The PDMS material was chosen because of its low viscosity at room temperature and good adhesion to the silicon surface (measurements of macroscopic work of adhesion between PDMS samples and a silicon by the detachment length method determined a value of  $0.11 \pm 0.015$  N/m, while tensile experiments determined values of  $1.75 \pm 0.29$  MPa for the Young modulus).

The external loading force applied to the indenter during unloading process,  $P$ , is considered as a sum of the elastic force of the sample,  $F_e$ , and adhesive force,  $F_a$ , at the indenter-sample contact:

$$P = F_e + F_a, \quad (42)$$

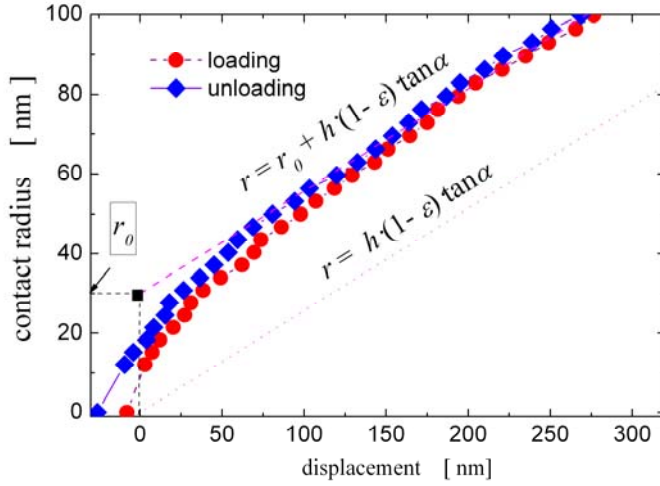


**Fig. 64 Plots of contact radius versus AFM tip displacement as they were measured in indentation of a PDMS sample**

Using of the Sneddon equation for the elastic force, the value of  $\varepsilon$ , and Eq. (40) for the conical indenter-sample contact geometry, the following equation is found for elastic stiffness of the indenter-sample contact:

$$\frac{dF_e}{dh} = (4E^*/\pi) \cdot \tan \alpha \cdot h. \quad (43)$$

The integral of Eq. (43) gives the Oliver and Pharr dependence of the unloading (pure elastic) force on indentation height for the conical tip-sample geometry:

$$F_e(h) = (2E^*/\pi) \cdot \tan \alpha \cdot h^2. \quad (44)$$

If  $h_f \neq 0$ , the Eq. (44) becomes

$$F_e(h) = (2E^*/\pi) \cdot \tan \alpha \cdot (h - h_f)^2 \quad (45)$$

This equation describes the dependence of indentation force on indentation depth for the elastic unloading process in indentations performed with conical indenters with negligible adhesion to the sample surface.

When the indenter-sample adhesion is not negligible, a term describing adhesive force variation during the unloading process has to be added to the right-hand member of Eq. (36). To determine  $F_a$ , the energy of adhesion at the indenter-sample contact is considered as:

$$W_a = -\gamma_a \cdot A_c, \quad (46)$$

where  $\gamma_a$  is the thermodynamic work of adhesion and  $A_c$ , the indenter-sample contact area.

For the conical geometry,  $A_c$  is

$$A_c = \frac{\pi \cdot \tan \alpha}{\cos \alpha} \cdot h_c^2. \quad (47)$$

Use of Eqs. (38) and (47) in Eq. (50) gives the following expression for the contact adhesion energy:

$$W_a = -\frac{\gamma_a \cdot 4 \tan \alpha}{\pi \cdot \cos \alpha} \cdot h^2. \quad (48)$$

Therefore, the adhesive force is

$$F_a = -\frac{\gamma_a \cdot 8 \tan \alpha}{\pi \cdot \cos \alpha} \cdot h \quad (49)$$

If  $h_f \neq 0$  the Eq. (17) has to be written as:

$$F_a = -\frac{\gamma_a \cdot 8 \tan \alpha}{\pi \cdot \cos \alpha} \cdot (h - h_f). \quad (50)$$

According to Eqs (42), (45), and (50), the external force acting during unloading the contact is:

$$P(h) = \frac{2E^* \cdot \tan \alpha}{\pi} \cdot (h - h_f)^2 - \frac{\gamma_a \cdot 8 \cdot \tan \alpha}{\pi \cdot \cos \alpha} \cdot (h - h_f). \quad (51)$$

Therefore, for a conical indenter the adhesive force modifies the Oliver and Pharr unloading force-displacement equation to

$$P(h) = a \cdot (h - h_f)^2 - b \cdot (h - h_f), \quad (52)$$

with

$$a = \frac{2E \cdot \tan \alpha}{(1 - \nu^2) \cdot \pi} \quad (53a)$$

and

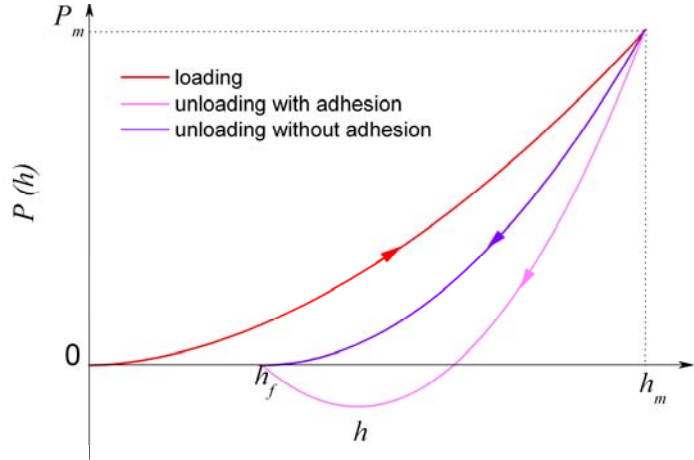
$$b = \frac{8 \cdot \gamma_a \cdot \tan \alpha}{\pi \cdot \cos \alpha}. \quad (53b)$$

Figure 65 illustrates the difference between the two dependences. The effects of adhesion force are: 1) occurrence of negative values of  $P$  on the unloading part of the force-displacement curve; 2) decrease of the apparent contact stiffness, and; 3) increase of the indentation depth. During loading, the adhesion force contributes to the work of indentation and this is why the indentation depth is higher when adhesion force at indenter-sample contact is noticeably large. On the other hand, adhesion force opposes to the unloading process. Considering the force-displacement dependences described by the Eqs (36) and (52), it follows that apparent stiffness is  $S = 2a \cdot (h - h_f)$  for the non adhesive contact, and  $S' = 2a \cdot (h - h_f) - b$ , for the adhesive contact. Therefore,  $S'$  is smaller than  $S$  and can have negative values at the end of the unloading process. The unloading force-displacement curve for the adhesive contact shows a minimum at a distance,  $h_0$ , which is determined by the condition  $S' = 0$ . Taken into account the expressions of  $a$  and  $b$  [Eqs (56)], it follows that

$$h_0 - h_f = \frac{2\gamma \cdot (1-\nu^2)}{E \cdot \cos \alpha}. \quad (54)$$

For stiff and non adhesive samples (large values of  $E$  and small values of  $\gamma$ ),  $h_0 - h_f \approx 0$ , which indicate a negligible effect of adhesion on the indentation mechanism. On the other hand, important values of  $h_0 - h_f$  can be observed for soft and adhesive samples (small values of  $E$  and large values of  $\gamma$ ), in which cases the effect of adhesion on the indentation mechanism can not be neglected.

If the effect of adhesion on the indenter-sample contact area is considered [i.e.  $r_c$  depends on  $h$  according the Eq. (41)], the fallowing dependence of indentation force on the indenter displacement is found {Sirghi and Rossi [157]}:



**Fig. 65** Representation of typical force-distance curves obtained in indentation experiments showing the effect of adhesion force. Maximum indentation depth ( $h_m$  for nonadhesive contact and  $h'_m$  for adhesive contact), depth of remnant imprint ( $h_f$ ) and displacement at minimum value of the loading force, ( $h_0$ ) are shown.

$$P(h) = -\frac{4\gamma_a \cdot r_a}{\cos \alpha} + \left( 2E^* r_a - \frac{8\gamma_a \tan \alpha}{\pi \cos \alpha} \right) \cdot h + \frac{2E^* \tan \alpha}{\pi} \cdot h^2. \quad (55)$$

This dependence provides a more accurate description of indentation force in nanoindentation experiments affected by adhesion. Mathematically,  $P$  is a second order polynomial function of  $h$  with the first term expressing the constant adhesive force at the initial contact of the indenter with the sample, the linear term comprising elastic and adhesive effects, and a quadratic term describing the typical variation of the elastic force in conical indentations. Fitting of experimental data with this expression of  $P(h)$  yields values of three parameters,  $r_a$ ,  $\gamma_a$ , and  $E^*$ . Figure 66 provides a comparison of theoretical expressions of  $P(h)$  for the case no adhesion ( $F_a = 0$ ), adhesion model in which  $r_c$  is approximated by the Eq. (40), and adhesion model in which  $r_c$  is approximated by the Eq. (41). In the previous adhesion model [Eq (52)] the parameter  $h_f$ , of which values was

considered negative, was introduced to express the effect of adhesion on the indenter-sample contact, the negative values of  $h_f$  indicating that the sample surface is pulled up when the indenter-sample contact breaks up. The parameter  $h_f$  in Eq. (52) is the analogue of the parameter  $r_a$  in Eq. (55). Figure 63 provides a comparison between the two models of indentation.

Figure 67 shows the typical force-displacement curve obtained in the AFM indentation experiments on the PDMS sample. The displacement of the AFM tip was determined by subtracting the deflection of the AFM cantilever from the total displacement of the cantilever base. One common problem of the AFM indentation experiments is that the tip is inclined with a small angle  $\beta$  with respect to the direction perpendicular to the sample surface. This generates an in-plane displacement of the tip with a distance,  $\Delta y$ , that depends on cantilever length,  $L$ , applied force,  $P$ , cantilever spring constant  $k$ , and  $\beta$  [158].

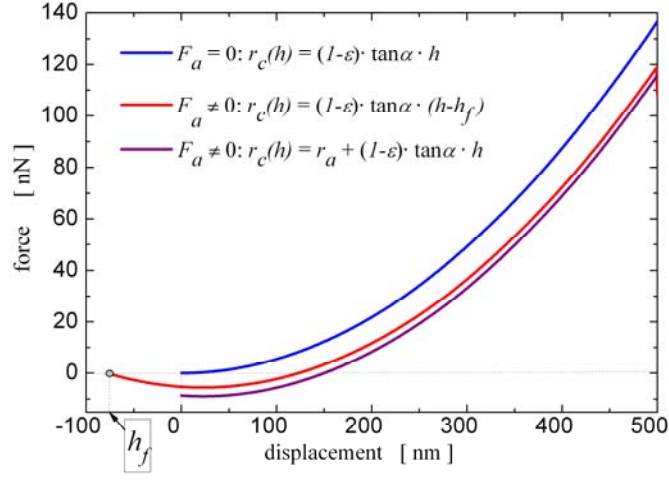


**Fig. 66 Dependence of the indentation force on indenter displacement predicted by indentation model that ignores the contact adhesion  $F_a = 0 : r_c(h) = (1-\varepsilon) \cdot \tan \alpha \cdot h$ , takes into account the adhesion force but ignore the effect of adhesion on the contact area [ $F_a \neq 0 : r_c(h) = (1-\varepsilon) \cdot \tan \alpha \cdot (h-h_f)$ ], and takes into account the adhesion force and the effect of adhesion on contact area [ $F_a \neq 0 : r_c(h) = r_a + h \cdot (1-\varepsilon) \cdot \tan \alpha$ ], respectively.**

In this indentation experiments ( $L = 100 \mu\text{m}$ ,  $k = 11.5 \text{ N/m}$ ,  $P < 50 \text{ nN}$ , and  $\beta = 20^\circ$ )  $\Delta y$  was estimated to be smaller than 2 nm, which is, by comparison to the corresponding vertical displacement of the tip, a negligible distance. The tilt of the tip is affecting also the tip sample contact area because the contact depth along the tip axis is larger than contact depth measured in vertical direction,  $h_c$ , by a factor of  $1/\cos \beta$  (1.064 for our AFM apparatus). In spite of the above-described drawbacks, the AFM indentation experiments on PDMS samples showed a remarkable agreement with the theory. The effect of adhesive force on the force-displacement curve is easily noticed, as the unloading part of the curve presents an important part with negative values of the

loading force. The unloading part of the force-displacement curve shows a very good fit ( $R^2 = 0.99$ ) with the theoretical force-displacement described by Eq. (52). The value of 2.08 for  $n$  confirms the conical geometry of the AFM tip-sample contact. Fittings for a set of force-displacement curves taken for indentation experiments on a matrix of  $7 \times 7$  points homogeneously distributed on an area of  $1 \times 1 \mu^2$  of the PDMS sample surface with the dependence described by Eq (52) have determined values of  $1.91 \pm 0.33$  MPa (mean and standard deviation values) and  $0.095 \pm 0.023$  N/m for  $E$  and  $\gamma$ , respectively. These values are close to the values measured in tensile and detachment macroscopic experiments. This agreement can be considered as a passed test for the analysis of indentation data proposed in reference [99].

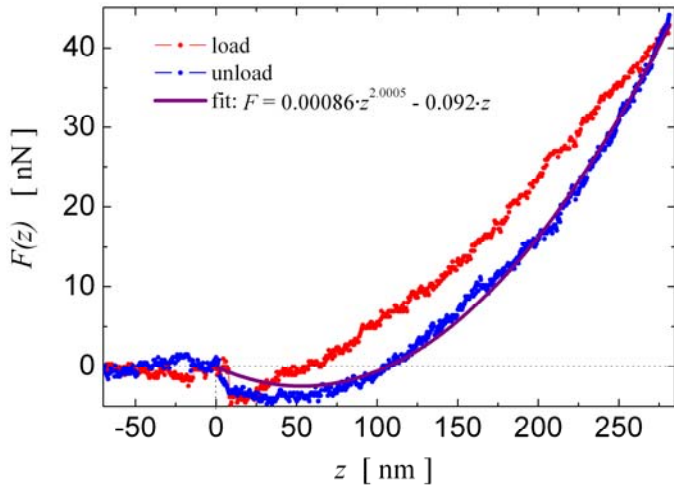


**Fig. 67** Typical force-distance curve obtained in indentation of PDMS sample with sharpened AFM tip showing a good fit ( $R^2 = 0.99$ ) with the theoretical force-displacement dependence.

Sirghi et al [98] used the theoretical model of indentation described above to analyze the force-displacement curves acquired in living cell indentations with pyramidal AFM tips. It was considered that the indentation force equilibrates the elastic force of the cell cytoskeleton and the adhesion force of the cell membrane. The indenter-cell contact area and the adhesion force were assumed to decrease continuously during the unloading part of the indentation (peeling model). Force-displacement curves measured in indentation experiments performed with silicon nitride AFM probes with pyramidal tips on live cells (mouse fibroblast Balb/c3T3 clone A31-1-1) in physiological medium at  $37^\circ\text{C}$  were analyzed to determine the cell elasticity modulus and indenter-cell work of adhesion. Figure 68 a) shows a sketch of the experimental setup. The cells were cultured on sterilized glass slides in complete culture medium at  $37^\circ\text{C}$  in a cell incubator. The live cells grown in sub confluent layer on the glass slide were washed twice with PBS and then

transferred to the AFM liquid cell filled with incomplete cell culture medium (without phenol red). The silicon nitride AFM probes used in the measurements (Microlever MLCT-AUNM from Veeco) had soft triangular cantilevers (nominal constant of 10 mN/m) and pyramidal unsharpened tips (with pyramid angle of 35° and maximum curvature radius of 60 nm). The precise values of the spring constant of the AFM probes used in the indentation experiments were determined by measurements of the thermal noise spectra of the AFM deflection signal of the free AFM probes in air. Prior to the indentation experiments, AFM probes were cleaned by imbedding them successively in ethanol and chloroform (30 minutes for each process) in order to remove contaminant molecules adsorbed on the probe surface. Alternatively, some AFM measurements were performed with PEO coated AFM probes. Details on PECVD of PEO coatings are described in section II.2.2. Figure 68 b) presents a topography image of a living cell showing a cell thickness of about 2 $\mu$ m near the cell nucleus. Therefore, the indentation experiments were performed only in the proximity of cell nucleus where the cells are thick and the effect of hard substrate is negligible. Moreover, in this region the cytoskeleton structure is more homogeneous and does not show microtubules [as it is shown in the topography image in Fig. 68 b)].

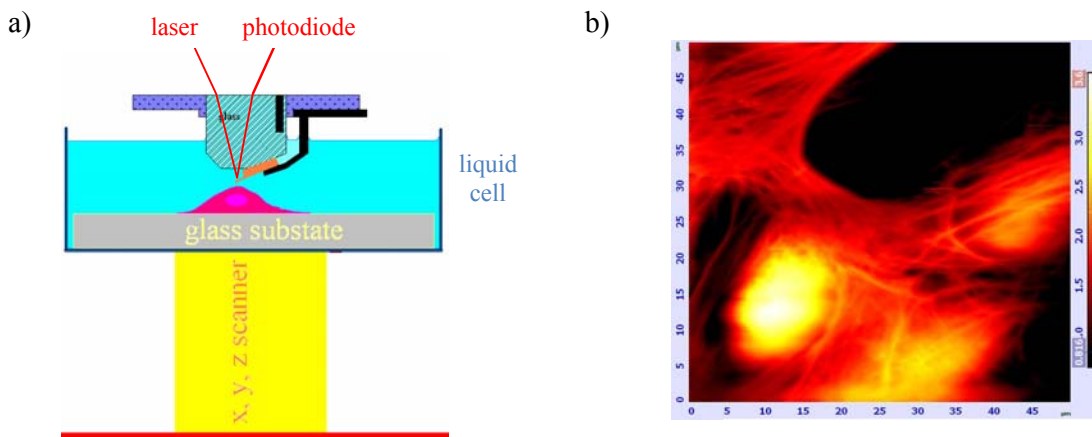


**Fig. 68** a) sketch of the AFM liquid cell containing the AFM probe and the sample consisting of living cells on a glass substrate (the dimension of the AFM probe and cell are exaggerated for clarity). b) Topography AFM image of a living cell showing the nucleus and the structure of cytoskeleton. The indentations were performed on thick part of the cell, near the nucleus.

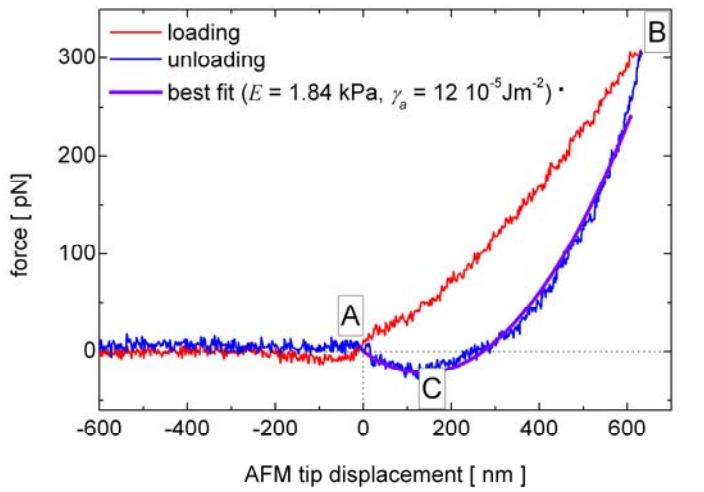


**Fig. 69 Typical force-displacement curve and the best theoretical fit obtained in live cell indentation experiments showing a continuous variation of the adhesion force.**

A typical force distance curve obtained in indentation of cell near its nucleus with a maximum indentation depth of 650 nm is presented in Fig. 69. Because of the cell is very soft (typical values of Young modulus of 2 kPa), the force required to perform this indentation is very small (0.3 nN). The force curve data were fitted with the indentation described above where the adhesion force between cell membrane and pyramidal AFM tip was considered to determine the work of adhesion for silicon nitride surface towards the cell membrane. The fitting yielded values of cell elasticity modulus and work of adhesion. In some indentation experiments, especially in those where large values of indentation depth and indentation force were used, it was observed the phenomenon of cell membrane tethering to the AFM tip [98]. Figure 70 a) shows a sketch of the phenomenon with the cell membrane that adhere to the AFM tip and the cell is pulled up until a sudden detachment occurs. A typical force versus indenter displacement obtained in such a experiment is given in Fig. 67 b). It is noticed that the maximum indentation depth in this indentation is 2000 nm and the maximum indentation force is 7 nN. During AFM tip retraction, the cell membrane is tethered to the AFM tip and detached suddenly after cell elongation (point D on force curve). To prevent the membrane tethering phenomenon and to minimize the effect of adhesion force on the indentation curves, the AFM probes were coated by a Poly(ethylene oxide) (PEO) layer. The PEO surface is well known for its ability to reduce adsorption of protein and cell adhesion (see section II.2.2). Figure 71 presents two force versus displacement curves obtained in indentations of living (mouse fibroblast Balb/c3T3 clone A31-1-1) in physiological medium at

37°C with AFM probes with different tip geometry and surfaces. The indentation performed with a pyramidal Si<sub>3</sub>N<sub>4</sub> tip showed a noticeable adhesion force (visible as negative values of indentation force on the unloading force curve in Fig. 71) between the Si<sub>3</sub>N<sub>4</sub> surface of the tip and cell membrane.

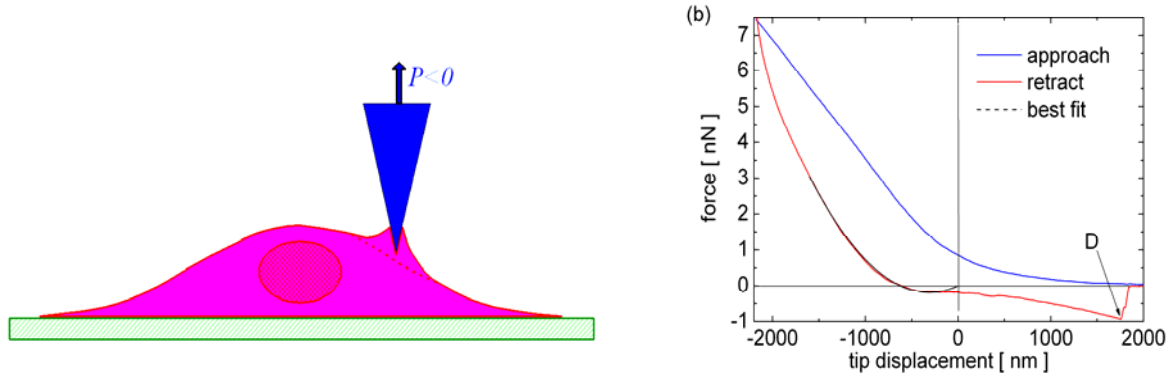


**Fig. 70** a) Tethering of cell membrane to the AFM tip during a hard cell indentation (the maximum indentation force. b) Typical force-displacement curve obtained in live cell indentation experiments showing a discontinuous variation of the adhesive force interpreted as a cell membrane detachment events (indicated by D ).

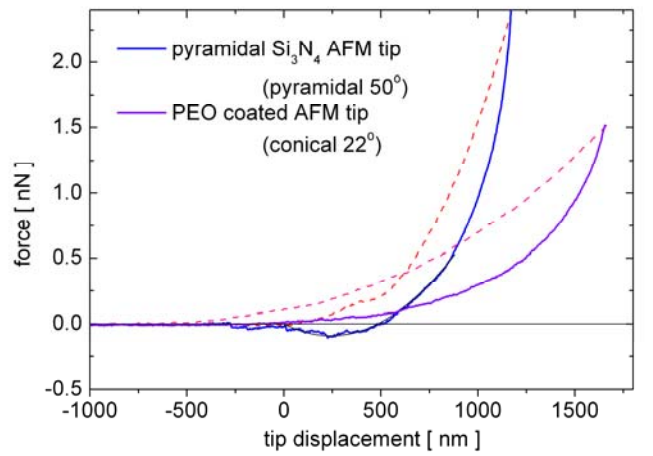


**Fig. 71** Force versus tip displacement obtained in indentation of living cells (mouse fibroblast Balb/c3T3 clone A31-1-1) in physiological medium at 37°C by a Si<sub>3</sub>N<sub>4</sub> pyramidal AFM tip and a PEO coated conical AFM tip. The pyramid and cone angle values ( $50^\circ$  and  $22^\circ$ , respectively) are shown. The PEO coating reduced the adhesion force between the AFM tip and cell membrane to zero.

On the other hand, the force versus indenter displacement obtained in cell indentations performed by PEO covered AFM tip shows no adhesive force between the PEO surface of the tip and cell membrane (Fig. 71). In summary, indentation of small objects with small indenters (tips of AFM probes) are affected by indenter-sample adhesion force. Therefore, analysis of the curves of indentation force versus indenter displacement obtained in these experiments requires use of a indentation model that take into account the effect of adhesion. Such a model has been proposed by Sirghi and Rossi [99] considering a continuous variation of the indenter-sample contact area. The model was further improved to consider the effect of adhesion on the indenter-sample contact radius {Sirghi and Rossi [157]}. According to the proposed models, analysis of the force versus indenter displacement data allows for determination of sample elasticity modulus and work of adhesion for sample and indenter surfaces. Application of the model to AFM indentation experiments of living cells led to information on cell elasticity and membrane adhesion to Si<sub>3</sub>N<sub>4</sub> surface of AFM tips {Sirghi et al [98]}. Some cell indentation experiments showed the phenomenon of membrane tethering to the AFM tip. This is happening due to large adhesion between membrane and AFM tip, especially in hard indentations (large values of indentation force and indentation depth). In order to reduce the adhesion between the AFM tip and cell membrane, the AFM tip has been coated by a thin PEO layer by PECVD. AFM indentations performed with PEO coated AFM tips showed negligible indenter-cell adhesion, the only force governing the indentation being the elastic force. This is an example of use of plasma technology to tailor surface properties of nanoscopic indenters (AFM probes) with the goal of controlling of surface forces.

### **III. Prospective and future research**

This section presents the point of view of the author of the present habilitation thesis on the state of the art and future of low-pressure plasma as a tool for material processing for various applications in microelectronics, energy, life science, medicine, nanotechnology, etc. This includes the use of plasma in surface functionalization, polymerization, surface nanopatterning, and synthesis of new functional materials in form of thin films, nanocomposite materials, nanoparticles, nanotubes, etc. Prospection of new directions of research involving the use of plasma technology for surface functionalization and synthesis of new functional materials is done taking into account the present and future technological needs of our modern society.

As a result of global problems of a growing population with an increased demand of energy, services and goods, the science and technology in the 21st century is relying heavily on the development of new smart devices and functional materials [159, 160]. The development of such materials is an essential task in many fields of science and technology such as energy, medicine, life science, electronics, etc. This trend is following the lesson of nature, which created many highly functional materials as solutions of various biological functions in living organisms. Therefore, material science in the future will be directed toward creation of highly functional materials that may surpass the biological materials. Physical and chemical properties of functional materials are sensitive to a change in the environment such as temperature [161], sound [162], electric field [163], magnetic field [164], light [165], adsorbed gas molecules, and the pH value. As an example, poly(N-isopropyl-acrylamide) (pNIPAM) has a fast and reversible response to medium temperature at a neutral pH value, presenting a hydrophilic surface below a phase transition temperature ( $28^{\circ}\text{C}$ ) and a less hydrophilic (or hydrophobic) surface at higher temperature values. Figure 73 shows this behavior of a pNIPAM layer obtained by grafting NIPAM on plasma activated surface of a polyethylene glycol oxide layer deposited on silicon by plasma enhanced chemical deposition [166]. Another example of highly functional material is inspired by Lotus leaf of which superhydrophobic surface (water contact angle larger than  $150^{\circ}$ ) avoids contact with water and works in the same time as a self-cleaning surface. It has been discovered that this unique property of Lotus leaf is due not only to the hydrophobic property of wax but also to a hierarchical structure at nano- and micro- scales [167]. The researches are following the lessons of nature and adopted strategies that combine materials with low surface energy and rough substrates to reproduce the water repellency behavior. Creating such surfaces that repels water or some other liquids would have a big technological impact in fabrication of micro electro mechanical devices, biomedical devices, fuel transport pipelines, building materials, etc.

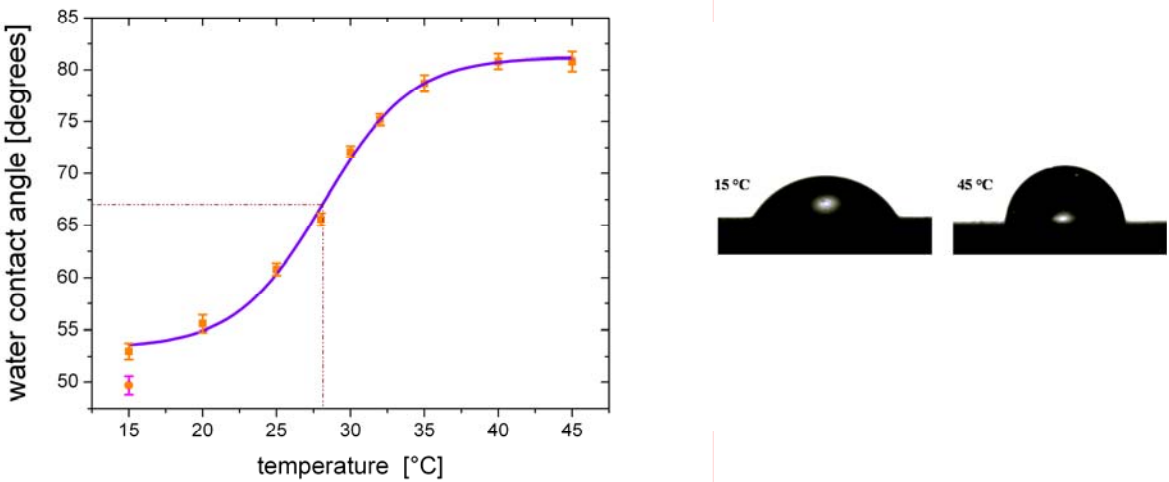


**Fig. 73 Example of thermo sensitive functional material obtained by grafting NIPAM on plasma treated polyethylene glycol oxide layer on a silicon substrate. The surface hydrophilicity changed when the material is heated above 28° C [166].**

Among other synthesis methods, it has been proved that plasma fluorination followed by cross-linking of polybutadiene films gives rise to the formation of hard super-hydrophobic surfaces [168].

In the context of actual need of functional materials, searching of new routes to prepare such materials, controlling their structure and understanding the relationship between the structures and their properties are very important. A key requirement in preparations of materials is to control the structural and chemical composition for achieving superior properties. Because its versatility and good control, low-pressure plasma has been and will be an important tool for synthesis of various functional materials [169]. Plasma processing of materials started to be used in microelectronics industry in 70's. Considerable advancement in plasma sources, plasma processes, and plasma control and diagnostics has been done since then. As result, today's plasma technology is used intensively not only for thin film depositions, ion implanting, doping, cleaning and various surface treatments in the microelectronics industry, but also in processing polymers, biomaterials, photocatalytic materials, and synthesis of composite materials, nanoparticles and nanotubes.

Low pressure plasmas provide key techniques in the fabrication of the ever smaller microelectronic devices [170]. Plasma-assisted etch and thin film deposition at low temperature processes are used to precisely define critical electronic device structures. Plasma technology has allowed the semiconductor industry to follow what is known as Moore's law, *i. e.* the number of devices in an integrated circuit (IC) tended to double every 2 years. Fabrication of ICs requires several hundred processing steps in order to obtain complex, multilayered structures. These processes involve the deposition and patterning of metallic, semi conducting, and insulating thin

films on top of a semiconducting single crystal substrate. The increased number of devices per IC has been accomplished by scaling down the device dimensions, which is technologically challenging not only from the point of view of patterning at nanoscale. Thus, the continuous decrease in the size of ICs requires fabrication of dielectric layers with dielectric constant that is lower than that of commonly used silica layers. A class of materials that has shown promise for this purpose is based on amorphous hydrogenated carbon thin films produced by plasma-assisted deposition [171]. These films, known as amorphous hydrogenated carbon (a-C:H) or diamond-like-carbon (DLC), have a cross-linked network structure of carbon with variable amounts of hydrogen bonded via a mixture of  $sp_3$  (diamond),  $sp_2$  (graphite), and  $sp_1$  type C bonding. The presence of a significant fraction of  $sp_3$  bonding in the DLC film structures results in good mechanical properties (high hardness), excellent chemical stability, and low dielectric constant. Low-pressure plasma processing of materials has replaced many traditional wet chemistry methods in electronics industry because it allows anisotropic etching and definition of smaller patterns (below 100 nm). It is a dry processing method in ultra-clean atmosphere that avoids the hazards and pollution associated with wet chemistry.

As it has been illustrated in the section II of the present habilitation thesis, one of most important applications of low-pressure plasma is plasma assisted depositions of thin films with various surface functionalities. One important example is plasma assisted synthesis of thin films and nanoparticles with high photocatalytic activity, as  $TiO_2$ ,  $ZnO$ , etc. Synthesis of these materials is important for applications in heterogeneous photocatalytic oxidation of toxic and persistent organic pollutants in water and air under solar UV and visible light radiation [172]. Moreover, photocatalytic splitting of water on metal oxide photocatalytic materials can be a clean, low-cost and environmentally friendly technology for hydrogen production [173]. Hydrogen produced directly from photocatalytic hydrolysis of water is considered as an ideal fuel for the future. In this applications, the sunlight is considered as renewable energy source [174]. The heterogeneous photocatalytic oxidation process relies mainly on generation of hydroxyl radicals at the level of photocatalyst surface capable of converting a wide spectrum of toxic organic compounds into relatively inoffensive end products such as  $CO_2$  and  $H_2O$ . Figure 74 presents a sketch of the heterogeneous photocatalytic degradation of organic and water molecules. The organic molecules are oxidized directly by the holes photogenerated in the valence band, or indirectly by OH radical molecules produced by oxidation of water.

$TiO_2$  is by far the most widely studied photocatalytic material due to its high activity, desirable physical and chemical stability, low cost, and availability. Anatase has been reported to have the highest photocatalytic activity of the common  $TiO_2$  crystalline forms. The  $ZnO$  photocatalyst

showed similar photocatalytic activity in UV range, the band-gap energy of ZnO being equal to that of TiO<sub>2</sub>, i.e., 3.2 eV. Some other metal oxides including CeO<sub>2</sub>, SnO<sub>2</sub>, WO<sub>3</sub> and CdS have also been considered as photocatalytic materials for water molecule splitting and organic contaminants degradation. Figure 75 shows the dynamic of number of published paper reporting synthesis and characterization of TiO<sub>2</sub> and ZnO as photocatalyst materials during last two decades as resulted from a search on Web of Science database. In the recent years, around 600 papers/year and 100 papers/year dealing with TiO<sub>2</sub> and ZnO photocatalysts, respectively, have been published. Many of these works used plasma technology for synthesis of the photocatalytic materials (for example, 10% of the published papers dealing with TiO<sub>2</sub> photocatalytic materials).

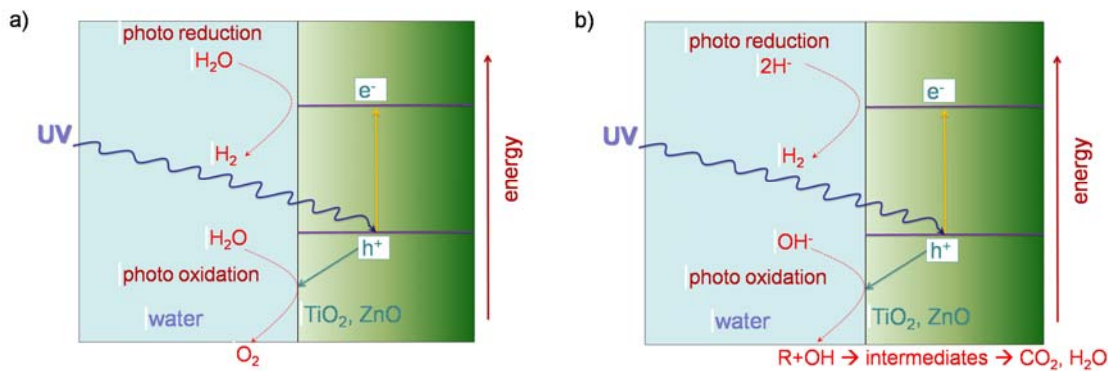


**Fig. 74 Sketch of heterogeneous photocatalysis process of a) water and b) toxic organic molecules on TiO<sub>2</sub> or ZnO photocatalytic materials [173].**

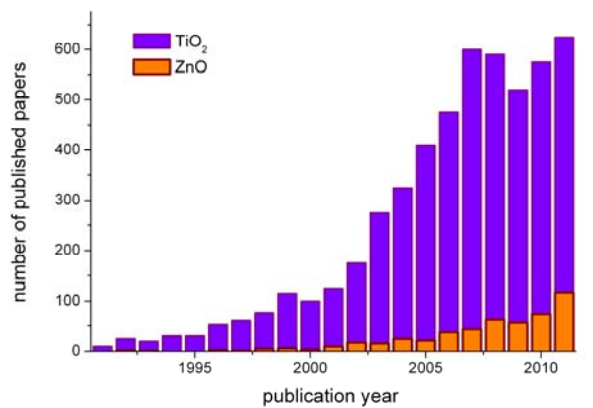


**Fig. 75 Dynamics of number of published papers dealing with TiO<sub>2</sub> and ZnO as photocatalyst materials (source: Web of Knowledge<sup>SM</sup>)**

However application of photocatalytic degradation of toxic organic molecules and water splitting is hampered by some major drawbacks and concerns as low quantum efficiency due to the inefficient visible-light harvesting catalysts, the design of photoreactors, the recovery and reuse of photocatalytic material, the generation of toxic intermediates, and catalyst deactivation. As the photocatalytic activity is usually constrained to the UV wavelength spectrum for photonic activation of catalysts and most of incident solar radiation energy is in the visible spectrum, various methods have been used to broaden the photoresponse spectrum of catalyst material to include the visible range. The solutions used to achieve this goal include doping with metals and non-metal atoms, synthesis of composite photocatalysts, metal ion implantations, etc. [175]. Recently, it has been demonstrated that the use of non-metal dopants (e.g. N, C, F, S and etc.) can improve the photoactivity [176]. Other methods used to improve the photocatalytic activity are directed to obtaining of an increased surface/volume ratio of photocatalytic materials, i. e. synthesis of photocatalytic nanoparticles (NPs) and nanocomposite materials, deposition of photocatalytic thin films on rough substrates, carbon nanotubes, etc. In the last decade the research on composite materials based on metal nanoparticles (NPs) in/on oxide matrices has received great deal of interest due to their potential applications not only in heterogeneous catalysis, but also in gas sensing, non-linear optics, and biological applications [177]. Plasma sputtering [178] and plasma sputtering in combination with CVD [179] have been used to synthesize nanocomposite materials formed by metallic (Ag, Cu, Au) NPs in/on oxide matrices as TiO<sub>2</sub>, SiO<sub>2</sub> and Al<sub>2</sub>O<sub>3</sub>. The novel properties of the nanocomposite materials result from enhancement of the surface-to-volume ratio of small NPs [180] and confinement of charge carriers [181]. Low pressure plasma methods of preparation of metal oxide NPs are much less used than the more popular chemical (sol-gel) methods [182]. However, plasma technology provides clean synthesis environment that not require extensive post-synthesis treatment to remove solvents and other chemical by-products. As it has been shown in the subsection II.1.1, the author of the present thesis contributed to study of deposition mechanisms and characterization of photocatalytic TiO<sub>2</sub> thin films fabricated by plasma enhanced CVD and r.f. magnetron sputtering. Research in this field will be continued and extended to synthesis of new nanocomposite photocatalytic metal oxide thin films with good photocatalytic activity in UV and VIS spectra. Doping of the films with different metals will be explored using the synthesis and doping method described in subsection II.1.3.

During the last three decades the plasma technology has been extending its applications to surface treatments [183]. Unlike plasma-assisted deposition of thin films, where material is added to a surface, plasma surface modification alters the structure and composition of a surface layer of few tens of nm in thickness of a material, leaving the bulk material unaffected. One of the

advantages of this technology is that surface chemical and physical properties can be selectively modified without affecting the bulk characteristics of the treated material. The most preeminent example of plasma surface treatment is that of plastic automobile parts to improve paint adhesion [184]. The plasma surface treatment technique works very well on polymer surfaces. Interaction between plasma and a polymer surface is very complex, including bombardment by energetic particles, irradiation by ultraviolet photons, and chemical reactions. Plasma treatment has results in surface cleaning (removal of adsorbed contaminants and water vapor), ablation, crosslinking, and surface chemical modification [185]. Figure 76 illustrates the growing popularity of plasma surface treatments, the number of papers published every year on this topic reaching the value of 1500. About 200 papers from this value are dealing with polymer surfaces.

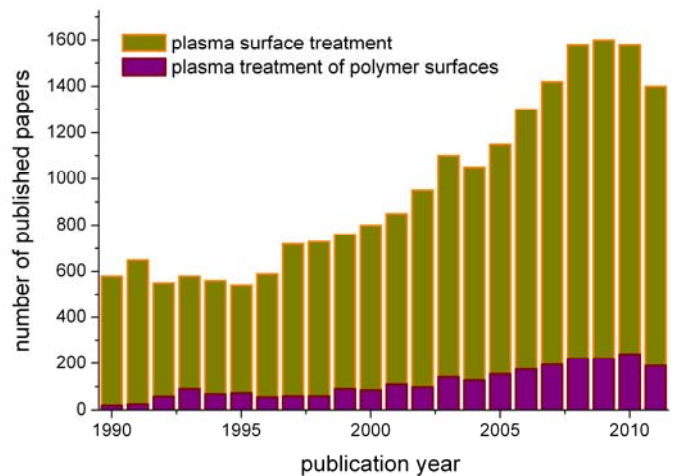


**Fig. 76 Dynamics of number of published papers dealing with plasma surface treatment and plasma surface treatment of polymer surfaces according the Web of Knowledge<sup>SM</sup> database.**

One example of plasma cleaning and hydrophilization of silicon surface has been presented in section II of this thesis [93]. Under the effect of ion bombardment, oxygen and hydroxyl species created in the glow discharge plasma in air at low pressure, the surfaces of silicon samples are cleaned by oxidation and removal of hydrocarbon adsorbed contaminant molecules. Such plasma treatment activates the silicon surface by creating hydroxyl groups and this process can be a fabrication step in chemical functionalisation of silicon probes used in atomic force microscopy. Such a strategy is illustrated in Fig. 77 and is subject of a research project to be developed by the author of the present thesis with the financial support of Romanian Government [186].

Another example of plasma surface treatment is offered by the chemical changes induced by the interaction of Ar/H<sub>2</sub> microwave plasma with the polyethylene glycol oxide (PEO) thin film

surface to create biological adhesive/non-adhesive surface micro- and nano- patterns [140]. Plasma enhanced CVD of PEO thin films is a known method of fabrication of functional surfaces with strong non fouling property for proteins and cells. However, the PEO surface loses its bio repellent property after exposure to Ar/H<sub>2</sub> microwave plasma. Therefore, such plasma treatment can be used to generate nano-patterned surfaces with adhesive contrast for proteins and cells.

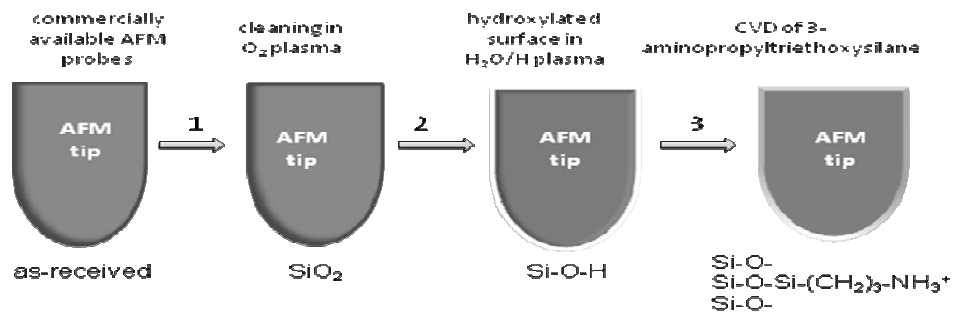


**Fig. 77** Steps of surface functionalization of Si or Si<sub>3</sub>N<sub>4</sub> atomic force microscopy (AFM) probes. 1 - The probe surface is cleaned and oxidized by oxygen plasma; 2 – The probe surface is hydroxylated in H<sub>2</sub>O/H plasma; 3 – the probe surface is subjected to chemical vapor deposition of organosilane molecules with different functional groups. Case of 3-aminopropyltriethoxysilane (APTES) to generate amino functional groups on surface is presented. APTES can be replaced, for example, by Octadecyltrimethoxysilane (C<sub>21</sub>H<sub>46</sub>O<sub>3</sub>Si) for obtaining methyl terminated surfaces.

Such patterned surfaces are studied as sensing platforms for biomolecular recognition because of their high potential for the improvement of bio-detection performance [187]. Recent works have shown that hetero functional nano-structured surfaces containing contrasted chemical response towards proteins (adhesive and repellent) lead to an increase of the immuno-reaction sensitivity recognition between antigens and antibodies couples, when compared to the non structured surfaces[, 189]. These recent results indicate the high potential of these surfaces for enhanced specific bio-reactions on solid substrate and open up new opportunities for the development of a new generation of miniaturized biochips with better performance (e.g. lower detection limit, smaller reagent quantity needed, higher integration...).

In the recent years, an important trend towards the production of patterns with biological functions at the nanoscale has been observed and an impressive number of works has been published. Details on the main patterning methods and results can be found in the recent and complete review on the topic by Blätter *et al.* [190]. Here is presented an example of application of low-pressure plasma in fabrication of nano-patterned surfaces based on organothiols with carboxylic and polyethylene oxide (PEO) terminations. These patterns were obtained on smooth

(RMS roughness of 0.15 nm) gold thin films (200 nm in thickness) transferred by gluing a glass slide. Then, the gold surface was functionalized by SAM deposition of a Mercaptohexadecanoic acid (MHD) layer, followed by spin coating deposition of polystyrene bead ( $\phi = 500\text{nm}$ ) mask and etching by oxygen plasma. Finally, the etched areas were backfilled with thiolated PEO and the beads were lift-off to generate a nanoarray with COOH/PEO chemical contrast. The fabrication steps of the pattern are illustrated in Fig. 77 and an AFM image of the obtained patterned surface is shown in Fig. 78. In this example the colloidal lithography technique [191] is used in combination with plasma etching and SAM deposition techniques. Colloidal lithography can be used in combination with plasma assisted deposition techniques to obtain patterns of the deposited material (metals, oxides, polymers) on various substrates. According to a search on Web of Science about 15% of the 140 papers/year dealing with colloidal lithography are using plasma technology in fabrication of the nanopatterns. These techniques might be used to enhance the photocatalytic properties of surfaces. Some other surface properties as hydrophilicity or hydrophobicity might be also enhanced by these techniques [192]. The author of the present habilitation thesis intends to focus his future research in fabrication and characterization of such nanopatterned surfaces.

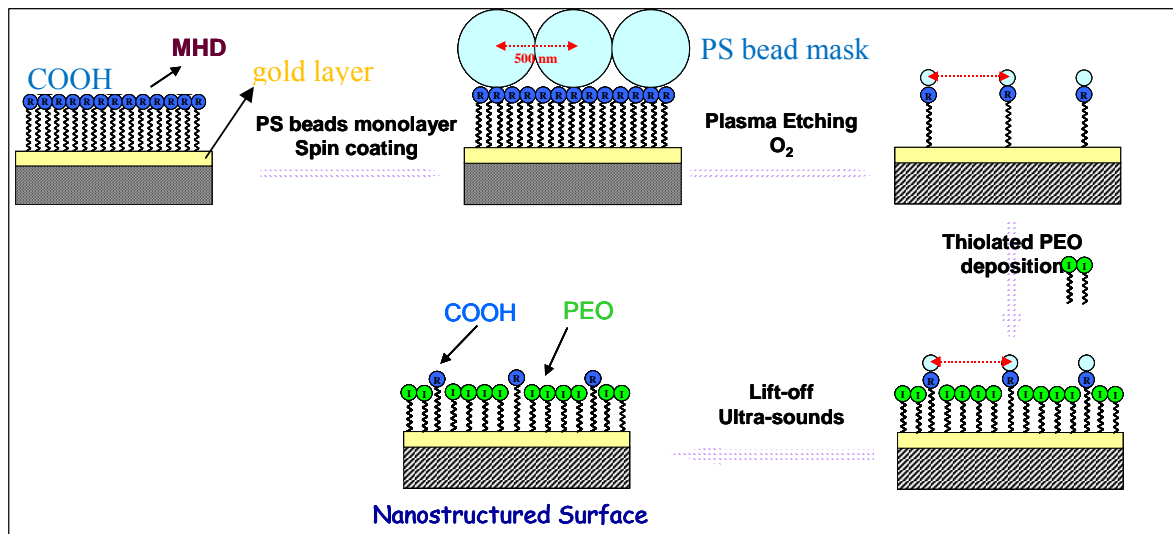


**Fig. 77** Fabrication scheme of -COOH/-PEO chemical patterns on gold substrate. A mercaptohexadecanoic acid (MHD) layer is obtained on gold by self assembled monolayer (SAM) deposition. Then, the layer is covered by a colloidal mask formed by a monolayer of polystyrene (PS) beads, etched in oxygen plasma, and followed by SAM deposition of thiolated PEO and lift-off of the mask.

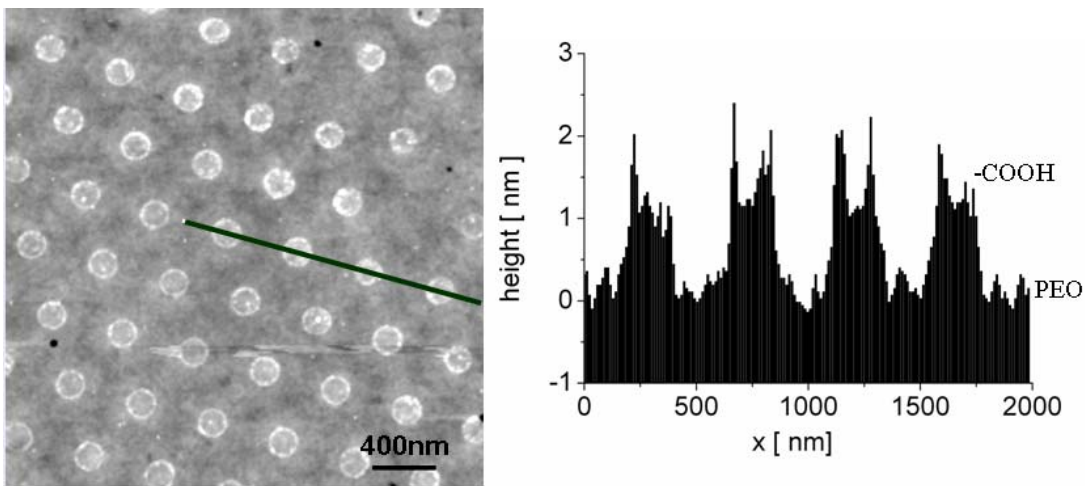


**Fig. 78 - AFM topographic image of the nanoarray (vertical scale 0-3nm) of thiol SAMS on gold showing chemical contrast between -COOH terminated disks surrounded by -PEO terminated matrix. The height profile along a line of four disks is also shown.**

In the last few decades, the low pressure plasma technology have been intensely used for depositions of thin films with various surface functionalities and is likely that the plasma assisted deposition techniques will remain popular in the future. Figure 79 shows the time evolution of number of papers published per year found on Web of Science using the keywords “plasma assisted deposition” and “plasma enhanced CVD” (PECVD), respectively. The plots shows a dramatic increase of the number of papers reporting results of plasma assisting depositions, in the recent years the average number of paper published per year exceeding 3000. A significant number of papers (around 700 papers/year) report results of plasma enhanced chemical vapor depositions. This shows that the plasma technology became very popular for researchers willing to synthesize new materials. Recent development of nanotechnology is likely to enhance this trend because of new nanomaterial (nanoparticles, nanotubes, etc.) synthesis routes offered by plasma [193]. In this respect, Fig. 80 shows the evolution in the last decade of the number of papers published per year found on Web of Science using the keywords “plasma nanotechnology” and “plasma synthesis of nanocomposite materials”, respectively. These plots show that use of plasma in synthesis of nanocomposite, nanoparticle and nanotube materials is increasing in popularity. For example, plasma enhanced CVD (PECVD) is a practical technique of carbon nanotube (CNT) synthesis at relatively low temperature (in comparison to the thermal CVD) known to yield free-standing vertically-aligned CNTs due to presence of large electric field created in plasma sheath [194].

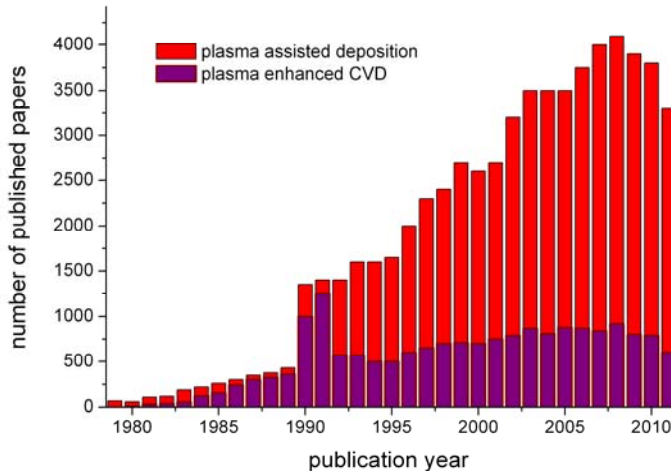


**Fig. 79** Dynamics of number of published papers reporting results of plasma assisted deposition and plasma enhanced CVD according to a search on Web of Science database.

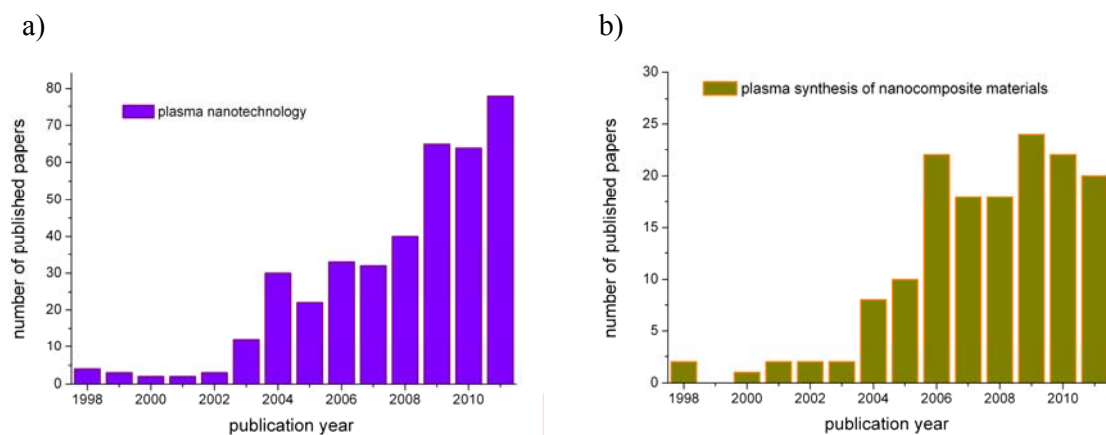


**Fig. 80** Dynamics of number of published papers a) in the field of “plasma nanotechnology” and b) using plasma technology for synthesis of nanocomposite materials.

Usually, this technique uses a r.f. discharge in methane atmosphere to grow CNTs on a nanostructured catalyst (Cobalt) layer deposited on a substrate [195]. In this case, the low-pressure PECVD is known to favor synthesis of carbon nanofibers (CNFs) or multi-walled CNTs (MWCNTs) because of the damages produced by high-energy ion bombardment and excess of reactive species. On the other hand, it is demonstrated that the atmospheric pressure PECVD (AP-PECVD) produces high-purity vertically-aligned SWCNTs [196]

Development of plasma assisted deposition methods for synthesis of new materials in form of thin films, nanoparticles, or nanotubes is related not only on the increased need of new functional materials, but also on the recent evolution of plasma technology involving development of efficient

low-pressure plasma sources as magnetron, radio frequency, microwave and electron cyclotron resonance discharges in low-pressure gases. For example, sputtering deposition became a competitive deposition technique only after discovery of magnetron discharge by Chapin [197] in 1974. This invention allowed deposition rates comparable with physical evaporation depositions due to magnetic field generation of high density plasma near the cathode target at gas pressure values with one order of magnitude lower than in the diode sputtering device using the conventional glow discharge plasma (see Fig. 81). Figure 81 illustrates the versatility of plasma technology in meeting the deposition conditions specific for each application [198]. The unbalanced magnetron uses a magnetic field at the cathode with an open line configuration to allow dense plasma to reach the deposition substrate, thus generating a intense positive ion bombardment of the deposited film in order to control the microstructure of the growing film. The magnetron with supplementary ionization uses additional discharge plasma (hollow cathode or hot cathode) to increase the density of plasma in the deposition chamber. Low-pressure magnetron (not shown) uses a special magnetic field configuration with closed field lines at the target surface in order to decrease the loss of plasma particles, which is especially high at low gas pressure. PECVDs also uses various glow discharge (r.f., microwave or ECR) or arch plasmas to activate reactions in the deposition chamber leading to synthesis of various thin films and nanoparticles [199]. The glow discharge plasmas are non-isothermal and used when bombardment by energetic plasma ions of the growing film surfaces is beneficial for the film properties. To reduce the ion bombardment the PECVD is used in remote glow discharge plasma configuration.

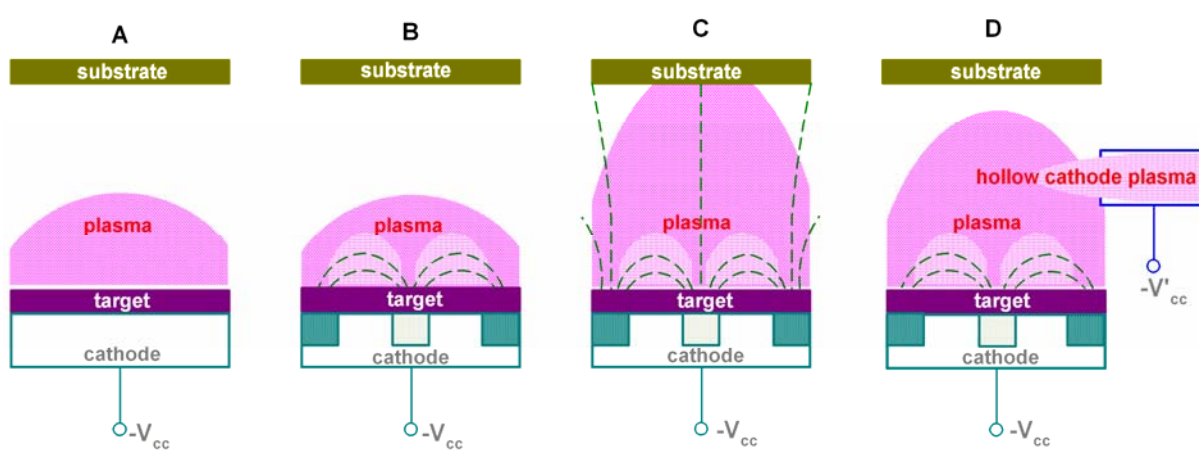


**Fig. 81** Sketches of plasma device configuration used in sputtering depositions. A-sputtering diode; B-conventional magnetron; C-umbalanced magnetron; D-magnetron with additional ionization generated by a hollow cathode discharge [198].

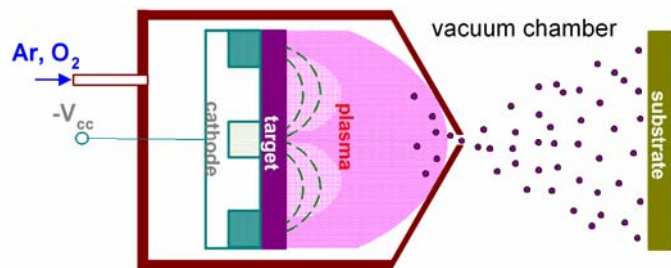


**Fig. 82 Sketch of an experimental setup using a reactive magnetron sputtering deposition in combination with a cluster aggregation source [200] to synthesize nanoparticles. The system has been used in [201] for synthesis of Ti cluster particles in pure Ar plasma.**

The versatility of plasma technology is illustrated also by use of different discharge regimes, as continuous or pulsed mode in direct current (d.c.) or radio frequency (r.f.) electrical discharges in inert or reactive (mixtures of inert and reactive gases as O<sub>2</sub>, H<sub>2</sub>, N<sub>2</sub>, etc. ) low-pressure gas. As an example of versatility of plasma technology, the author of the present thesis used a high power impulse magnetron discharge in reactive gas mixture (Ar/O<sub>2</sub>) and an additional discharge on an aluminum electrode to deposit transparent and electrically conductive ZnO:Al thin films (see the subsection II.1.3). Although in present there is a well established set of so called classical plasma sources used for a broad range of applications, it is foreseen that the evolution of new plasma sources specialized for certain type of applications will not end. For example, recently a conventional planar magnetron discharge was used as a source of Ti atoms in a gas aggregation cluster source [200] to synthesize Ti nanocluster thin films [201]. A sketch of this experimental setup is given in Fig. 82. The author of present habilitation thesis intends to use reactive magnetron sputtering of pure metal (Ta, Zn, Ti) targets in Ar/O<sub>2</sub>/N<sub>2</sub> atmosphere to generate gaseous source material for a gas aggregation cluster source to synthesize oxynitrides nanoclustered thin films. Recently, it has been reported that oxynitrides as TaON, Ta<sub>3</sub>N<sub>5</sub>, and LaTiO<sub>2</sub>N have a high photocatalytic activity for water splitting under visible light [202].

In summary, plasma technology is intensely used in processing highly functional materials. Thin films with various functional properties are currently obtained by plasma assisted chemical vapor depositions or by plasma sputtering. Various plasma sources have been developed for these applications. While d.c. and r.f. magnetron discharges in inert or reactive gases are intensely used for sputtering depositions, the r.f., microwave, electron cyclotron resonance and arch discharges are used in chemical vapor depositions. This trend is expected to continue due to the increased need for new functional materials and development of new plasma sources and techniques. The recent

development of nanotechnology with its need for control of surface structure and chemistry at nanoscale is likely to contribute to further development of plasma technology for new applications related to synthesis and patterning of highly functional materials. The author of the present habilitation thesis intends to focus his research efforts on finding new plasma strategies for synthesis and fabrication of new functional materials and surfaces (including nanopatterning, nanolayers, nanoparticles, nanotubes and nanofibers). Such materials will be developed for various applications in energy (photocatalytic materials in visible light, transparent conductors), water and air purification (photocatalytic decomposition of toxic molecules), biomedicine (platforms for biologic sensors, drug carriers and medical imaging). The effort will be directed to fabrication of surfaces with special properties (highly hydrophilic or hydrophobic, low friction, high hardness) and development of characterization techniques. Atomic force microscopy techniques will be developed further for surface characterization of the new synthesized materials. The AFM is an invaluable technique of surface characterization for nanopatterned surfaces and surface forces. Low pressure plasma is commonly used for cleaning of the AFM probes and there is hope that plasma technology can be used to control the chemistry of the AFM probes, case in which a good characterization of chemical contrast of the patterned surfaces is possible.

## **IV. Selected papers**

### **P1**

L. Sirghi, M. Nakamura, Y. Hatanaka, O. Takai, *Langmuir* **17** (2001) 8199-8203.

*Atomic Force Microscopy Study of the Hydrophilicity of TiO<sub>2</sub> Thin Films Obtained by Radio Frequency Magnetron Sputtering and Plasma Enhanced Chemical Vapor Depositions*

#### **Abstract**

We performed an investigation by atomic force microscopy (AFM) of the hydrophilicity of TiO<sub>2</sub> thin films obtained by radio frequency magnetron sputtering deposition (RFMSD) and plasma enhanced chemical vapor deposition (PECVD). On the basis of a theoretical model of the capillary and superficial tension force of the capillary water bridge formed at tip-sample contact, it is proved that AFM measurements in the atmospheric air of the tip-sample adhesion force provide information about the sample surface hydrophilicity at the microscopic level with a resolution of a few nanometers. Macroscopically, the film hydrophilicity was characterized by a water drop contact angle that, as a result of UV irradiation in atmospheric air, decreased from 60° to 20° for RFMSD films and from 60° to 4° for PECVD films. The AFM measurements revealed that the UV-induced macroscopic changes in the film hydrophilicity corresponded to an increase of the tip-sample adhesive force on the film surfaces. Very inhomogeneous adhesive force distributions were observed for RFMSD films, while even distributions were observed for PECVD films. Fluctuations in sample surface curvature due to grain occurrence on the film surface could not account for the wide spread of the adhesive force values noticed for RFMSD films, and such force distributions were ascribed to an uneven arrangement of oxygen bridging sites on the film surface. The relatively homogeneous distributions of the adhesive force values on the PECVD film surface were characterized by Gaussian probabilities of occurrence.

### **P2**

L. Sirghi, T. Aoki, Y. Hatanaka, *Thin Solid Films* **422** (2002) 55-61.

*Hydrophilicity of TiO<sub>2</sub> thin films obtained by radio frequency magnetron sputtering deposition*

#### **Abstract**

This paper reports results of the macroscopic and microscopic studies of the UV-light-induced hydrophilicity of TiO thin films prepared by radio frequency magnetron sputtering of a pure TiO in an Ar-O mixture gas at different pressure values. The gas pressure affects the crystallographic

structure as well as the surface topography and UV-light-induced hydrophilicity of the deposited films. The microscopic study of the film hydrophilicity is based on friction force microscopy measurements, which are used to microscopically distinguish regions of different hydrophilicity on the film surfaces. These measurements make use of the observation that for a hydrophilic tip, the more hydrophilic the sample surface is, the larger the tip-sample friction force is. The films deposited at a relatively high value of gas pressure (10 mtorr) had an amorphous structure, a good UV-light-induced hydrophilicity and a microscopically smooth and homogeneous surface. The films deposited at lower gas pressure values had mixed crystalline and amorphous structures and relatively rough and inhomogeneous surfaces. The effect of the gas pressure on the plasma particle bombardment of the growing films is discussed to account for the dependence of the structure and surface properties of the films on the gas pressure.

### P3

L. Sirghi, Y. Hatanaka, *Surface Science* **530** (2003) L323-L327 (Surface Science Letters)

#### *Hydrophilicity of amorphous TiO<sub>2</sub> ultra-thin films*

##### **Abstract**

The UV-light-induced hydrophilicity of amorphous titanium dioxide thin films obtained by radio frequency magnetron sputtering deposition was studied in relation with film thickness. The effect of UV light irradiation on the film hydrophilicity was fast, strong and did not depend on substrate or thickness for films thicker than a threshold value of about 12 nm, while for thinner films it was weak and dependent on substrate or thickness. The weak effect of UV light irradiation observed for the ultra-thin films (with thickness less than 12 nm) is explained based on results of measurements of surface topography, UV-light absorption and photocurrent decay in vacuum. Comparing to thicker films, the ultra-thin films have a smoother surface, which diminish their real surface area and density of defects, absorb partially the incident UV light radiation, and exhibit a longer decay time of the photocurrent in vacuum, which proves a spatial charge separation. All these effects may contribute to a low UV light irradiation effect on the ultra-thin film hydrophilicity.

### P4

L. Sirghi, G. Popa, Y. Hatanaka, *Thin Solid Films* **515** (2006) 1334-1339.

#### *Heating of polymer substrate by discharge plasma in radiofrequency magnetron sputtering deposition*

##### **Abstract**

The substrate used for the thin film deposition in a radiofrequency magnetron sputtering deposition system is heated by the deposition plasma. This may change drastically the surface properties of the polymer substrates. Deposition of titanium dioxide thin films on polymethyl methacrylate and polycarbonate substrates resulted in buckling of the substrate surfaces. This effect was evaluated by analysis of atomic force microscopy topography images of the deposited films. The amount of energy received by the substrate surface during the film deposition was determined by a thermal probe. Then, the results of the thermal probe measurements were used to compute the surface temperature of the polymer substrate. The computation revealed that the substrate surface temperature depends on the substrate thickness, discharge power and substrate holder temperature. For the case of the TiO<sub>2</sub> film depositions in the radiofrequency magnetron plasma, the computation indicated substrate surface temperature values under the polymer melting temperature. Therefore, the buckling of polymer substrate surface in the deposition plasma may not be regarded as a temperature driven surface instability, but more as an effect of argon ion bombardment.

## P5

L. Sirghi, A. Ruiz, P. Colpo, F. Rossi, *Thin Solid Films* 517 (2009) 3310-3314.

*Atomic force microscopy indentation of fluorocarbon thin films fabricated by plasma enhanced chemical deposition at low radio frequency power*

### Abstract

Atomic force microscopy (AFM) indentation technique is used for characterization of mechanical properties of fluorocarbon (CF<sub>x</sub>) thin films obtained from C<sub>4</sub>F<sub>8</sub> gas by plasma enhanced chemical vapour deposition at low r.f. power (5–30 W) and d.c. bias potential (10–80 V). This particular deposition method renders films with good hydrophobic property and high plastic compliance. Commercially available AFM probes with stiff cantilevers (10–20 N/m) and silicon sharpened tips (tip radius b10 nm) are used for indentations and imaging of the resulted indentation imprints. Force depth curves and imprint characteristics are used for determination of film hardness, elasticity modulus and plasticity index. The measurements show that the decrease of the discharge power results in deposition of films with decreased hardness and stiffness and increased plasticity index. Nanolithography based on AFM indentation is demonstrated on thin films (thickness of 40 nm) with good plastic compliance.

## P6

L. Sirghi, O. Kylian, D. Gilliland, G. Ceccone, F. Rossi, *J. Phys. Chem. B* 110 (2006) 25975-25981

## *Cleaning and Hydrophilization of Atomic Force Microscopy Silicon Probes*

### **Abstract**

The silicon surface of commercial atomic force microscopy (AFM) probes loses its hydrophilicity by adsorption of airborne and package-released hydrophobic organic contaminants. Cleaning of the probes by acid piranha solution or discharge plasma removes the contaminants and renders very hydrophilic probe surfaces. Time-of-flight secondary-ion mass spectroscopy and X-ray photoelectron spectroscopy investigations showed that the native silicon oxide films on the AFM probe surfaces are completely covered by organic contaminants for the as-received AFM probes, while the cleaning methods effectively remove much of the hydrocarbons and silicon oils to reveal the underlying oxidized silicon of the probes. Cleaning procedures drastically affect the results of adhesive force measurements in water and air. Thus, cleaning of silicon surfaces of the AFM probe and sample cancelled the adhesive force in deionized water. The significant adhesive force values observed before cleaning can be attributed to formation of a bridge of hydrophobic material at the AFM tip-sample contact in water. On the other hand, cleaning of the AFM tip and sample surfaces results in a significant increase of the adhesive force in air. The presence of water soluble contaminants at the tipsample contact lowers the capillary pressure in the water bridge formed by capillary condensation at the AFM tip-sample contact, and this consequently lowers the adhesive force.

### **P7**

L. Sirghi, R. Szoszkiewicz, E. Riedo, *Langmuir* **22** (2006) 1093-1098.

#### *Volume of a Nanoscale Water Bridge*

### **Abstract**

Water bridges formed through capillary condensation at nanoscale contacts first stretch and then break during contact rupture. Atomic force microscopy (AFM) pull-off experiments performed in air with hydrophilic tips and samples show that stretched nanoscopic water bridges are in mechanical equilibrium with the external pull-off force acting at the contact but not in thermodynamic equilibrium with the water vapor in air. The experimental findings are explained by a theoretical model that considers constant water volume and decrease of water meniscus curvature during meniscus stretching. The model predicts that the water bridge breakup distance will be roughly equal to the cubic root of the water bridge volume. A thermodynamic instability was noticed for large water bridges formed at the contact of a blunt AFM tip (curvature radius of 400 nm) with a flat sample. In this case, experiments showed rise and stabilization of the volume of the

water at the contact in about 1 s. For sharp AFM tips (curvature radius below 50 nm), the experiments indicated that formation of stable water bridges occurs in a much shorter time (below 5 ms).

## P8

L. Sirghi, Appl. Phys. Lett. 82 (2003) 3755.

*Effect of capillary-condensed water on the dynamic friction force at nanoasperity contacts*

### Abstract

A single nanoasperity contact in ambient air is usually wetted by capillary condensation of water vapor and is surrounded by a water meniscus. This phenomenon strongly affects the contact friction, not only by the effect of meniscus loading force ~superficial tension and capillary forces!, but also by a friction force that accounts for the energy loss in the meniscus movement along with the sliding contact. Occurrence of the water-meniscus-generated friction is experimentally proved by atomic force microscopy measurements of the tip-sample friction force at minimum possible external load before pull-off. A qualitative explanation for the observed dependence of the friction force on air humidity and solid surface wettability is proposed.

## P9

L. Sirghi, F. Bretagnol, S. Mornet, T. Sasaki, D. Gilliland, P. Colpo, F. Rossi, *Ultramicroscopy* **109** (2009) 222–229

*Atomic force microscopy characterization of the chemical contrast of nanoscale patterns fabricated by electron beam lithography on polyethylene glycol oxide thin films*

### Abstract

The present paper shows that atomic force microscopy (AFM) imaging of friction force and phase lag in ambient air can be used to characterize the chemical contrast induced by electron beam (EB) irradiation on polyethylene glycol oxide (PEO) surface. Time-of-flight secondary emission mass spectroscopy measurements showed that the EB irradiation generates chemical contrast on PEO surface by decreasing the ether bond density. The AFM measurements showed smaller phase lag and lower friction and adhesive forces on the EB irradiated PEO surface, as compared to the non-irradiated PEO surface. While the chemical contrast in friction force had a linear dependence on the EB irradiation dose, the dependence of the chemical contrast in the phase lag was strongly non-linear. As the friction and adhesive forces depended on the AFM probe hydrophilicity and air humidity, the contrast in friction and adhesive forces is ascribed to different capillary condensation

of ambient water vapour at the AFM tip contact with the EB irradiated and non-irradiated PEO surfaces, respectively.

## P10

L. Sirghi, F. Rossi, Applied Physics Letters **89** (2006) 243118

*Adhesion and Elasticity in Nanoscale Indentation*

### Abstract

The present work proposes an extension of Oliver-Pharr analysis (J. Mater. Res. **7**, 1564, 1992) of unloading force-displacement data obtained in nanoscale indentation experiments to account for contact adhesion. The loading force is considered a sum of the contact elastic and adhesion forces. During the unloading, both forces suffer variations. For conical geometry, the unloading force-displacement curve is described by a sum of a quadratic term accounting for the elastic force and a linear term accounting for adhesive force. Results of atomic force microscopy indentation experiments performed with sharpened silicon tips on poly(dimethylsiloxane) agreed well with the prediction of the proposed theoretical model.

## References

- [1] A. Fujishima, K. Honda, *Nature* **238** (1972) 37.
- [2] A. Leinsebliger, G. Lu, J. T. Yates Jr., *Chem. Rev.* **95** (1995) 735.
- [3] A. Fujishima, K. Hashimoto, T. Watanabe, *TiO<sub>2</sub> Photocatalysis, Fundamentals and Applications*, BKC Inc. Tokyo (1999).
- [4] M. Miyauchi, N. Kieda, S. Hishita, T. Mitsuhashi, A. Nakajima, T. Watanabe, K. Hashimoto, *Surface Science* **511** (2002) 401.
- [5] M. Kamei, T. Mitsuhashi, *Surface Science* **463** (2000) L609.
- [6] T. Sumita, T. Yamaki, S. Yamamoto, A. Miyashita, *Appl. Surface Science* **9184** (2002) 1.
- [7] L. Sirghi, Y. Hatanaka, *Surface Science* **463** (2000) L609
- [8] V. Shapovalov, E. V. Stefanovich, T. N. Truong, *Surface Science* **498** (2002) L 103.
- [9] M. Anpo, T. Shima, K. Kubokawa, *Chem. Lett.* (1985) 1799
- [10] P. Schartz, N. J. Turro, S. H. Bossman, A. M. Braun, A. M. Abdel Wahab, H. Durr, *J. Phys. Chem. B* **101** (1997) 7127.
- [11] T. E. Karis, G. W. Tyndall, D. Fenzel-Alexander, M. S. Crowder, *J. Vac. Sci. & Technol. A* **15** (1997) 2382.
- [12] H. Ji, A. Côté, D. Koshel, B. Terreault, G. Abel, P. Ducharme, G. Ross, S. Savoie, M. Gagné, *Thin Solid Films* **405** (2002) 104.
- [13] A. Shirakura, M. Nakaya, Y. Koga, H. Kodama, T. Hasebe, T. Suzuki, *Thin Solid Films* **494** (2006) 84.
- [14] T. Hasebe, A. Shimada, T. Suzuki, Y. Matsuoka, T. Saito, S. Yohena, A. Kamijo, N. Shiraga, M. Higuchi, K. Kimura, H. Yoshimura, S. Kurabayashi, *J. Biomed. Mater. Res.* **76A** (2005) 86.
- [15] C. E. Bottani, A. Lamperti, L. Nobili, P. M. Ossi, *Thin Solid Films* **433** (2003) 149.
- [16] P. Ayala, M. E. H. Maia da Costa, R. Prioli, F. L. Freire Jr., *Surf. Coat. Technol.* **182** (2004) 335.
- [17] G. Tang, X. Ma, M. Sun, X. Li, *Carbon* **43** (2005) 345.
- [18] D. Koshel, H. Ji, B. Terreault, A. Cote, G. G. Ross, G. Abel, M. Bolduc, *Surf. Coat. Technol.* **173** (2003) 161.
- [19] A. Janotti, C.G. Van de Walle, *Rep. Prog. Phys.* **72** (2009) 126501.
- [20] Ü. Özgür, Ya.I. Alivov, C. Liu, A. Teke, M.A. Reshchikov, S. Doğan, V. Avrutin, S.-J. Cho, and H. Morkoç, *J. Appl. Phys.* **98** (2005) 041301.
- [21] A. Janotti, C.G. Van de Walle, *Appl. Phys. Lett.* **87** (2005) 122102.
- [22] L.S. Vlasenko, G.D. Watkins, *Phys. Rev. B* **71** (2005) 12521.

- [23] L. Schmidt-Mende and J.L. MacManus-Driscoll, *Material Today* **10** (2007) 40.
- [24] S. B. Zhang, S.H. Wei, A. Zunger, *Phys. Rev. B* **63** (2001) 075205.
- [25] K. Elmer, *J. Phys. D: Appl. Phys.* **33** (2000) R17.
- [26] P. Kindshott, H. J. Griesser, *Curr. Opin. Sol. State Mater. Sci.* **4** (1999) 403.
- [27] F. Bretagnol, A. Valsesia, G. Ceccone, P. Colpo, D. Gilliland, L. Ceriotti, M. Hasiwa, F. Rossi, *Plasma Process. Polym.* **3** (2006) 443–455
- [28] F. Bretagnol, O. Kylian, M. Hasiwa, L. Ceriotti, H. Rauscher, G. Ceccone, D. Gilliland, P. Colpo, F. Rossi, *Sensors and Actuators B* **123** (2007) 283-292.
- [29] F. Brétagnol, L. Sirghi, S. Mornet, T. Sasaki, D. Gilliland, P. Colpo, F. Rossi, *Nanotechnology* **19** (2008) 125306.
- [30] A. Ruiz, L. Buzanska, D. Gilliland, H. Rauscher, L. Sirghi, T. Sobanski, M. Zychowicz, L. Ceriotti, F. Bretagnol, S. Coecke, P. Colpo, F. Rossi, *Biomaterials* **29** (2008) 4766-4774.
- [31] L. Ceriotti, L. Buzanska, H. Rauscher, I. Mannelli, L. Sirghi, D. Gilliland, M. Hasiwa, F. Bretagnol, M. Zychowicz, A. Ruiz, S. Bremer, S. Coecke, P. Colpo, F. Rossi, *Soft Matter* **5** (2009) 1406-1416.
- [32] L. Sirghi, F. Bretagnol, S. Mornet, T. Sasaki, D. Gilliland, P. Colpo, F. Rossi, *Ultramicroscopy* **109** (2009) 222–229.
- [33] X. Wang, Y. Yu, X. Hu, L. Gao, *Thin Solid Films* **371** (2000) 148.
- [34] M. Nakamura, T. Aoki, Y. Hatanaka , D. Korzec and J. Engemann, *J. Mater. Res.* **16** (2001) 621
- [35] L. Sirghi, M. Nakamura, Y. Hatanaka and O. Takai, *Langmuir* **17** (2001) 8199.
- [36] L. Sirghi, T. Aoki and Y. Hatanaka, *Thin Solid Films* **422**, 55 (2002).
- [37] L. Sirghi, T. Aoki, Y. Hatanaka, *Surf. Coat. Technol.* (2004)
- [38] L. Sirghi, T. Aoki and Y. Hatanaka, *Surface Review Letters* **10** (2003).
- [39] L. Sirghi, y. Hatanaka, G. Popa, *Thin Solid Films* **515** (2006) 1334-1339
- [40] L. Sirghi, A. Ruiz, P. Colpo, F. Rossi, *Thin Solid Films* **517** (2009) 3310-3314
- [41] L. Sirghi, V. Tiron and G. Popa, *Ro Patten Application No. A/00735* , 13.12.2011
- [42] V. Tiron, L. Sirghi and G. Popa, *Thin Solid Films* (2012) doi:10.1016/j.tsf.2012.02.079
- [43] M. Nakamura, S. Kato, T. Aoki, L. Sirghi and Y. Hatanaka, *Thin Solid Films* **401** (2001) 138
- [44] M. Nakamura, L. Sirghi, T. Aoki, Y. Hatanaka, *Surf. Science* **507-510** (2002) 778.
- [45] L. Sirghi, T. Aoki, Y. Hatanaka, *Surf. Coat. Technol.* **187** (2004) 358.
- [46] R. Messier, A. P. Giri and R. A. Roy, *J. Vac. Sci. Technol.* **A2** (1984) 500.

- [47] K. Okimura, A. Shibata, *Jpn. J. Appl. Phys.* **36** (1997) 4917.
- [48] K. Tominaga, M. Chong and Y. Shintani, *J. Vac. Sci. Technol. A* **12** (1994) 1435.
- [49] B. L. T. Lamont Jr., R. J. Jepsen, *Phys. Rev. Lett.* **21** (1968) 1224.
- [50] K. Okimura, A. Shibata, N. Maeda, K. Tachibana, Y. Noguchi and K. Tsuchida, *Jpn. J. Appl. Phys.* **34** (1995) 4950.
- [51] A. Fogden, L. R. White, *J. Colloid Interface Sci.* **138** (1990) 414.
- [52] S. Mezhenny, P. Maksymovych, T. L. Thompson, O. Diwald, D. Stahl, S. D. Walck, and J. T. Yates, Jr., *Chem. Phys. Lett.* **369** (2003) 152.
- [53] M. Nakamura, S. Kato, T. Aoki, L. Sirghi and Y. Hatanaka, *J. Appl. Phys.* **90** (2001) 3391.
- [54] M. Takahashi, K. Tsukigi, T. Uchino, T. Yoko, *Thin Solid Films* **388** (2001) 231.
- [55] H. Poelman, D. Poelman, D. Depla, H. Tomaszewski, L. Fiermans, R. De Gryse, *Surface Science* **482-485** (2001) 940.
- [56] R. Piejak, V. Godyak, B. Alexandrovich, N. Tishchenko, *Plasma Sources Sci. Technol.* **7** (1998) 590.
- [57] E. Stamate, H. Sugai, K. Ohe, *Appl. Phys. Lett.* **80** (2002) 3066.
- [58] M. C. Coen, R. Lehmann, P. Groening, L. Schlapbach, *Appl. Surf. Sci.* **207** (2003) 276.
- [59] M. C. Coen, S. Nowak, O. M. Kuttel, P. Groening, *Appl. Surf. Sci.* **103** (1996) 27.
- [60] L. Sirghi, Y. Hatanaka, G. Popa, *J. Appl. Phys.* **91** (2002) 4026-4032.
- [61] L. Sirghi, Y. Hatanaka, T. Aoki, *Appl. Surf. Scie.* **244** (2004) 408.
- [62] C. E. Bottani, A. Lamperti, L. Nobili, P. M. Ossi, *Thin Solid Films* **433** (2003) 149.
- [63] P. Ayala, M. E. H. Maia da Costa, R. Prioli, F. L. Freire Jr., *Surf. Coat. Technol.* **182** (2004) 335.
- [64] G. Tang, X. Ma, M. Sun, X. Li, *Carbon* **43** (2005) 345.
- [65] A. Milella, F. Palumbo, P. Favia, G. Cicala, R. d'Agostino, *Plasma Process. Polym.* **1** (2004) 164.
- [66] L.-M. Lacroix, M. Lejeune, L. Ceriotti, M. Kormunda, Tarik Meziani, P. Colpo, F. Rossi, *Surf. Sci.* **592** (2005) 182.
- [67] C. A. Clifford, M. P. Seah, *Nanotechnology* **17** (2006) 5283.
- [68] L. Sirghi, F. Rossi, *Appl. Phys. Lett.* **89** (2006) 243118
- [69] B. J. Briscoe, L. Fiori, E. Pelillo, *J. Phys. D: Appl. Phys.* **31** (1998) 2395.
- [70] W. C. Oliver, G. M. Pharr, *J. Mater. Res.* **7** (1992) 1564.
- [71] M.F. Doerner, W.D. Nix, *J. Mater. Res.* **1** (1986) 601.

- [72] I. N. Sneddon, *Int. J. Eng. Sci.* **3** (1965) 47.
- [73] S.P. Chang, R.W. Chuang, S.J. Chang, C.Y. Lu, Y.Z. Chiou, S.F. Hsieh, *Thin Solid Films* **517** (2009) 5050.
- [74] W. Gao, Z. Li, *Ceramics International* **30** (2004) 1155.
- [75] Y. Liu, Q. Li, H. Shao, *Vacuum* **83** (2009) 1435.
- [76] Y. Liu, C.R. Gorla, S. Liang, N. Emanetoglu, Y. Lu, H. Shen and M. Wraback, *J. Electronic Materials* **29** (2000) 69.
- [77] K. Elmer, *J. Phys. D: Appl. Phys.* **33** (2000) R17.
- [78] A.P. Ehiasarian, *Pure Appl. Chem.* **82** (2010) 1247.
- [79] M. Ganciu, M. Hecq, S. Konstantinidis, J. P. Dauchot, M. Touzeau, L. de Poucques, and J. Bretagne, *World Patent No. WO 2005/090632*.
- [80] A.P. Ehiasarian, R. New, W.D. Munz, L. Hultman, U. Helmersson, V. Kouznetsov, *Vacuum* **65** (2002) 147.
- [81] S. Konstantinidis, A. Hemberg, J.P. Dauchot, M. Hecq, *J. Vac. Sci. Technol. B* **25** (2007) L19.
- [82] F. Ruske, A. Pflug, V. Sittinger, W. Werner, B. Szyszka, D.J. Christie, *Thin Solid Films* **516** (2008) 4472.
- [83] M. Wolter, H.T. Do, H. Steffen, R. Hippler, *J. Phys. D: Appl. Phys.* **38** (2005) 2390.
- [84] Y. Chen, D.M. Bagnall, H.J. Koh, K.T. Park, K. Hiraga, Z.Q. Zhu, T. Yao, *J. Appl. Phys.* **84** (1998) 3912.
- [85] D.C. Reynolds, D.C. Look, B. Jobai, C.W. Litton, T.C. Collins, W. Harsch, G. Cantwell, *Phys. Rev., B* **57** (1998) 12151.
- [86] K. Vanheusden, W.L. Warren, C.H. Seager, D.R. Tallant, J.A. Voigt, B.E. Gnade, *J. Appl. Phys.* **79** (1996) 7983.
- [87] M. Liu, A.H. Kitai, P. Mascher, *J. Lumin.* **54** (1992) 35.
- [88] R. Dingle, *Phys. Rev. Lett.* **23** (1969) 579.
- [89] N.Y. Garces, L. Wang, L. Bai, N.C. Giles, I.E. Halliburton, G. Cantwell, *Appl. Phys. Lett.* **81** (2002) 622.
- [90] S. Shionoya, W.M. Yen (Eds.), *Phosphor Handbook, Chemical Rubber*, Cleveland, 1999.
- [91] Z.K. Tang, G.K.L. Wong, P. Yu, *Appl. Phys. Lett.* **72** (1998) 3270.
- [92] V. Musat, B. Teixeira, E. Fortunato, R.C.C. Monteiro, *Thin Solid Films* **502** (2006) 219.
- [93] L. Sirghi, O. Kylian, D. Gilliland, G. Ceccone, F. Rossi, *J. Phys. Chem. B* **110** (2006) 25975-25981

- [94] L. Sirghi, *Appl. Phys. Lett.* **82** (2003) 3755.
- [95] A. Ruiz, L. Buzanska, D. Gilliland, H. Rauscher, L. Sirghi, T. Sobanski, M. Zychowicz, L. Ceriotti, F. Bretagnol, S. Coecke, P. Colpo, F. Rossi, *Biomaterials* **29** (2008) 4766.
- [96] L. Sirghi, F. Bretagnol, S. Mornet, T. Sasaki, D. Gilliland, P. Colpo, F. Rossi, *Ultramicroscopy* **109** (2009) 222–229
- [97] L. Sirghi, R. Szoszkiewicz, E. Riedo, *Langmuir* **22** (2006) 1093-1098.
- [98] L. Sirghi, J. Ponti, F. Rossi, *European Biophysics Journal* **37** (2008) pp. 935-945.
- [99] L. Sirghi, F. Rossi, *Applied Physics Letters* **89** (2006) 243118.
- [100] G. Binnig, H. Rohrer, C. Gerber, E. Weibel, *Phys. Rev. Lett.* **49** (1982) 57.
- [101] W.A. Ducker, T.J. Senden, R.M. Pashley, *Nature* **353** (1991) 239.
- [102] C. M. Mate, G. M. McClelland, R. Erlandsson, S. Chiang, *Phys. Rev. Lett.* **59** (1987) 1942.
- [103] P. Hinterdorfer, *Methods Cell Biol.* **68** (2002) 115-139.
- [104] M. Benoit, H. E. Gaub, *Cells Tissues Organs* **172** (2002) 174-189.
- [105] M. Greene, C. Kinser, D. Kramer, L. Pingree, M. Hersam, *Microscopy Research and Technique* **64** (2004) 415–434.
- [106] Barat Bushan, *Handbook of Nanotechnology* Vol. 2, Springer Berlin (2007)
- [107] H. Kim, J.H. Park, I.-H. Cho, S.-K. Kim, S.-H. Paek, H. Lee, *J. Colloid Interface Sci.* **334** (2009) 161.
- [108] T. Ito, M. Namba, P. Bühlmann, Y. Umezawa, *Langmuir* **13** (1997) 4323.
- [109] C. D. Frisbie, L. F. Rozsnyai, A. Nay, M. S. Wrighton, C. M. Lieber *Science* **265** (1994) 2071.
- [110] A. Janshoff, M. Neitzert, Y. Oberdorfer, H. Fuchs *Angew. Chem., Int. Ed.* **39** (2000) 3213.
- [111] Q. K. Ong, I. Sokolov, *J. Colloid and Interface Science* **310** (2007) 385–390
- [112] R. Luginbuhl, A. Szuchmacher, M. D. Garrison, J. -B. Lhoest, R. M. Overney, B. D. Ratner *Ultramicroscopy* **82** (2000) 171.
- [113] Y.-S. Lo, N. D. Huefner, W. S. Chan, P. Dryden, B. Hagenhoff, T. P. Jr. Beebe *Langmuir* **15** (1999) 6522.
- [114] Senden, T. J.; Drummond, C. J. *Colloids Surf. A* 1995, **94**, 29.
- [115] Tomitori, M.; Arai, T. *Appl. Surf. Science* **140** (1999) 432.
- [116] C. A. R. Costa, E. Radovanovic, E. Teixeira-Neto, M. C. Goncalves, F. Galembeck, *Acta Microscopica* **12** (2003) 71.
- [117] H.-Y. Nie, N. S. McIntyre *Langmuir* **17** (2001) 432.

- [118] E. Bonaccurso, G. Gillies *Langmuir* **20** (2004) 11824.
- [119] H. F. Knapp, A. Stemmer *Surf. Interface Anal.* **27** (1999) 324.
- [120] K. Choi, S. Ghosh, J. Lim, C. M. Lee *Appl. Surf. Scie.* **2003**, 206, 355.
- [121] Ch. Foster, F. Schnabel, P. Weih, Th. Stauden, O. Ambacher, J. Pezoldt *Thin Solid Films* **2004**, 455-456, 695.
- [122] M. Enachescu, R. W. Carpick, D. F. Ogletree, M. Salmeron *J. Appl. Phys.* **2004**, 95, 7694.
- [123] L. Sirghi, M. Nakamura, Y. Hatanaka, O. Takai, *Langmuir* **17** (2001) 8199-8203.
- [124] L. Sirghi, T. Aoki, Y. Hatanaka, *Thin Solid Films* **422** (2002) 55-61.
- [125] L. Sirghi, Rom J Phys. **56** (2011) 144.
- [126] A. Fogden, L. R. White, J. Colloid Interface Sci. **138**, 414 (1990).
- [127] F. Bretagnol, M. Lejeune, A. Papadopoulou, M. Hasiwa, H. Rauscher, G. Ceccone, P. Colpo, F. Rossi, *ActaBiomaterialia* **2** (2006) 165-172.
- [128] L. Ceriotti, L. Buzanska, H. Rauscher, I. Mannelli, L. Sirghi, D. Gilliland, M. Hasiwa, F. Bretagnol, M. Zychowicz, A. Ruiz, S. Bremer, S. Coecke, P. Colpo, F. Rossi, *Soft Matter* **5** (2009) 1406-1416.
- [129] J. N. Israelachvili, *Intermolecular and Surface Forces*, 2<sup>nd</sup> Ed.; Academic Press: New York, 1992.
- [130] Y. Kanda, T. Nakamura, K. Higashitani *Colloid Surfaces A: Physicochem. Eng. Aspects* **139** (1998) 55.
- [131] C. M. Mate, Lorenz, M. R.; Novotny, V. J. *J. Chem. Phys.* **90** (1989) 7550.
- [132] R. Lavery, A. Lebrune, J.-F. Allemand, D. Bensimon, V. Croquette *J. Phys.: Condens. Matter* **14** (2002) R383.
- [133] Xiao, X.; Qian, L. *Langmuir* **16** (2000) 8153.
- [134] L. Sirghi, *Langmuir* **28** (2012) 2558.
- [135] L. Sirghi, N. Nakagiri, K. Sugisaki, H. Sugimura, O. Takai *Langmuir* **16** (2000) 7796.
- [136] S Hartland, R. W. Hartley, *Axisymmetric fluid-liquid interfaces*; Elsevier: Amsterdam, 1976.
- [137] F. Brétagnol, L. Sirghi, S. Mornet, T. Sasaki, D. Gilliland, P. Colpo, F. Rossi, *Nanotechnology* **19** (2008) 125306.
- [138] F. Bretagnol, M. Lejeune, A. Papadopoulou, M. Hasiwa, H. Rauscher, G. Ceccone, P. Colpo, F. Rossi *ActaBiomaterialia* **2**(2006) 165-172.
- [139] F. Bretagnol, L. Cerriotti, M. Lejeune; A. Papadopoulou-Bouraoui, M. Hasiwa, C. Giacomo, D. Gilligand, P. Colpo, F. Rossi, *Plasma Processes and Polymer* **3** (2006) 30–38.

- [140] F. Bretagnol, O. Kylian, M. Hasiwa, L. Ceriotti, H. Rauscher, G. Ceccone, D. Gilliland, P. Colpo, F. Rossi, *Sensors and Actuators B* **123** (2007) 283-292.
- [141] J. Tamayo, R. Garcia, *Appl. Phys. Lett.* **73** (1998) 2926-2928.
- [142] L. Sirghi, T. Aoki and Y. Hatanaka, *Surface Review Letters* **10** (2003).
- [143] J. D. Kraus, *Electromagnetics 3<sup>rd</sup> ed.*, McGraw-Hill Book Co.: Singapore (1984) p. 58.
- [144] J. L. Hutter, J. Bechhoefer *J. Appl. Phys.* **73** (1993) 4123.
- [145] Y.-G. Jung, B. R. Lawn, M. Martyniuk, H. Huang, X. Z. Hu, *J. Mater. Res.* **19** (2004) 3076.
- [146] K. Miyahara, N. Nagashima, T. Ohmura, S. Matsuoka, *NanoStructured Materials* **12** (1999) 1049.
- [147] A. Touhami, B. Nysten, Y. F. Dufrene, *Langmuir* **19** (2003) 4539.
- [148] Y. Rabinovich, M. Esayanur, S. Daosukho, K. Byer, H. El-Shall, S. Khan, *J. of Colloid and Interface Scie.* **285** (2005) 125.
- [149] V. V. Pokropivnyy, V. V. Skorokhod, A. V. Pokropivny, *Modelling Simul. Mater. Sci. Eng.* **5** (1997) 579.
- [150] I. P. Zhao, X. Shi, W. J. Li, *Rev. Adv. Mat. Sci.* **5** (2003) 348.
- [151] W. C. Oliver, G. M. Pharr, *J. Mater. Res.* **7** (1992) 1564.
- [152] I. N. Sneddon, *Int. J. Engng. Sci.* **3** (1965) 47.
- [153] G. M. Pharr, W. C. Oliver, F. R. Brotzen, *J. Mater. Res.* **7** (1992) 613.
- [154] N. A. Stillwell, D. Tabor, *Proc. Phys. Soc. London* **78** (1961) 169.
- [155] L. Sirghi, A. Ruiz, P. Colpo, F. Rossi, *Thin Solid Films* **517** (2009) 3310-3314
- [156] M. F. Doerner, W. D. Nix, *J. Mat. Res.* **1** (1986) 601.
- [157] L. Sirghi, F. Rossi, *Nanotechnology* **20** (2009) 365702.
- [158] R. J. Cannara, M. J. Brukman, R. W. Carpick, *Rev. Sci. Instrum.* **76** (2005) 53706.
- [159] Z. L. Wang and Z. C. Kang, *Functional and Smart Materials. Structural Evolution and Structure Analysis*, Plenum Press, NY, USA (1998)
- [160] B. D. Ratner, A. S. Hoffman, F. J. Schoen, J. E. Lemons, *Biomaterials Science; An Introduction to Materials in Medicine*, Vol. 2, Elsevier, San Diego, USA (2004).
- [161] H. E. Canavan, X. Cheng, D. J. Graham, B. D. Ratner, D. G. Castner, *Journal of Biomedical Materials Research, Part A* **75** (2005) 1.
- [162] C. S. Kwok, P. D. Mourad, L. A. Crum, B. D. Ratner, *Journal of Biomedical Materials Research* **57** (2001) 151.
- [163] M. Cole, N. H. Voelcker, H. Thissen, *Proceedings of SPIE*, Vol. **5651** (Ed.: D. V. Nicolau) Bellingham, USA (2005) 19.

- [164] X. Y. Jing, R. M. Li, P. Wang, J. Wang, Y. Yuan, G. Y. Zhu, *Analytical Chemistry* **27** (1999) 1462.
- [165] D. J. Chung, Y. Ito, Y. Imanishi, *Ind. Eng. Chem. Res.* **39** (1994) 2491.
- [166] P. Heinz, F. Brétagnol, I. Mannelli, L. Sirghi, A. Valsesia, G. Ceccone, D. Gilliland, K. Landfester, H. Rauscher and F. Rossi *Langmuir* **24** (2007) 6166.
- [167] C. Neinhuis, w. Barthlott, *Annals of Botany* **79** (1997) 667-677.
- [168] I. Woodward, W. C. E. Schofield, V. Roucoules, J. P. S. Badyal, *Langmuir* **19** (2003) 3432.
- [169] *Advanced Plasma Technology* (Eds. R. D'Agostino, P. Favia, Y. Kawai, H. Ikegami, N. Sato, F. Arefi-Khonsari) Wiley-VCH Verlag GmbH&Co. KGaA, Weinheim (2008).
- [<sup>170</sup>] B.R. Rogersa,\* T.S. Caleb, *Vacuum* **65** (2002) 267–279
- [171] A Grill, *Diam Relat Mater* **10** (2001) 234–239.
- [172] S. Ahmed, M.G. Rasul, R. Brown, M.A. Hashib, *Journal of Environmental Management* **92** (2011) 311-330.
- [173] M. Ni, M. K. H. Leung, D. Y. C. Leung, K. Sumathy, *Renewable and Sustainable Energy Reviews* **11** (2007) 401–425.
- [174] R. Goslich, R. Dillert, D. Bahnemann, *Water Science and Technology* **35** (4), (1997) 137-148.
- [175] M. N. Chong, B. Jin, C. W. K. Chow, C. Saint, *Water research* **44** (2010) 2997-3027
- [176] A. Fujishima, X. Zhang, D. A. Tryk, *Surf. Sci. Rep.* **63** (2008) 515-582.
- [177] Lidia Armelao, Davide Barreca, Gregorio Bottaro, Alberto Gasparotto, Silvia Gross, Cinzia Maragno, Eugenio Tondello, *Coordination Chemistry Reviews* **250** (2006) 1294–1314
- [178] L. Yang, Y. Liu, Q. Wang, H. Shi, G. Li, L. Zhang, *Microelectron. Eng.* **66** (2003) 192.
- [179] D. Dalacu, L. Martinu, *J. Appl. Phys.* **87** (2000) 228
- [180] C.N.R. Rao, G.U. Kulkarni, P.J. Thomas, P.P. Edwards, *Chem. Soc. Rev.* **29** (2000) 27.
- [181] C. Burda, X. Chen, R. Narayanan, M.A. El-Sayed, *Chem. Rev.* **105** (2005) 1025.
- [182] D. P. Macwan, P. N. Dave, S. Chaturvedi, *J. Mater. Sci.* **46** (2011) 3669–3686.
- [183] M.R. Wertheimer, H.R. Thomas, M.J. Perri, J.E. Klemburg-Sapieha, L. Martinu, *Pure and Appl. Chem.* **68** (1996) 1047-1053.
- [184] Y. Taga, *Surf. Coat. Technol.* **112** (1999) 339-346.
- [185] E. M. Liston, L. Martinu, M. R. Wertheimer, *J. Adh. Sci. Tech.* **7** (1993) 1091-1127.
- [186] L. Sirghi, Grant no. 267/2011 CNCSIS, IDEI Research Program of Romanian Research, Development and Integration National Plan II.

- [187] M. Arnold, E. Ada Cavalcanti-Adam, R. Glass, J. Blummel, W. Eck, M. Kantlehner, H. Kessler, J. P. Spatz *ChemPhysChem* **5** (2004) 383.
- [188] H. Agheli, J. Malmstrom, E. M. Larsson, M. Textor, D. S. Sutherland, *Nano Letters* **6** (2006) 1165
- [189] K. B. Lee, E. U. Kim, C. A. Mirkin and S. M. Wolinsky *Nano Letters* **4** (2004) 1869
- [190] T. Blätter, C. Huwiler, M. Ochsner, B. Städler, H. Solak, J. Vörös, H. M. Grandin, *Journal of Nanoscience and Nanotechnology* **6** (2006) 2237.
- [191] A. del Campo, E. Arzt, *Chem. Rev.* **108** (2008) 911–945.
- [192] J. X. Wang, Y. Z. Zhang, T. Y. Zhao, Y. L. Song, L. Jiang, *Sci. China Chem.* **53** (2010) 318–326
- [193] G. R. Alcott, *Plasma deposition of nanocomposite thin films. Process concept and realization*, Technische Universiteit Eindhoven (2004).
- [194] M. Meyyappan, L. Delzeit, A. Cassell, D. Hash, *Plasma Sources Sci Technol* **12** (2003) 205–16.
- [195] T. Nozaki, T. Karatsu, K. Ohnishi, K. Okazaki, *Carbon* **48** (2010) 232 – 238.
- [196] T. Nozaki, K. Okazaki, *Plasma Process Polym.* **5** (2008) 300–21.
- [197] J. S. Chapin, *US Patent Application*, 438 482 (1974)
- [198] J. Musil, J. Vlcek P. Baroch, Mangetron discharges for Thin Films Plasma Processing, *Materials Surface Processing by Direct Energy Techniques* (Y. Pauleau, Editor) 2006 Elsevier.
- [199] I. Pierson, O. Hugh, *Handbook of Chemical Vapor Deposition 2<sup>nd</sup> edition*, Noyes Publications/William Andrew Publishing LLC, (1999) NY, USA
- [200] H. Haberland, M. Mall, M. Mosseler, Y. Qiang, T. Rainers, Y. Turner, *J. Vac. Sci. Technol. A* **12** (1994) 2925.
- [201] M. Drabik, A. Choukourov, A. Artemenko; J. Kousal, O. Polonskyi, P. Solar, O. Kylian, J Matousek, J. Pesicka, I. Matolinova, D. Slavinska, H. Biederman, *Plasma Processes and Polymers* **8** (2011) 640-650.
- [202] K. Maeda, K. Teramura, N. Saito, Y. Inoue, H. Kobayashi, and K. Domen, *Pure Appl. Chem.* **78** (2006) 2267–2276.